Lancaster University
Physics Department

Theory of molecular scale thermoelectricity

Marjan Famili

This thesis is submitted in partial fulfilment of the requirements for the degree of
Doctor of Philosophy
, May 2018

Deceleration

Except where stated otherwise, this thesis is a result of the author's original work and has not been submitted in substantially the same form for the award of a higher degree elsewhere. Other sources of information have been used, they have been acknowledged. This thesis documents work carried out between November 2014 and May 2018 at Lancaster University, UK, under the supervision of Prof. Colin J. Lambert and Dr. Iain M. Grace funded by the **F**aculty of **S**cience and **T**echnology (FST) of Lancaster University, UK.

Marjan Famili

May 2018

Abstract

In this thesis we use a combination of density functional theory and equilibrium Green's function to study thermoelectricity in molecular scale. We have aimed to improve the efficiency of single molecules in converting heat to electricity by carefully designing them. We introduced a novel strategy for designing molecules with low thermal conductance. This strategy states that adding side branches of different length to the backbone of a molecule can eliminate phonon transport through the backbone over a wide range of frequencies. Moreover, we demonstrate that chemical modification of thiophene molecular wire to ethylenedioxy-thiophene molecular wire can improve their thermoelectric efficiency. Furthermore, to demonstrate that the adopted molecular designs will be effective when scaled up to a self-assembled monolayer (SAM) of molecules, we model three independent experiments on gold-SAM-graphene vertical transport devices. The agreement between our calculations and the experiments elucidates the survival of quantum interference effect on a single molecular level in SAM devices. The work presented in this thesis has received considerable attention from many experimental groups in the UK and overseas stimulating novel experimental studies which are ongoing at present.

Acknowledgements

I would like to express my gratitude to Prof. C. J. Lambert for providing many hours of stimulating discussion, without which the successful conclusion of this thesis would not be possible. I would also like to thank Dr. I. Grace for his supervisory support.

Finally, I would like to acknowledge Lancaster Physics department for the provision of a Studentship.

Dedication

I dedicate this thesis to my parents, Mohammad Famili and Faezeh Amouzgar, who over the years have encouraged me to be a careful observer, have curiosity and a questioning mind. Their endless love, support and encouragement made the completion of this journey possible.

Publications

I. Suppression of Phonon Transport in Molecular Christmas Trees *M. Famili, I. Grace, H. Sadeghi, C.J. Lambert, ChemPhysChem,* ***2017*** *, 18, 1234.*

II. Toward High Thermoelectric Performance of Thiophene and Ethylenedioxythiophene (EDOT) Molecular Wires

M. Famili, I.M. Grace, Q. AlGaliby, H. Sadeghi, C.J. Lambert, Advanced Functional, ***2017****, 1703135.*

III. Cross-plane conductance through a graphene-molecular monolayer-gold sandwich

B. Li, M. Famili , E. Pensa, I. Grace, N. J. Long, C.J. Lambert, T. Albrecht, L. F. Cohen, Submitted to Nanoscale.

IV. Quantum interference mediated vertical molecular tunneling transistors

C. Jia, M. Famili, M. Carlotti, Y. Liu, P. Wang, I. M. Grace, Z. Feng, Y. Wang, Z. Zhao, M. Ding, J. Guo, X. Xu, C. Wang, S. Lee, Z. Wang, Y. Huang, R. C. Chiechi, C. J. Lambert and X. Duan, Submitted Science Advances.

V. Self-assembled molecular-electronic films controlled by room temperature quantum interference

M. Famili, C. Jia, X. Liu, P. Wang, I. M. Grace, J. Guo, Y. Liu, Z. Feng, Y. Wang, Z. Zhao, S. Decurtins, R. Häner, Y. Huang, S. Liu, C. J. Lambert and X. Duan , Submitted to Nature Materials.

Contents

Abstract **ii**

1 Introduction **1**

2 Methodology **5**

2.1 Many-body problem 6

2.2 Born-Oppenheimer approximation 7

2.3 Density functional theory 8

2.3.1 The Hohenberg-Kohn theorems 8

2.3.2 Kohn-Sham equation 11

2.3.3 Exchange-correlation functional 11

2.4 Motion of nuclei 13

2.5 SIESTA implementation of DFT 13

2.5.1 Pseudopotential approximation 14

2.5.2 Numerical Atomic Orbitals (NAO) 15

2.6 Dynamical matrix 17

2.7 Quantum theory of transport 19

2.7.1 The Landauer-Büttiker approach 20

2.7.2 Equilibrium Green's Function method 23

2.8 Thermoelectric properties of materials 29

3 A festive strategy for suppressing phonons in single molecules: Molecular Christmas trees 30

3.1 Introduction 31

3.2 Dynamics of model Christmas trees 32

3.3 Dynamics of molecular Christmas trees 43

3.4 Shape vs number of branches 49

3.5 Heavier side branches 52

3.6 Christmas-tree strategy for an acene trunk 52

3.7 Gold lead 56

3.8 Conclusion 56

4 Thermoelectric properties of thiophene and EDOT molecular wires 58

4.1 Introduction 59

4.2 Conductance 60

4.3 Thermal conductance 63

4.4 Figure of merit ZT 65

4.5 Doping EDOT 66

4.6 Conclusion 67

5 Cross-plane Conductance through a Graphene-Molecular Monolayer-Gold Sandwich. 68

5.1 Introduction 69

5.2 The I-V characteristics of the device 71

5.3 Analytical model 74

5.4 DFT Modelling the I-V characteristics of the device 81

5.5 Conclusion 85

6 Quantum interference mediated vertical molecular 87

6.1 Introduction 88

6.2 Modelling gold-SAM-graphene devices 89

6.3 Properties of the molecules 91

6.4 Current and conductance 92

6.5 Conclusion 100

7 Self-assembled molecular-electronic films controlled by room-temperature quantum interference 102

7.1 introduction 103

7.2 Results 105

7.3 Conclusion 115

8 Conclusion 117

Bibliography 119

Appendices **144**

A General Scattering problem **145**

B Green's Function of a perfect one dimensional lattice **153**

C Dyson's equation **158**

C.1 Example-Single impurity 161

C.2 Example - 2×2 impurity 162

D ZT **165**

E Python code for solving the analytical model provided in chapter 3 **169**

List of Figures

2.1 A schematic description of a many body problem. i and j are electronic labels. α and β are the nuclei labels. $\mathbf{r}$ and $\mathbf{R}$ denote the vector coordinates of the electrons and nuclei respectively. 6

2.2 Schematic illustration of the pseudopotential approximation. All-electron potential (light blue) and pseudopotential (dark blue) converge to the the same function outside the cut-off radius (rc). This is the same for the corresponding wavefunctions (purple and pink). 15

2.3 A schematic description of vector coordinates utilised to describe basis sets 16

2.4 Deviation of atoms from their equilibrium position for the purpose of using finite differences method to obtain the vibrational properties of a system. M_i and M_j are the masses of the i^{th} and j^{th} atoms. . . 18

2.5 (a) Scatterer (white) placed between two leads (yellow). The leads are connected to two reservoirs with chemical potential μ_1 (pink) and μ_2 (blue) where μ_2 is elevated by eV. (b) The dispersion relation. 20

2.6 A quantum system coupled to the left (R) and right (R) leads. $\boldsymbol{H}_S$ is the non-interacting Hamiltonian of the scattering region. 24

2.7 System is divided into 3 highlighted blocks. Green representing all the leads ($\boldsymbol{H}_O$), red is the scattering region ($\boldsymbol{H}_S$) and blue includes all the matrix elements connecting the leads to the scattering region ($\boldsymbol{H}^P$). 25

3.1 (a) A SAM connected between hot and cold electrodes. (b) Examples of molecules possessing pendant groups (oriented vertically) connected to molecular trunks (oriented horizontally) formed from alkyl chains. 33

3.2 Idealised examples of vertical molecular backbones, with pendant side branches. The mass of the brown 'atoms' is m and the mass of the green 'atoms' is M. The brown spring constants are γ and the green spring constants are α. 33

3.3 (a) Single side branch. (b) Chain side branch with N sites. γ, α and β are the Hessian matrix elements between the illustrated sites. . . 34

3.4 The side branch in figure 3.3a can be decimated to yield an infinite chain with a single impurity whose onsite energy is ε. 35

3.5 For model Christmas trees formed from single-degree-of-freedom masses, such those shown in figure 3.2, (a), (b) and (c) show the transmission coefficient for N=1, 3 and 10 side branches respectively. In each case, the lengths of the branches increase sequentially from 1 to N. (d) The phonon thermal conductances of structures 3.5a (black), 3.5b (red) and 3.5c (blue) obtained by combining the transmission coefficients $3(a-c)$ with equation 3.27. Results are shown on the scale of Debye temperature $T_D = \hbar\Omega_D/K_B$. 40

3.6 ($a-c$) Transmission coefficients of a Christmas-tree with 10 side branches, when $\alpha = 0.2, 0.4$ and 0.7. (d) The corresponding thermal conductances versus temperature. 42

3.7 Red and black cures curve shows the $T_{ph}(\omega)$ (on the left) and κ_{ph} (on the right) for chain attached to wall and chain with three side branches respectively. 42

3.8 (a) Transmision coefficient comparison for illustrated models. (b) The phonon conductance. This demonstrates that the presence of branches of different lengths is desirable. 43

3.9 DFT results for the transmission coefficients and thermal conductances of molecules 1 (black), 2 (red) and 3 (blue) of figure 3.1b, where the trunks are formed from infinitely-long alkyl chains. 44

3.10 (a) Number of open phonon channels in an infinite alkyl chain versus frequency. (b) Phonon conductance for a perfect infinite alkane chain. 45

3.11 Comparison between the participation ratio (upper panel) and the transmission coefficient (lower panel). 46

3.12 Participation ratio of CH_3 side branch(red), C_2H_5 side branch (green) and C_3H_7 (blue). The sum of participation ratio of all side branches(black). 46

3.13 Black shows the Alkane with C_2H_5 branch, red is alkane with heavy side branch(no internal degrees of freedom) and green is an alkane branch attached to a wall. 47

3.14 Figures (a), (b), (c) show the phonon transport through molecules 1, 4 and 5 of figure 3.1 b respectively. Figure (d)compares the phonon conductance in molecules a, b and c. 48

3.15 Phonon transmission through alkane trunks with (a) C_2H_5, (b) NCH_4 and (c) OCH_3 side branches Figure (d) shows the phonon thermal conductances of alkyl trunks with OCH_3 (blue), C_2H_5 (black) m,kand NCH_4 (red) branches. 49

3.16 (a) Participation ratio of two side branches CH_3 and C_2H_5 when attached to a rigid wall and (b) for C_3H_7. (c) Comparison of the phonon conductances of the illustrated system. 50

3.17 Participation ratio of all side branches in molecule 2 in figure 3.1b (Black) participation ratio of C_2H_5 side branch (Green) and participation ratio of CH_3 (Red). 51

3.18 (a) Participation ratio of three side branches CH_3, C_2H_5 and C_3H_7 when attached to a rigid wall and (b) for C_6H_{13}. (c) Comparison of the phonon conductances of the illustrated system. 51

3.19 Phonon transmission through molecule 3 in figure 3.1b (b) Phonon transmission for molecule 3 where all the carbons in the side braches are replaced by ^{13}C. (c) Comparison between the phonon thermal conductance of both systems. 53

3.20 Examples of acene branch with various side branches. 53

3.21 ($a-c$) Transmission coefficient for phonons through molecules $a-c$ in figure 3.20. (d) Phonon conductance for molecule $a-c$ respectively. 54

3.22 The number of open channels in an infinite acene chain. 54

3.23 The relaxed geometry of two systems with acene trunk and $C60$ side branch where $C60$ is attached to the trunk via different connections. 54

3.24 Comparison between the phonon conductances for the structures A and B. (c) Comparison between the phonon conductances for the structures A and B. 55

3.25 Phonon conductance through molecule 2 and 7 when placed between two gold leads. 56

4.1 Optimised geometry of the thiophene series (left) and EDOT series (right) for n=1 to 4 units contacted between gold electrodes. 60

4.2 The Seebeck coefficient of T1 (black), Experimental value for the Seebeck coefficient of T1 (red) and the relatively chosen Fermi energy. 61

4.3 Room temperature conductance for the (a) thiophene (a) and (b) EDOT molecular wires shown in figure 4.1. (c) Conductance vs length at $E_F - E_F^{DFT} = 0.35eV$. (d) Beta factor vs. Fermi energy. The predicted value for the decay constant of oligothiophene is somewhat lower than the experimental value of $\beta = 2.9nm^{-1}$,[30,114] because DFT underestimates the HOMO-LUMO gap. 62

4.4 (a) Seebeck coefficient against Fermi energy for thiophenes and EDOTs over a range of $-0.2 < E_F - E_F^{DFT} < 0.6$ (b) Seebeck coefficient over a range of Fermi energy in the vicinity of chosen Fermi energy $E_F - E_F^{DFT} = 0.35eV$ 63

4.5 Phonon transport through the thiophene series. 64

4.6 Phonon transmission through the EDOT series. 65

4.7 (a) The electronic thermal conductance at 300 K over a range of $E_F - E_F^{DFT}$ (b) the phonon thermal conductance of both the EDOT and thiophene series. 65

4.8 (a) ZT in a range of Fermi energy from -0.2 to 0.6 (b) over a range of Fermi energy in the vicinity of chosen Fermi energy $E_F - E_F^{DFT} = 0.35eV$ 66

4.9 (a) Toluenesulfonate (TOS) and EDOT:TOS in the junction and the comparison between the logarithm of conductance (b), Seebeck coefficient (c) and the (d) ZT of E3 in a doped and undoped state. 66

5.1 (a) Optical image (graphene is shown as light grey colour) (b) cross-section schematic illustration of the vertical transport device. (c) Au/BPDT/graphene model used for calculations. Representative (d) I-V and (e) dI/dV vs V characteristics of the vertical transport device (offset of the minimum differential conductance indicated by the blue arrow). (f) The experimentally determined zero bias conductance (G_{SAM}) versus junction width. The red dash curve is a guide to show the expected trend of G_{SAM} with junction area assuming 100% coverage. 71

5.2 (a) The predicted room-temperature electrical conductance of a n-doped graphene/BPDT/Au junction (blue) and a p-doped graphene/BPDT/Au (pink), divided by the room temperature single-molecule conductance of the Au/BPDT/Au junction. The predicted ratio depends on the doping of the graphene and on the precise location of the Fermi energy E_F relative to the frontier orbitals of the molecule. However, over a range of such values in the vicinity of the DFT-predicted Fermi energy (shown shaded in green) the ratio varies from 10^{-2} to 10^{-3}. (b) Overview of the parameters involved in the generic model where $\Gamma_{1,2}$ are level broadening due to contact with the source and drain and ε_m is maximum energy of the molecular orbital. 73

5.3 The predicted room-temperature electrical conductance of a n-doped graphene/BPDT/Au junction (blue) and a p-doped graphene/BPDT/Au (pink), and Au/BPDT/Au (yellow) in units of G_0. The predicted ratio of conductance per molecule for graphene/BPDT/Au to Au/BPDT/Au depends on the doping of the graphene and on precise location of the Fermi energy E_F relative to the frontier orbitals of the molecule. However, over a range of such values in the vicinity of the DFT-predicted Fermi energy the ratio varies from 10^{-2} to 10^{-3}. 74

5.4 The current at a given source and gate voltage is obtained by integrating the transmission curve $T(E, V_G, V_D)$ over energies between E_F^{Gold} to $E_F^{Gold} - |e|V_D$. 76

5.5 Four possible scenarios for the dip and asymmetry in dI/dV curve of $Gr/SAM/Au$ devices. The transport and graphene are (a) LUMO and p-doped ($E_{Dirac} = 0.1$ and $\varepsilon_m = 0.5$) (b) LUMO dominated, n-doped ($E_{Dirac} = -0.1$ and $\varepsilon_m = 0.5$) (c) HOMO dominated, n-doped ($E_{Dirac} = -0.1$ and $\varepsilon_m = 0.5$) and (d) HOMO dominated, p-doped ($E_{Dirac} = +0.1$ and $\varepsilon_m = 0.5$). For all four scenarios $\Gamma_0 = 0.1$, $\alpha = 1$ and $z = 1$. In each quadrant, the transmission coefficient $T_e(E)$ vs energy $E - E_F^{Gold}$ (the energy, relative to the Fermi energy of the gold) is plotted at various drain voltages V_D (top graph), the differential conductance (dI/dV) and the current (I) verses the drain voltage are plotted (middle graphs left and right, respectively) and a schematic showing the position of the Fermi energy of the gold relative to graphene (bottom diagram). . . 78

5.6 Four possible scenarios for the dip and asymmetry in dI/dV curves. All parameters are the same as 5.5 except for the exponent in equation 5.6, $z = 2$. 79

5.7 (a) The theoretical model (red) fit to the experimental dI/dV (blue) for the parameters, $\Gamma_0 = 0.003$, $\alpha = 1$, $\gamma_0 = 0.002$, $\gamma_1 = 1$, $\varepsilon_m = 0.1$ and $-0.1 < E_0^{Dirac} < 0.4$. (b) The differential conductance characteristics of IA3 (minimum indicated by blue arrows). (c) KFM work function mappings of device IA3 with respect to the gold tip. (d) The corresponding statistical analysis of the work function across the junction area on BPDT of IA3 as well as one of the areas where graphene lies on the SiO_2. (e) Optical images of the mapped graphene areas on IA3. (f) Corresponding statistical analysis of G band position. 80

5.8 (a) n-doped and (b) p-doped graphene at zero bias voltage with 16 K points in the transverse direction. 83

5.9 (a) Transport through a SAM with p-doped and n-doped graphene at zero bias voltage. (b) The logarithm of transmission vs the energy relative to the Fermi energy of gold at various source drain voltages. (c) Comparison between experimental and theoretical current (d) comparison of the average calculated dI/dV for differently doped systems (blue) with the experimental dI/dV (red). The units of conductance and current used in these plots are $G_0 = e^2/h$ and $I_0 = 2e/h$. Although the asymmetry and the lowest conductance point in curve is similar to the experimental data, the absolute value of the calculated conductance is greater than that of experiment, in common with DFT transport calculations reported in the literature and therefore the vertical axes have been scaled to aid comparison. 84

6.1 Schematic illustration of the vertical molecular tunnel transistor. (a) Schematic illustration of the device structure for the fabricated device. (b) Schematic diagrams of the molecular transistor with OPE3 SAMs and ionic liquid (DEME-TFSI) gating. DEME+ ions are the cations and TFSI- ions comprise the anions. (c) Chemical structure of the PCP and OPE3 molecules. 89

6.2 Schematic structures for theoretical calculation. (a) Simulating PCP SAM with gold and graphene electrodes. $K = 30$ k-points are employed in the direction indicated. (b) The structure for a single PCP junction. (c) Band structure of the graphene using 30 transverse k-points 90

6.3 (a) Schematic band diagram of the device with changed V_D at graphene electrode. (b) Schematic illustration of the working device with electrical double layers. (c) Schematic band diagram of the device with changed V_G. 90

6.4 Charge transport in gold/molecule/gold junctions. (a) Schematic illustration of the PCP and OPE3 junctions. (b) Transmission functions $T(E)$ for PCP (purple) and OPE3 (blue). 92

6.5 PCP and OPE3 molecular orbitals, (a) The Molecular orbitals for OPE3 (b) Molecular orbitals for PCP. 93

6.6 Charge transport in molecular junctions. (a) Schematic illustration of the PCP and OPE3 junctions. (b) Transmission functions $T(E)$ for PCP (purple) and OPE3 (orange). (c) Plots of experimental current density (J_D) versus bias voltage (V_D) for PCP and OPE3. (d) Differential conductance (dJ/dV) to V_D plots for experimental PCP and OPE3. (e) Theoretical current (I_D) to V_D plots for PCP and OPE3. (f) Theoretical differential conductance (dI/dV) to V_D plots for PCP and OPE3. 94

6.7 Experimental gating charge transport in molecular transistors. (a, d) Experimental J_D versus V_D characteristics for PCP and OPE with V_G changing from -1 to $1V$ with step of $0.5V$ (b, e) Experimental dJ/dV versus V_D characteristics for PCP and OPE (colour code for gate voltages are consistent with panel a)(c,f) Two-dimensional visualization of dJ/dV plotted versus V_G and V_D for PCP. 95

6.8 Gate dependent transmission for molecular transistors. Transmission functions $T(E)$ for PCP (a) and OPE3 (b) with V_G changing from -0.6 to $0.6V$ at step of $0.3V$. 97

6.9 Theoretical gating charge transport in molecular transistors. (a, d) Transmission coefficient $T(E)$ versus for PCP and OPE3 junctions for $-0.4 < V_D < 0.4$ with steps of $0.2V$. (b, e) Gate dependent theoretical $I_D - V_D$ characteristics for PCP and OPE3. (c, f) Gate dependent theoretical $dI/dV - V_D$ for PCP and OPE3. V_G is varied from $-0.6, -0.3, 0.0, 0.3$ to $0.6V$ in b,e,c,f. 98

6.10 Experimental transfer characteristics for the vertical molecular transistors with (a) PCP and (c) OPE3. (b, d) On-off ratio for PCP and OPE devices. 98

6.11 Theoretical transfer characteristics for the vertical molecular transistors with (a) PCP and (c) OPE3. (b, d) On-off ratio for PCP and OPE devices. V_D is varied from $-0.1, -0.2, -0.4, -0.6 to -0.8V$ in a and c. 99

7.1 Structures of the studied molecules. (a) A sketch of an anthanthrene core with connectivities $7, 2'$ and $1, 5'$ (the numbering system is chosen for mathematical convenience and does not coincide with standard chemical notation). (b) Chemical realisations of molecules with anthanthrene cores. 1 corresponds to the $7, 2'$ connectivity, while 2 and 3 correspond to the $1, 5'$ connectivity. $R' = 4 - (2 - ethylhexyloxy) phenyl, R = -OC_8H_{17}$. 104

7.2 (a) Transmission coefficient for the connectivities in figure 7.1a for a tight-binding model. (b) The ratio of the transmission coefficients. The conductance ratio for the connectivities discussed in figure 7.1a is 81.[185] 105

7.3 Schematic illustration of the vertical molecular tunnelling transistor. (a, b) Schematic illustration for the setup of the device with vertical ionic liquid gate through graphene layer to SAMs and molecular structures for DEME+ cation and TFSI- anion. (c) Optical photograph of the device with ionic liquid gate. 106

7.4 Charge transport in molecular junctions. (a) Schematic illustration of molecular junction 1, 2 and 3, where the side chains of molecules are hidden. (b) Transmission functions $T(E)$ for 1 (red), 2 (green) and 3 (blue). (c) Plots of experimental current density (J_D) vs. bias voltage (V_D) for 1, 2 and 3. (d) Experimental differential conductance (dJ/dV) vs. V_D. (e) Theoretical current (I_D) vs. V_D. (f) Theoretical differential conductance (dI/dV) vs. V_D. 107

7.5 The local density of states for the anthanthrene core of the molecule 1, 2 and 3 of Figure 1. The wavefunction of the HOMO and the LUMO energy levels of the core suggests that neither of the connectivities suggested in Figure 1 lead to inter-orbital destructive quantum interference.[22] 108

7.6 Gating charge transport in molecular transistors. (a, d, g) J_D vs. V_D characteristics for 1 (a), 2 (d), and 3 (g) with gate voltage (V_G) changing from -1 to $1V$ with step of $0.5V$. Insets show schematics of the 1, 2 and 3 transistors with applied vertical electric field. (b, e, h) dJ/dV vs. V_D characteristics for 1 (b), 2 (e), and 3 (h) with V_G changing from -1 to $1V$ with step of $0.5V$. (c, f, i) Two-dimensional visualization of dJ/dV vs. V_G and V_D for 1 (c), 2 (f), and 3 (i). 110

7.7 (a) The structure of gold/molecule/gold junction 1, 2 and 3 for simulation. (b) Transmission coefficient for gold/molecule/gold junctions for molecule 1(red), 2 (green) and 3 (blue). At $E - E_F^{mid-gap} = 0eV$, the ratio of $\frac{T_1}{T_2} = 203$, $\frac{T_2}{T_3} = 52$. 110

7.8 Working mechanism for vertical molecular transistors. Transmission coefficient $T(E)$ vs. $E - E_F^{mid-gap}$ for molecular junction 1 (a), 2 (d) and 3 (g) for $-0.4 < V_D < 0.4$ with steps of $0.13V$ (red for $V_D = 0.4V$). Insets show the structures of molecular junctions for simulation. Gate dependent theoretical $I_D - V_D$ characteristics for 1 (b), 2 (e) and 3 (h) for $-0.6 < V_G < 0.6$ with steps of $0.2V$ (red for $V_G = 0.6V$). Gate dependent theoretical $dI/dV - V_D$ characteristics for 1 (c), 2 (f) and 3 (i) for $-0.6 < V_G < 0.6$ with steps of $0.2V$ (red for $V_G = 0.6V$). 112

7.9 Transfer characteristics for the vertical molecular transistors. ($a-c$) Experimental transfer characteristics for 1 (a), 2 (b) and 3 (c). ($d-f$) Theoretical transfer characteristics for 1 (d), 2 (e) and 3 (f). V_D is varied from -0.1, -0.2, -0.4, -0.6 to -0.8 V in ($a-f$). 113

A.1 General scattering problem: Green object is the scatterer, the Hamiltonian of which is represented by h. The wavefunction in scattering region is f_j in the left lead is ψ_j and in the right lead is ϕ_j. The on-site energies in the leads are ε_0 and the hopping integral elements are $-\gamma$. The coupling between left and right leads are represented as $-\gamma_L$ and $-\gamma_R$. 145

A.2 A Breit-Wigner resonance: the demonstration of level broadening due to the imaginary part of the self-energy (Γ) and the shift in the resonances due to the real part of the self energy(σ). 152

B.1 A perfect doubly infinite 1D chain with on-site energies of ε_0 and hopping elements of γ. 153

B.2 The Retarded Green's function of an infinite one dimensional lattice. The excitation at $j = l$ causes the wave to propagate to the left and right with amplitudes A and B 154

B.3 Advanced Green's function corresponds to the boundary condition where two incoming waves disappear at the point of excitation . . . 156

B.4 A scattering problem where the scatterer has N sites and is connected to two leads. 156

C.1 The scatterer can be defined as a perturbation (H_S) to the doubly infinite chain (H_O). 158

C.2 Infinite chain with a single impurity. 161

C.3 Infinite chain with a 2×2 impurity. 162

C.4 The special case where $\varepsilon_1 = \varepsilon_2 = \varepsilon_0$ and $\alpha = 0$, which yields to two semi-infinite leads. 163

D.1 Fermi distribution of charges in a hot (red) and cold (blue) lead. . . 166

Chapter 1

Introduction

Molecular electronics studies electronic structures and charge transport across devices in atomic scales. These devices can vary from single molecules to multiple molecules, carbon nanotubes and other atomic structures.[1–3] The first molecular electronic device was the Avriam and Ratner rectifier in 1974 where they considered placing a single molecule consisting of electron donor and accepter compartments between two metal electrodes and showed that the transport properties of this device are controlled by the properties of this molecule.[4] Later in 1980s the invention of scanning tunneling microscope (STM)[5] and atomic force microscope (AFM)[6] led to further recognition of this field. Devices with molecular building blocks have a broad range of applications in various fields such as transistors,[7–10] switches,[11,12] rectifiers,[13,14] interconnects,[15,16] sensors,[17,18] memories[19,20] and photovoltaics.[21]

The attraction of single-molecule electronics has arisen from their potential for sub-10nm electronic switches and rectifiers and from their provision of sensitive platforms for single-molecule sensing.[22–43] Moreover, molecular recognition can lead to carefully designed molecules which provide tunable transport and desirable electronic properties.[44–47]

Molecular electronics has been advancing rapidly in the past 40 year both exper-

imentally and theoretically. Powerful experimental methods have been developed to study devices at the single molecule scale such as mechanically controlled break junctions,[48–50] STM break junctions[51] and conductive atomic force microscopy.[52] Theoretical methods have also developed hand in hand with the experiments.[53,54] Development of Density functional theory (DFT) provided a method for studying finite systems[55] or perfectly periodic systems.[56] Later combining DFT with Green's function methods allowed for studying small systems (molecules) that are connected to a continuum (electrodes).[57–59] Today, availability of computational resources has made DFT one of the most reliable and widely used methods for calculating the electronic structure of atomic structures. This provides an excellent platform for initiating charge transport calculation in molecular devices. Together, these methods allow us to understand basic properties at the molecular scale and explore their potential use as a basic building block for next generation nano-electronic devices.

One of the main applications of the field of molecular electronics is power generation from waste heat. In recent years, the potential of self-assembled monolayers for removing heat from nano-electronic devices and thermoelectrically converting waste heat into electricity has been recognized.[43,60–69] This is achieved through the seebeck effect dicovered in 1821 by T. J. Seebeck who showed two different metals in a junction would deflect a compass magnet when connected to heat baths of different temperatures.[70] The reverse phenomena is known as Peltier effect which describes the emission of heat by current traveling through two different contacting metals. The efficiency of a material in converting heat to electricity depends on several factors. Firstly, it depends on the electrical (G) and thermal (κ) conductivity of the material. Secondly, The Seebeck coefficient also known as thermoelectric sensitivity (S) which is a meausre of the thermoelectric voltage induced in response to a temperature difference across that material. Finally, the thermoelectric efficiency depends on the tempreture difference applied accors the material. Therefore the thermoelectric efficiency is often describe using the

thermoelectric figure of merit, $ZT = GS^2T/\kappa$.

The combined electricity consumption of IT systems (communication networks, personal computers, data centres, etc.) was 900 TWh in 2012, or 4.6% of global electricity use, and this figure is set to double by 2025.[71] To meet this challenge, research laboratories around the world are competing to create high-performance thermoelectric materials, starting from single molecules[22–43] and scaling up to self-assembled molecular films (SAMs).[60–66,72–75]

The ZT record for inorganic materials is $ZT \approx 2.2$ at temperatures over 900 K.[68,69] However, this low level of efficiency means that the widespread use of thermoelectricity for energy harvesting is not economic. Organic thermoelectric materials may be an attractive alternative, but at present the best organic thermoelectric materials have a $ZT = 0.42$ at room temperature,[76,77] which is still too low. To overcome this barrier, several groups are now attempting to identify design strategies for optimising the thermoelectric properties of single molecules, with a view to subsequent translation of their enhanced functionality to self-assembled molecular layers.

To approach a commercially feasible state for such devices which requires not only size reduction but also efficiency, the meaningful design of molecules as the active components is necessary. In this thesis we study molecular junctions with the focus of improving their thermoelectric efficiency. We approach this problem by first representing a design strategy to minimise the phonon transport through single molecules. Secondly we move to improve electrical conductance of single molecules through doping and chemical modification. Finally we combine the obtained knowledge to design and simulate SAM devices.

This thesis is organised as follows: In the second chapter we discuss the theoretical background for simulating molecular devices and studying their electrical and thermal conductance. The proof and derivation details of some sections is provided in the appendices A to D. These chapters will provide the necessary theoretical

background for understanding our results which are presented in chapters three, four, five, six and seven. Appendix E presents a computer script to accompany results in chapter five. The sixth chapter is dedicated to the conclusion.

Chapter 2

Methodology

Theoretical condensed matter physics aims to understand the electronic properties of materials by formulating their very fundamental building blocks, electrons and nuclei. The interactions between electrons and nuclei result in an extraordinary range of properties in molecules, solids, polymers, 2D-materials, etc., which has intrigued the curiosity of many physicists in the past. Electronic transport, in particular has been a very successful branch of condensed matter which has received a great deal of attention. However, the enormity of the number of these interactions as well as computational limits of our time makes theoretical condensed matter a very challenging field. In the past 50 years, physicist have approached this problem creating different methods of various accuracy, impact and scale. Some of these methods are **M**olecular **D**ynamics (MD), **D**ensity **F**unctional **T**heory (DFT), **M**onte **C**arlo (MC) , **Q**uantum **M**onte **C**arlo (QM) and **T**ight **B**inding theory (TB).[78–80]

As discussed in the Introduction, our aim is to study the transport of electrons and phonons through single molecules when connected to electrodes. To achieve this goal, we have utilised DFT and tight binding methods to describe our systems. Furthermore, to obtain electron transport through such systems, we use the **E**quilibrium **G**reen's **F**unction (EGF) approach explained in section 2.7 in detail.

2.1 Many-body problem

In the field of theoretical solid state physics, in order to gain access to the observable properties of a system comprising of many atoms, it is desirable to find the solution to the Schrödinger equation (Eq. 2.1)

$$\widehat{H}\Psi_i(\mathbf{r},\mathbf{R}) = E_i\Psi_i(\mathbf{r},\mathbf{R}), \tag{2.1}$$

where the wavefunction is a function of electronic ($\mathbf{r}$) and nuclear ($\mathbf{R}$) coordinates. In order to achieve this goal one needs a full description of the electronic structure of the system, which is given by the Hamiltonian operator. For an interacting system of electrons and nuclei similar to figure 2.1, the Hamiltonian operator can be written as the sum of the kinetic energies of the electrons and nuclei ($\widehat{T}$) and the Coulomb interactions between them ($\widehat{V}$) as follows:

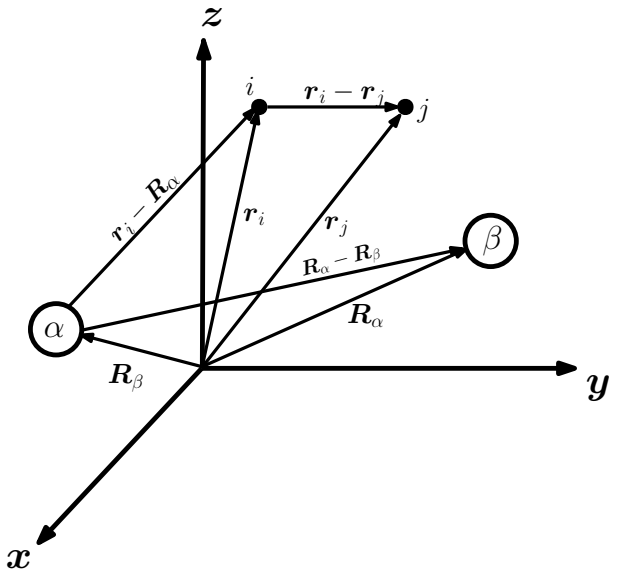

Figure 2.1: A schematic description of a many body problem. i and j are electronic labels. α and β are the nuclei labels. $\mathbf{r}$ and $\mathbf{R}$ denote the vector coordinates of the electrons and nuclei respectively.

$$\widehat{H} = \underbrace{\sum_i \frac{\hbar^2}{2m_e}\nabla_i^2}_{\widehat{T}_e} - \underbrace{\sum_\alpha \frac{\hbar^2}{2M_A}\nabla_\alpha^2}_{\widehat{T}_n} + \underbrace{\sum_{i\neq j} \frac{e^2}{|\mathbf{r}_i - \mathbf{r}_j|}}_{\widehat{V}_{e-e}} + \underbrace{\sum_{\alpha\neq\beta} \frac{Z_\alpha Z_\beta e^2}{|\mathbf{R}_\alpha - \mathbf{R}_\beta|}}_{\widehat{V}_{n-n}} - \underbrace{\sum_{i,\alpha} \frac{Z_\alpha e^2}{|\mathbf{r}_i - \mathbf{R}_\alpha|}}_{\widehat{V}_{e-n}}, \tag{2.2}$$

where M_α, $\mathbf{R}_\alpha$ and $Z_\alpha e$ are the mass, coordinates and the charge of the α^{th} nucleus. Similarly, m_e, $\mathbf{r}_i$ and $-e$ are the mass, coordinates and the charge of the i^{th} electron. In what follows we have adopted the Hartree atomic units ($e = \hbar = m_e = 4\pi\varepsilon_0 = 1$) for simplicity. Clearly for any system with more than a few electrons and nuclei, finding the eigenstates and eigenvalues of the Schrödinger equation becomes impractical. To reduce the size of this problem, one can employ the traditional Born-Oppenheimer approximation which assumes that due to the large mass of nuclei, $\widehat{T}_n \ll \widehat{T}_e$. This allows us to split the electronic and nuclear motions.

2.2 Born-Oppenheimer approximation

The Born-Oppenheimer approximation assumes that the masses of the nuclei are large in comparison with the electrons and therefore their kinetic energy ($\widehat{T}_n$) is negligible in comparison.[81] Therefore we can rewrite the Schrödinger equation for electronic Hamiltonian:

$$\widehat{H}_e \psi_i(\mathbf{r};\mathbf{R}) = E_i^e(\mathbf{R})\psi_i(\mathbf{r};\mathbf{R}), \tag{2.3}$$

where the electronic Hamiltonian is given by,

$$\widehat{H}_e = -\sum_i \frac{\hbar^2}{2m_e}\nabla_i^2 + \sum_{i\neq j}\frac{e^2}{|\mathbf{r}_i - \mathbf{r}_j|} + \widehat{V}_{ext}. \tag{2.4}$$

In the equation above, $\widehat{V}_{ext}$ represents an external potential acting on the electrons due to the frozen nuclei. This function varies for each nuclear arrangement. Therefore, the electronic wavefunction ($\psi(\mathbf{r};\mathbf{R})$) does not explicitly depend on nuclear coordinates. As a result, we can decouple the electronic and nuclear wavefunction in the total wave function. Hence the total wave function reads,

$$\Psi_i(\mathbf{r},\mathbf{R}) = \sum_j \sigma_{ij}(\mathbf{R})\psi_j(\mathbf{r};\mathbf{R}), \tag{2.5}$$

where $\sigma_{ij}(\mathbf{R})$ describe the nuclear motion and is solely determined by solving a nuclear equation.

2.3 Density functional theory

Density **F**unctional **T**heory (DFT), is one of the most commonly used approaches today for solving the many-body problem we introduced in equation 2.4.[78,79] This method was first introduced by Hohenberg and Kohn in 1964 who showed that the ground state energy of a system of interacting electrons is a unique functional of the electronic charge density.[82] Later in 1965 Kohn and Sham provided a method to relate the ground states of a system with interacting particles to a non-interacting particles system through their charge density.[83] In the next two sections we describe these methods in detail.

2.3.1 The Hohenberg-Kohn theorems

The **H**ohenberg-**K**ohn (HK) theorem is the foundation of density functional theory and applies to any system of electrons moving in an external potential. In this theorem the ground state energy of a fully interacting N-electron system is described via its electron density ($\rho(\mathbf{r})$) which reduces the size of the problem considerably.[82]

$$\rho(\mathbf{r}) = \int_i^N \psi(\mathbf{r})\psi^*(\mathbf{r}) \tag{2.6}$$

The Hohenberg-Kohn theorem consists of two simply stated theorems. These two theorem are based on the fact that two many-body problems can be different via external potential and/or the number of particles in them.

- **Theorem 1.** The first theorem states that there is a unique correspondence between the external potential ($V_{ext}(\mathbf{r})$) of the many-body Hamiltonian and

the corresponding ground state electronic density. This can be easily proven using contradiction. We start from the assumption that two potentials $V_{ext}(\mathbf{r})$ and $V'_{ext}(\mathbf{r})$ which differ by more than a constant give rise to the same density $\rho(\mathbf{r})$, yielding two different Schrödinger equations using resultant $\widehat{H}$ and $\widehat{H}'$. Variational principle states that the energy is minimal with respect to a variation of the wave function, and is an upper bound to the ground state energy. Assuming that the total energy from one of the Schrödinger equations corresponds to the ground state, we have

$$E_0 = \left\langle \psi_0 \left| \widehat{H} \right| \psi_0 \right\rangle < \left\langle \psi'_0 \left| \widehat{H} \right| \psi'_0 \right\rangle . \tag{2.7}$$

This arises from the difference between the two Hamiltonians,

$$\left\langle \psi_0 \left| \widehat{H} \right| \psi_0 \right\rangle = \left\langle \psi_0 \left| \widehat{H}' \right| \psi_0 \right\rangle + \langle \psi'_0 \left| V_{ext}(\mathbf{r}) - V'_{ext}(\mathbf{r}) \right| \psi'_0 \rangle \tag{2.8}$$

Therefore we can write,

$$E_0 < E'_0 + \langle \psi_0 \left| V_{ext}(\mathbf{r}) - V'_{ext}(\mathbf{r}) \right| \psi_0 \rangle , \tag{2.9}$$

where the difference between the two potentials is a direct consequence of the inequality. Similarly we can write,

$$E'_0 < E_0 - \langle \psi_0 \left| V_{ext}(\mathbf{r}) - V'_{ext}(\mathbf{r}) \right| \psi_0 \rangle . \tag{2.10}$$

Adding the above two inequalities we have ,

$$E'_0 + E_0 < E_0 + E'_0 + \langle \psi_0 \left| V_{ext}(\mathbf{r}) - V'_{ext}(\mathbf{r}) \right| \psi_0 \rangle - \langle \psi_0 \left| V_{ext}(\mathbf{r}) - V'_{ext}(\mathbf{r}) \right| \psi_0 \rangle . \tag{2.11}$$

Since we assume that both potentials have the same corresponding electron densities, $\rho(\mathbf{r})$, the two terms on the right hand side add up to zero,

$$\int d^3\mathbf{r}\rho(\mathbf{r})\left[V_{ext}(\mathbf{r}) - V'_{ext}(\mathbf{r})\right] - \int d^3\mathbf{r}\rho(\mathbf{r})\left[V_{ext}(\mathbf{r}) - V'_{ext}(\mathbf{r})\right] = 0, \quad (2.12)$$

resulting in $E'_0 + E_0 < E_0 + E'_0$ which is wrong. Therefore we can conclude that the potential $V_{ext}(\mathbf{r})$, must be unique. This conclusion allows us to write the total energy as a function of the electron density,

$$E\left(\rho(\mathbf{r})\right) = \int V_{ext}(\mathbf{r})\rho(\mathbf{r})d\mathbf{r} + \underbrace{\left\langle \psi_0 \left| \widehat{T} + \widehat{V} \right| \psi_0 \right\rangle}_{F[\rho(\mathbf{r})]}, \quad (2.13)$$

where $F[\rho(\mathbf{r})]$ is a unique and universal functional of the electron density which does not depend on the external potential.

- **Theorem 2.** Hohenberg showed that the minimum of the energy functional $E\left(\rho(\mathbf{r})\right)$ can be obtained variationally from

$$E\left(\rho(\mathbf{r})\right) = \left\langle \psi \left| \widehat{H} \right| \psi \right\rangle > E_0\left(\rho(\mathbf{r})\right). \quad (2.14)$$

$E\left(\rho(\mathbf{r})\right)$ is at its minimum only and only if $\rho(\mathbf{r})$ is the ground state charge density and all ground state properties of a many-body system can be obtained from $\rho(\mathbf{r})$. Therefore evaluating the following equation will lead us to the ground state charge density,

$$\frac{\delta E[\rho(\mathbf{r})]}{\delta \rho} = 0. \quad (2.15)$$

In order to evaluate the above energy one requires to describe the density functional ($F[\rho(\mathbf{r})]$) which could depend on properties such as polarization. Unfortunately the exact form of this functional is unknown and the accuracy of a DFT calculation depends on the approximations made to obtain $F[\rho(\mathbf{r})]$.

2.3.2 Kohn-Sham equation

The Kohn-Sham approach is a self-consistent method which describes an interacting system of electrons, using a auxiliary non-interacting system in an effective potential ($V_{eff}(\mathbf{r})$) which yields the same ground state charge density ($\rho(\mathbf{r})$) as the original problem.[83,84] The effective potential is as follows,

$$V_{eff}(\mathbf{r}) = \int d\mathbf{r}' \frac{e^2\rho(\mathbf{r}')}{|\mathbf{r}-\mathbf{r}'|} + V_{ext}(\mathbf{r}) + V_{xc}(\mathbf{r}), \tag{2.16}$$

where the first term is the electrostatic energy (referred to as Hartree energy), V_{ext} is the external potential due to the presence of stationary nuclei and V_{xc} is the exchange-correlation potential which describes the remaining contribution of interacting electrons to the exact energy of the system and is the derivative of exchange energy,

$$V_{xc}(\mathbf{r}) = \frac{\delta E_{xc}\left(\rho(\mathbf{r})\right)}{\delta\rho(\mathbf{r})}. \tag{2.17}$$

Therefore the Kohn-Sham Hamiltonian reads,

$$\widehat{H}^{KS}\phi_i(\mathbf{r}) = \left[\frac{-\nabla^2_{\mathbf{r}}}{2m_e} + V_{eff}(\mathbf{r})\right]\phi_i(\mathbf{r}) = \epsilon_i\phi_i(\mathbf{r}). \tag{2.18}$$

$\widehat{H}^{KS}$ isolates the kinetic energy of individual particles which interact individually with an effective potential and ϵ_i are the eigenvalues of such system. Note that the eigenvalues obtained from the Kohn-Sham equations are auxiliary and do not carry quantitative information.[84] $\phi_i(\mathbf{r})$ are the Kohn-Sham wavefunctions which describe the motion of i^{th} particle in an effective potential ($V_{eff}(\mathbf{r})$). The dependency of $V_{eff}(\mathbf{r})$ on the $\rho(\mathbf{r})$ results in the self-consistency of the Kohn-Sham method.

2.3.3 Exchange-correlation functional

The electronic wavefunction must satisfy the Pauli-exclusion principle meaning that electrons of a given spin are surrounded by a region where the density of

electrons with the same spin is reduced. Keeping the electrons of the same spin away from each other is referred to as exchange interaction and it reduces the Coulomb repulsion in equation 2.16. The correlation energy is the remaining difference to the exact total energy of the system with interacting electrons. A crude explanation is that the motion of one electron is affected by the motion of other electrons in a correlated system and the correlation energy compensates for the lack of this effect in a non-interacting system. These two corrections to the Hartree energy are commonly known as the 'exchange-correlation hole' that surrounds every electron in the system. Since it is not possible to find the exact form of the exchange-correlation energy, approximation is inevitable and the quality of this approximation determines the accuracy of a DFT calculation.[84] The simplest approximation for the xc-functional is the **L**ocal **D**ensity **A**pproximation (LDA) which derives the E_{xc} from the local electron density, assuming that electrons behave like a homogeneous gas:[85]

$$E_{xc}^{LDA}\left(\rho(\mathbf{r})\right) = \int \rho(\mathbf{r}) \epsilon_{xc}^{hom}\left(\rho(\mathbf{r})\right) d\mathbf{r}, \tag{2.19}$$

where ϵ_{xc}^{hom} is the xc energy of the homogeneous gas with a density of $\rho(\mathbf{r})$. This approximation is accurate for slowly varying electron densities. Despite the simplicity of LDA functional, it has been used in this work when the accuracy has been satisfactory.

The LDA functional can be improved by including the gradient of the density ($\nabla\rho$) which takes into account more of the non-local many body effects (Eq. 2.20). This is known as the **G**eneralised **G**radient **A**pproximation (GGA) of the xc-functional,[86,87]

$$E_{xc}^{GGA}\left(\rho(\mathbf{r})\right) = \int \rho(\mathbf{r}) \epsilon_{xc}^{LDA} F_{xc}\left(\rho, |\nabla\rho|\right) d\mathbf{r}. \tag{2.20}$$

In the above expression for GGA xc-functional (E_{xc}^{GGA}), F_{xc} is a function of the electron density and its gradient. GGA produces better results when itcomes to structural properties and is used in this work when necessary.

2.4 Motion of nuclei

Once the electronic state is obtained from equation 2.18 within the Born-Oppenheimer approximation, we can then obtain evolution of the nuclei coordinates in time. Since electronic motion is very fast in comparison with the nuclei, their coordinates can be replaced by their average value. Therefore we can describe the motion of nuclei in an average field of electrons. Assume there is a nuclear wave function which gives the minimum expectation value of the nuclear Hamiltonian

$$\begin{aligned} E_0^{tot}(\mathbf{R}) &= \left\langle \psi_0 \left| \widehat{H}(\mathbf{R}) \right| \psi_0 \right\rangle \\ &= \left\langle \psi_0 \left| -\sum_{\alpha}^{M} \frac{1}{2M_\alpha} \nabla_\alpha^2 \right| \psi_0 \right\rangle + E_e(\mathbf{R}_\alpha) + \left\langle \psi_0 \left| \sum_{\alpha}^{M} \sum_{\beta}^{M} \frac{Z_\alpha Z_\beta}{R_{\alpha\beta}} \right| \psi_0 \right\rangle \\ &= \left\langle \psi_0 \left| -\sum_{\alpha}^{M} \frac{1}{2M_\alpha} \nabla_\alpha^2 \right| \psi_0 \right\rangle + E_e(\mathbf{R}_\alpha) + E_n(\mathbf{R}_\alpha) \end{aligned} \tag{2.21}$$

Once the ground state energy is found, we can derive the forces using Hellmann-Feynman theorem. The equilibrium geometry of a system with several atoms ($\mathbf{R}_0$), then is found by evaluating the equation below,

$$F_A(\mathbf{R}_{eq}) = -\left. \frac{\partial E_{eq}}{\partial \mathbf{R}_A} \right|_{\mathbf{R}=\mathbf{R}_0} = 0. \tag{2.22}$$

This process is referred to as geometry relaxation (or geometry optimisation) within this work.

2.5 SIESTA implementation of DFT

The **S**panish **I**nitiative for **E**lectronic **S**imulations with **T**housands of **A**toms (SIESTA) code is a well known implementation of the DFT method.[88] SIESTA uses periodic boundary conditions to solve the Kohn-Sham equations which is suitable for studying crystals and in our case metallic electrodes. The supercell is represented utilising Bloch's theorem in this code where the single particle wavefunction for

band j is,

$$\psi_{j,\mathbf{k}}(\mathbf{r}) = e^{i\mathbf{kr}} u_{j,\mathbf{k}}(\mathbf{r}), \tag{2.23}$$

where $\mathbf{k}$ is the reciprocal lattice vector in the first Brillouin zone and $u_{j,\mathbf{k}}(\mathbf{r})$ is the lattice periodic function. Therefore equation 2.18 can be solved for each $\mathbf{k}$-point to obtain a set of Kohn-Sham eigenstates. In order to solve the Kohn-Sham equations, SIESTA uses various approximation schemes which are discussed in the following two sections.

2.5.1 Pseudopotential approximation

As previously discussed, the Kohn-Sham method has proved to be effective when solving many body problems. Nonetheless, solving an eigenvalue problem for a system of many atoms (such as a molecule) requires large computer time. To reduce the number of electrons, the interactions between the electrons and the ionic cores are represented by norm-conserving pseudopotentials in SIESTA according to the Troullier-Martins parametrization.[89] Pseudopotentials replace the core electrons and provide the same potential for valance electrons as these core electrons. This approximation is done on the grounds that the core electrons in an atom do not have an active role in chemical bonding and are relatively independent of the chemical environment of the atom. This approximation is shown schematically in figure 2.2.

The all-electron wavefunction (ψ_{all}) is a combination of the core and valance electrons wavefunctions and has to satisfy the orthogonality condition. Since the core states are tightly bound to the nucleus, they are localised in its vicinity. Thus, the valance states need to oscillate rapidly in the vicinity of the core in order to preserve the orthogonality constraint (dashed pink in Fig 2.2). Resultantly, the kinetic energy of the valance electrons counteracts the large potential energy due to the Coulomb interactions (-V_{eff}/r). Therefore, it is reasonable to approximate

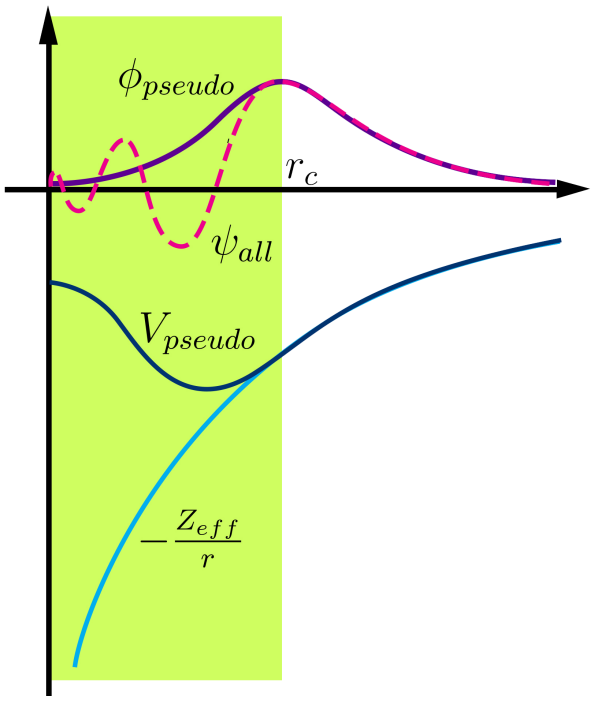

Figure 2.2: Schematic illustration of the pseudopotential approximation. All-electron potential (light blue) and pseudopotential (dark blue) converge to the the same function outside the cut-off radius (rc). This is the same for the corresponding wavefunctions (purple and pink).

the strong coulomb interaction and core electrons and introduce a pseudopotential (V_{pseudo}) which replaces the core electrons and provides the same potential for valance electrons as these core electrons. As a result the new pseudo-wavefunction (ϕ_{pseudo}) is much smoother in the vicinity of the core as shown in figure 2.2.

2.5.2 Numerical Atomic Orbitals (NAO)

Numerical atomic orbitals are localised basis sets in which the valance electronic states are **L**inear **C**ombination of **A**tomic **O**rbitals (LCAO).[90] Adoption of the LCAO method for Kohn-Sham wavefunction yields,

$$\phi_i = \sum_{j=1}^{L} c_{ji}\chi_j. \tag{2.24}$$

For an atom with total number of L orbitals, χ_j is the j^{th} atom centred orbital. To obtain a numerical solution for the Kohn-Sham equations, SIESTA employs

the LCAO method which is highly localised (short cut-off range) and therefore creates sparse Hamiltonian and overlap matrix. The variational parameters in the construction of these orbitals are the size (number of atomic orbitals per atom), range (spatial extension of the orbitals or the cut-off radius) and shape (of the radial part). These atom centred orbitals can be written as

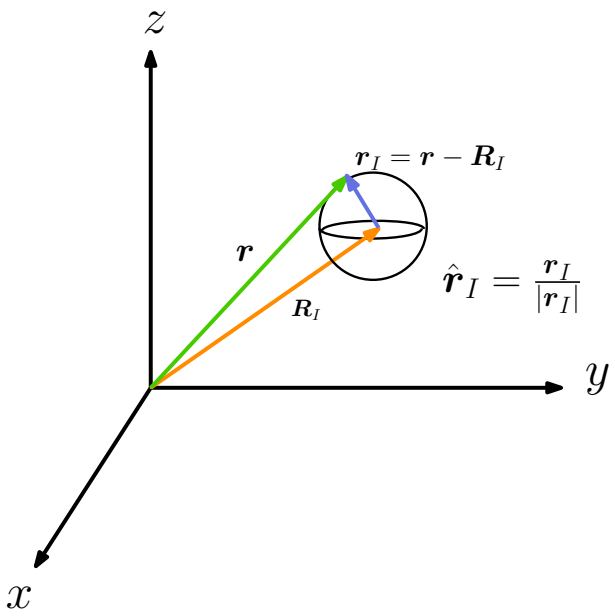

Figure 2.3: A schematic description of vector coordinates utilised to describe basis sets

$$\chi_{Ilmn}(\mathbf{r}) = R_{Iln}(|\mathbf{r}_I|)Y_{lm}(\hat{\mathbf{r}}_I). \tag{2.25}$$

Each basis set is a product of a radial wavefunction (R_{ln}) and a spherical harmonic (Y_{lm}). Where I is the index of the atom, l is the orbital angular momentum, m is the magnetic quantum number and n provides the possibility of possessing multiple orbitals for the same angular momentum numbers. The radial term can be obtained by solving the Kohn-Sham Hamiltonian for the isolated particular pseudo-atom species on a radial grid. Depending on the available time, computer power and the accuracy required one can choose the size of the basis set. The minimal basis set also known as single-ζ, has one radial function per angular momentum. Multiple-ζ basis sets have multiple orbitals (n) corresponding to the same angular momentum with different radial parts. It is also possible to have

shells of different atomic symmetry in a basis set (usually obtained by applying a small electric field to the orbital) thus introducing angular flexibility. These basis sets are referred to as multiple-ζ polarized basis sets. Throughout this work, unless stated otherwise, we have used double-ζ polarized basis set which is a good compromise between the accuracy we require and our available resources.

2.6 Dynamical matrix

In addition to the study of electronic structures and electron transport through single molecules, in this thesis we have studied the transmission probability of phonons through similar devices. The work is confined to the harmonic approximation, hence we have neglected phonon-phonon interactions. This approximation was taken into account due to the scale of our systems and the unimportance of phonon-phonon scattering effect in this scale.[91] In the harmonic approximation limit the description of vibrational properties of a system similar to figure 2.4 is purely determined by the spring constants between atom i and j in all directions. The spring constants can be presented in matrix form (Dynamical matrix) which can be used to solve the equation of motion. To obtain the Dynamical matrix of our systems we have adapted finite differences method. The following steps were taken to construct the Dynamical matrix:

- The structures are initially relaxed with a maximum residual force of 0.01 eV/Å.
- The atoms are displaced by $\mathbf{d}_{i\xi} = \pm 0.01nm$ where $\mathbf{d} = \{x, y, z\}$ as illustrated in figure 2.4 (6 displacements for each atom). For each displacement the force on all atoms was calculated using SIESTA. Note that the displacement range must be kept in the limit where the harmonic oscillation approximation is valid.

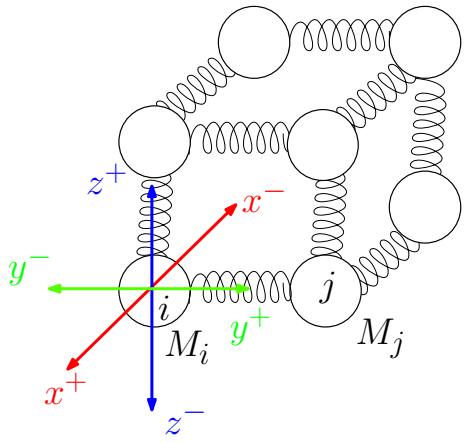

Figure 2.4: Deviation of atoms from their equilibrium position for the purpose of using finite differences method to obtain the vibrational properties of a system. M_i and M_j are the masses of the i^{th} and j^{th} atoms.

- The Hessian matrix (force constant matrix) was then constructed using the equation below.

$$K_{i\xi,j\nu} = \frac{\partial^2 E}{\partial \mathbf{d}_{i\xi} \partial \mathbf{d}_{j\nu}} = \frac{F_{j\nu}(\mathbf{d}_{i\xi}) - F_{j\nu}(\mathbf{d}_{j\nu})}{2\mathbf{d}_{i\xi}}, \tag{2.26}$$

  where E is the total energy and the force vectors were obtained from SIESTA. Considering the momentum conservation we can find the intra atomic elements using the equation below,

$$K_{i\xi,i\nu} = -\sum_{k \neq i} K_{i\xi,k\nu}. \tag{2.27}$$

- Having obtained the Hessian matrix we can easily compute the Dynamical matrix ($\mathbf{D}$) using the following equation,

$$\mathbf{D}_{i\xi,j\nu} = \frac{K_{i\xi,j\nu}}{\sqrt{M_i M_j}}, \tag{2.28}$$

  with M_i and M_j being the mass of atom i and j.

The phonon eigen-frequencies and eigen-functions are obtained by solving the equation of motion as below,

$$\mathbf{D}\phi_i = \omega^2 \phi_i. \tag{2.29}$$

2.7 Quantum theory of transport

In the macroscopic regime, where the impurities (scatterers) are distributed randomly in a material, the conductance is given by

$$G = \sigma A/L, \tag{2.30}$$

where A and L are the area and length of the conductor and σ is the conductivity. In such system, Ohm's law is applicable as the large number of scatterers reduce the collective electron drift motion. According to equation 2.30, in the limits that $A \to 0$, $G \to 0$ and if $L \to 0$, $G \to \infty$. However experiments on quantum point contacts contradict these conditions and demonstrate that Ohm's law fails on a small scale.[92,93] The characteristic lengths in which Ohm's law fails to predict the conductance are as follows:[79]

1. De Broglie wave-length λ_F: Where the width of the conductor is of the order of λ_F the problem is equivalent to a particle in a box problem and the wave like nature of electrons must be taken into account.

2. The mean free path L_m: The average distance that an electron passes without changing its momentum.

3. The phase relaxation length L_ϕ: The average distance that an electron passes without phase loss which takes place due to inelastic scattering caused by the electron-electron and electron-phonon interactions.

If the length of a conductor is not considerably larger than any of the named length scales, the wave nature of electrons play an important role in the conductance of the device. Therefore a fully quantum mechanical treatment of such devices is necessary.

Landauer was the first to suggest a formalism which established a direct relation

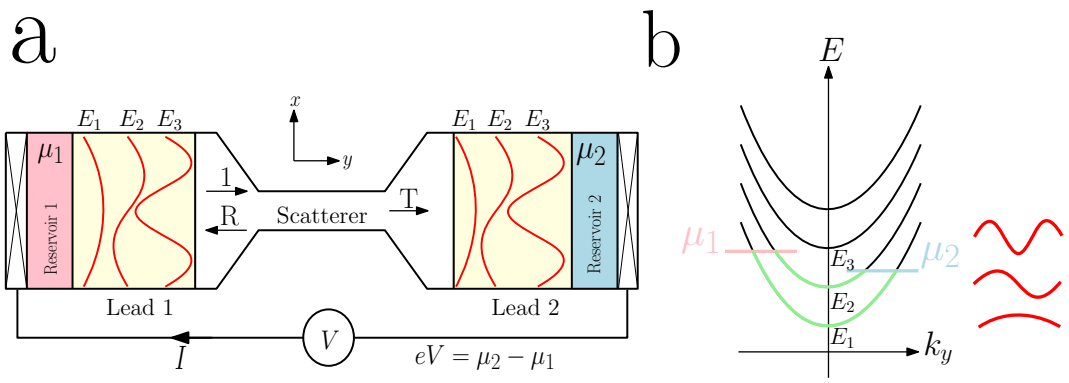

Figure 2.5: (a) Scatterer (white) placed between two leads (yellow). The leads are connected to two reservoirs with chemical potential μ_1 (pink) and μ_2 (blue) where μ_2 is elevated by eV. (b) The dispersion relation.

between the conductance and transmission probability of electrons in a one dimensional mesoscopic device. This idea was then generalised to a multi-channel (three dimensional) conductor by Fisher-Lee.[94] Later this theory was expanded by Büttiker to multi-probe devices.[95,96] The following section gives an overview of this theory.

2.7.1 The Landauer-Büttiker approach

To find the conductance of a system in the mesoscopic coherent regime, we introduce the system in figure 2.5.*a* where a scatterer (white) is attached to two leads (yellow). The transmission of electrons in the leads is ballistic therefore no energy is lost in the lead area. The leads are then connected to two reservoirs with chemical potential μ_1 (pink) and μ_2 (blue) where electrons reach thermal equilibrium. We assume that all contacts are non-reflecting therefore the reservoir are the analogue of radiative black body which absorbs electrons with no reflection and emit electrons with a constant thermal distribution. The two reservoirs are connected through contact points to a source and drain where a small voltage is applied such that the difference between the two Fermi levels is given by $eV = \mu_2 - \mu_1$. The size of the device follow the characteristic lengths, hence this problem can be treated

as a scattering problem. The conductance of this system can be written as,

$$G = \frac{I}{V} = \frac{eI}{\mu_2 - \mu_1}. \tag{2.31}$$

In what follows we derive the Landauer-Büttiker formula which allows us to calculate the current in equation 2.31. In the system introduced in figure 2.5.*a* x is the transverse and y the longitudinal direction. In the leads region, the confining potential in the x direction ($V(x)$) is a parabolic potential given by,

$$V(x) = \frac{1}{2} m^* \omega_0^2 x^2. \tag{2.32}$$

The Hamiltonian for such system can be written as,

$$H = \frac{p_x^2}{2m^*} + V(x) + \frac{p_y^2}{2m^*}. \tag{2.33}$$

Central to all quantum mechanical problems are the solutions to the Schrödinger equation. In the transverse direction the solutions are those of a harmonic oscillator (due to the presence of $V(x)$) which are shown in red in Fig. 2.5.*a*. In the longitudinal direction however, given there is no confinement, the solutions are plane waves of the form,

$$\psi(x, y) = \frac{1}{\sqrt{L}} e^{iky} \xi(x). \tag{2.34}$$

Therefore the dispersion relation ($E_n(k)$) is a parabola. The parabola associated with every mode in transverse direction is referred to as a sub-band shown in figure 2.5.*b*, also referred to as scattering channel. When the chemical potential in reservoir 1 and 2 are different, (the occupied states are highlighted by green in the sub-bands) the current from left to right is given by,

$$I = nev, \tag{2.35}$$

where e is the charge of an electron, n is the number of transported electrons and v is the group velocity. The number of incident electrons to the scattering region, must be obtained from the occupied states in the sub-bands and can be deriven from the density of states. The fraction of transmitted electrons is determined by the transmission coefficient T_n. Hence, current can be written as,

$$I = \frac{e}{2} \sum_{n=1}^{N} \int_{\mu_1}^{\mu_2} dE \cdot \frac{dN_n}{dE} \cdot v_n \cdot T_n. \tag{2.36}$$

The sum in the above equation is over all transverse sub-bands and v_n is the group velocity of the electrons in the n^{th} sub-band. The factor of $\frac{1}{2}$ accounts for the spin of electrons. The density of states and group velocity for a one dimensional propagator are given by,

$$\frac{dN_n}{dE} = \frac{2}{\pi} \left(\frac{dE_n}{dk_y} \right)^{-1} \quad , \quad v_n = \frac{1}{\hbar} \left(\frac{dE_n}{dk_y} \right), \tag{2.37}$$

substituting Eq.2.37 in Eq.2.36, I reads

$$I = \frac{2e}{h} (\mu_2 - \mu_1) \sum_{n=1}^{N} T_n. \tag{2.38}$$

Hence the conductance is,

$$G = \frac{I}{V} = \frac{2e^2}{h} \sum_{n=1}^{N} T_n. \tag{2.39}$$

According to the Landauer theory the conductance of a perfect ballistic conductor, is $\frac{2Ne^2}{h}$ which is referred to as the quantum of conductance. The experiments done on monoatomic gold wire between two gold surfaces agree with this theory.[97–99] It is important to remember that electrons which are propagating in the n^{th} channel in the left lead have a probability to propagate in the m^{th} channel in the right

lead. Therefore the transmission coefficient is,

$$T_n = \sum_m |t_{nm}|^2 , \tag{2.40}$$

where t is the transmission amplitude. Doing the sum over all channels in equation 2.39 we derive the following,

$$G = \frac{2e^2}{h} Tr(tt^\dagger). \tag{2.41}$$

Combining the transmission amplitudes with reflection amplitudes r^{nm} (i.e the probability for an electron travelling in the n^{th} channel to be reflected back in to the m^{th} channel of the same lead) we can obtain the scattering matrix,

$$S = \begin{pmatrix} r & t' \\ t & r' \end{pmatrix}, \tag{2.42}$$

where t and r are the transmission amplitudes for electrons travelling with positive momentum and t' and r' are for negative momentum. These amplitudes can be obtained using the famous Fisher-Lee relations which relate the scattering amplitudes to the surface Green's function of the system. The derivation of Fisher-Lee equations are discussed in great detail in section 2.7.2 for a multi channel system and in appendix B for a simplified single channel system.

2.7.2 Equilibrium Green's Function method

The conductance of the molecular device is an equilibrium property determined purely by the electronic structure in the equilibrium junction. The theoretical treatment of electron transport through such devices requires the combination of techniques which calculate the electronic structure (as discussed in DFT section) and use that to obtain the electron transport probabilities.

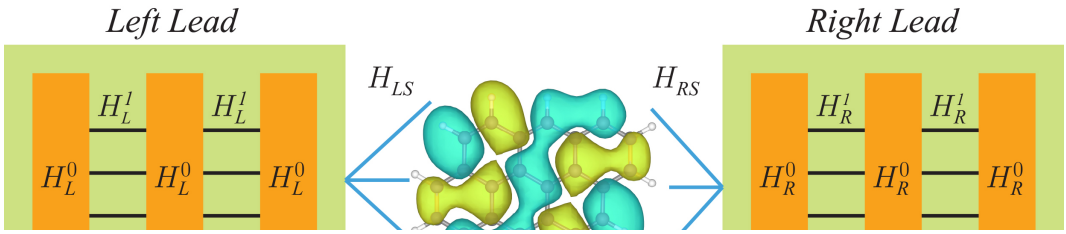

Figure 2.6: A quantum system coupled to the left (R) and right (R) leads. $\boldsymbol{H}_S$ is the non-interacting Hamiltonian of the scattering region.

In any computational study of a Lead/Device/Lead system, one faces the complication of dealing with semi-infinite Hamiltonians describing the leads. This hurdle can be dealt with using a general technique to calculate the Green's function of such system and hence convert the infinite problem to a finite problem which only involves the device and the surfaces of the leads, where all contributions from the leads are incorporated into the self-energies.[57,100,101] In this section we outline this equilibrium method which allows us to find the reflection and transmission amplitudes of the scattering matrix introduced in the previous section.

Figure 2.6 shows a scatterer placed between two leads (namely L and R). The leads are periodic and consist of principle layers ($H^0_{L/R}$) which are coupled together via a coupling matrix $H^1 L/R$. We start with Schrödinger equation of the system in figure 2.6,

$$\boldsymbol{H}\boldsymbol{\psi} = \boldsymbol{E}\mathbb{S}\boldsymbol{\psi}, \tag{2.43}$$

where $\boldsymbol{H}$ is the full electronic mean-field Hamiltonian of the system and $\mathbb{S}$ is the overlap matrix (obtained from SIESTA code in this thesis). The use of a local basis in SIESTA allows us to extract $\boldsymbol{H}$ and $\mathbb{S}$ into the following format,

$$\begin{pmatrix} \boldsymbol{H}_L & \boldsymbol{H}_{LS} & 0 \\ \boldsymbol{H}_{SL} & \boldsymbol{H}_S & \boldsymbol{H}_{RS} \\ 0 & \boldsymbol{H}_{SR} & \boldsymbol{H}_R \end{pmatrix} \begin{pmatrix} \boldsymbol{\psi}_L \\ \boldsymbol{\psi}_S \\ \boldsymbol{\psi}_R \end{pmatrix} = \boldsymbol{E} \begin{pmatrix} \mathbb{S}_L & \mathbb{S}_{LS} & 0 \\ \mathbb{S}_{SL} & \mathbb{S}_S & \mathbb{S}_{RS} \\ 0 & \mathbb{S}_{SR} & \mathbb{S}_R \end{pmatrix} \begin{pmatrix} \boldsymbol{\psi}_L \\ \boldsymbol{\psi}_S \\ \boldsymbol{\psi}_R \end{pmatrix}, \tag{2.44}$$

where $\boldsymbol{H}_{SL} = \boldsymbol{H}^\dagger_{LS}$ and $\boldsymbol{H}_{SR} = \boldsymbol{H}^\dagger_{RS}$ represent the interactions between the left(right) lead and the scattering region. It is crucial to bear in mind that $H_{L(R)}$,

$\boldsymbol{H}_{SL}$ and $\boldsymbol{H}_{SR}$ are matrices of semi-infinite dimension. Similarly $\boldsymbol{\psi}_{L(R)}$ are semi-infinite length vectors.

For mathematical convenience we rearrange the blocks of matrices in equation 2.44 such that the system is represented by two main blocks, the leads(outside) and the scattering region which are connected via a perturbation. (Fig. 2.7)

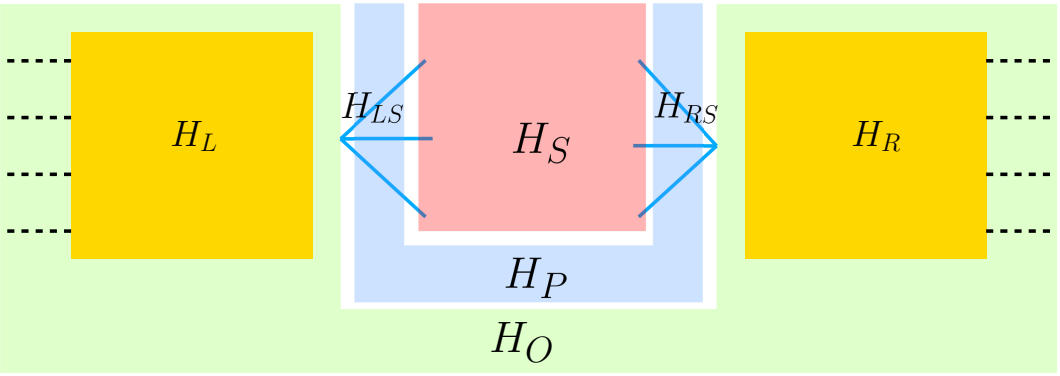

Figure 2.7: System is divided into 3 highlighted blocks. Green representing all the leads ($\boldsymbol{H}_O$), red is the scattering region ($\boldsymbol{H}_S$) and blue includes all the matrix elements connecting the leads to the scattering region ($\boldsymbol{H}^P$).

Therefore the Hamiltonian of the whole system may be represented as a 2×2 matrix,

$$\boldsymbol{H} = \begin{pmatrix} \boldsymbol{H}_O & \boldsymbol{H}^P_{OS} \\ \boldsymbol{H}^P_{SO} & \boldsymbol{H}_S \end{pmatrix}, \tag{2.45}$$

where $\boldsymbol{H}_O$ and $\boldsymbol{H}_S$ are the non-interacting units which are connected via a perturbation matrix, $\boldsymbol{H}_P$ given below,

$$\boldsymbol{H}_P = \begin{pmatrix} 0 & \boldsymbol{H}_{LS} \\ \boldsymbol{H}_{RS} & \\ \boldsymbol{H}_{LS} & \\ & \boldsymbol{H}_{RS} \\ & 0 \end{pmatrix}. \tag{2.46}$$

Note that the highlighted blocks are zero due to absence of any connection between the Left and the right lead. In general an equation of form 2.44 can be solved using the retarded Green's function (see appendix A for details). The retarded Green's

function is defined by the relation,

$$[\boldsymbol{ES} - \boldsymbol{H}]\,\boldsymbol{G}^R = \boldsymbol{I}, \tag{2.47}$$

which is related to the Green's function of the non-interacting units by the means of Dyson's equation. (proof of which is available in appendix C)

$$(\boldsymbol{g}^{-1} - \boldsymbol{H}^P)\boldsymbol{G}^R = \boldsymbol{I}, \tag{2.48}$$

where $\boldsymbol{G}^R$ is the Green's function of the perturbed system and $\boldsymbol{g}$ is the Green's function of non-interacting leads and the scattering region. (Eq. 2.49)

$$\boldsymbol{g} = \left(\begin{array}{cc|cc} \bar{\boldsymbol{g}}_L & & \multicolumn{2}{c}{\multirow{2}{*}{$\mathbf{0}$}} \\ & \bar{\boldsymbol{g}}_R & & \\ \hline \multicolumn{2}{c|}{\multirow{2}{*}{$\mathbf{0}$}} & \bar{\boldsymbol{g}}_{nn} & \bar{\boldsymbol{g}}_{nm} \\ & & \bar{\boldsymbol{g}}_{mn} & \bar{\boldsymbol{g}}_{mm} \end{array}\right) = \left(\begin{array}{c|c} \boldsymbol{g}_O & \boldsymbol{g}_{OS} \\ \hline \boldsymbol{g}_{SO} & \boldsymbol{g}_S \end{array}\right) \tag{2.49}$$

In the equation above, $\bar{\boldsymbol{g}}_L$ and $\bar{\boldsymbol{g}}_R$ are the Green's function of the left and right lead and can be easily obtained as shown in Appendix B. In the intermediate derivations the superscript R for the retarded Green's function is ignored. Substituting the matrices in Dyson's equation (Eq. 2.48) we have,

$$\begin{pmatrix} \boldsymbol{g}_O^{-1} & -\boldsymbol{H}_{OS}^P \\ -\boldsymbol{H}_{SO}^P & \boldsymbol{g}_S^{-1} \end{pmatrix} \begin{pmatrix} \boldsymbol{G}_{OO} & \boldsymbol{G}_{OS} \\ \boldsymbol{G}_{SO} & \boldsymbol{G}_{SS} \end{pmatrix} = \boldsymbol{I}. \tag{2.50}$$

Solving this matrix equation we find the following,

$$\boldsymbol{G}_{SS} = \boldsymbol{g}_S + \boldsymbol{g}_S \boldsymbol{H}_{SO}^P \boldsymbol{G}_{OO} \boldsymbol{H}_{OS}^P \boldsymbol{g}_S, \tag{2.51}$$

$$\boldsymbol{G}_{OO} = \boldsymbol{g}_O + \boldsymbol{g}_O \boldsymbol{H}_{OS}^P \boldsymbol{G}_{SS} \boldsymbol{H}_{SO}^P \boldsymbol{g}_O, \tag{2.52}$$

where the self energy is given by

$$\boldsymbol{\Sigma} = \boldsymbol{H}_{SO}^{P}\boldsymbol{g}_{O}\boldsymbol{H}_{OS}^{P} = \begin{pmatrix} \boldsymbol{H}_{LS}^{2}\bar{\boldsymbol{g}}_{L} & \mathbf{0} \\ \mathbf{0} & \boldsymbol{H}_{RS}^{2}\bar{\boldsymbol{g}}_{R} \end{pmatrix}. \tag{2.53}$$

The self-energy ($\boldsymbol{\Sigma}$) consists of a real and an imaginary part,

$$\boldsymbol{\Sigma} = \boldsymbol{\sigma} - i\boldsymbol{\Gamma}, \tag{2.54}$$

where $\boldsymbol{\sigma} = \frac{\boldsymbol{\Sigma}^{\dagger}+\boldsymbol{\Sigma}}{2}$ and $\boldsymbol{\Gamma} = -\frac{\boldsymbol{\Sigma}^{\dagger}-\boldsymbol{\Sigma}}{2i}$. It is important to mention that if the leads are not semi-infinite and the system is closed, then the self-energy is hermitian ($\Sigma^{\dagger} = \Sigma$) and $\boldsymbol{\Gamma} = 0$. For that reason $\Gamma_{R/L}$ are also referred to as the injection rates. As equation 2.53 reveals, the importance of self energies is due to the fact that they are purely determined by the coupling Hamiltonians $\boldsymbol{H}_{SR}$, $\boldsymbol{H}_{SL}$ and the retarded Green's function of the leads. This means that the self-energies are independent of the scattering region and are solely affected by the lead contacts. From the Fisher-Lee equations the transmission amplitude between the scattering channels p and q for when $p \neq q$ is provided by

$$t = i\hbar\sqrt{v_p v_q}\boldsymbol{G}_{OO}^{pq}. \tag{2.55}$$

For $p = q$, the reflection amplitude is

$$r = \left(i\hbar v_p \boldsymbol{G}_{OO}^{pp} - 1\right) e^{-2ik_p}. \tag{2.56}$$

To find the pq^{th} element of the leads Green's function we use equation 2.52 to write

$$\begin{aligned} \boldsymbol{G}_{OO}^{pq} &= \langle p|\, \boldsymbol{G}_{OO}\, |q\rangle \\ &= \langle p|\, \boldsymbol{g}_{O}\, |q\rangle + \boldsymbol{g}_{O}^{p}\, \langle p|\, \boldsymbol{H}_{OS}^{P}\boldsymbol{G}_{SS}\boldsymbol{H}_{OS}^{P}\, |q\rangle\, \boldsymbol{g}_{O}^{q}, \end{aligned} \tag{2.57}$$

where the Green's function of the p^{th} lead is given by

$$\boldsymbol{g}_O = \sum_{p=L,R} |p\rangle \, \boldsymbol{g}_O^p \, \langle p| \, . \tag{2.58}$$

For when $p \neq q$, the first term in the equation 2.57 is zero. Although H_{OS}^P and H_{SO}^P are infinite matrices, the only non-zero elements are coupling elements to the leads. Therefore $\boldsymbol{g}_O^{p/q}$ in the second term only needs to be evaluated at the leads surfaces. We can simplify equation 2.57 to the following,

$$\boldsymbol{G}_{OO}^{pq} = \boldsymbol{g}_O^p \, \langle \boldsymbol{S}_p| \, \boldsymbol{G}_{SS} \, |\boldsymbol{S}_q\rangle \, \boldsymbol{g}_O^q, \tag{2.59}$$

where the dimensionality of vector $S_{p/q}$ is the number of sites (orbitals) in the scattering region. Since $T = |t|^2$, we need to find $|\boldsymbol{G}_{OO}^{pq}|^2$,

$$|\boldsymbol{G}_{OO}^{pq}|^2 = |\boldsymbol{g}_O^p|^2 \, \langle \boldsymbol{S}_p| \, \boldsymbol{G}_{SS} \, |\boldsymbol{S}_q\rangle \, |\boldsymbol{g}_O^q|^2 \, \langle \boldsymbol{S}_q| \, \boldsymbol{G}_{SS}^\dagger \, |\boldsymbol{S}_p\rangle \, . \tag{2.60}$$

Using cyclic invariance under traces we can rearrange equation 2.60 to have,

$$|\boldsymbol{G}_{OO}^{pq}|^2 = Tr \left[|\boldsymbol{S}_p\rangle \, |\boldsymbol{g}_O^p|^2 \, \langle \boldsymbol{S}_p| \, \boldsymbol{G}_{SS} \, |\boldsymbol{S}_q\rangle \, |\boldsymbol{g}_O^q|^2 \, \langle \boldsymbol{S}_q| \right] . \tag{2.61}$$

We define

$$\begin{aligned} |\boldsymbol{S}_p\rangle \, |\boldsymbol{g}_O^p|^2 \, \langle \boldsymbol{S}_p| &= \frac{2\Gamma^p}{\hbar v_p} \\ , |\boldsymbol{S}_q\rangle \, |\boldsymbol{g}_O^q|^2 \, \langle \boldsymbol{S}_q| &= \frac{2\Gamma^q}{\hbar v_q}. \end{aligned} \tag{2.62}$$

Substituting in equation 2.61,

$$|\boldsymbol{G}_{OO}^{pq}|^2 = Tr \left[\Gamma^p \boldsymbol{G}_{SS} \Gamma^q \boldsymbol{G}_{SS}^\dagger \right] . \tag{2.63}$$

The transmission coefficient from lead p to lead q is given by

$$T_{R,L} = |t|^2 = 4Tr \left[\boldsymbol{\Gamma}^p \boldsymbol{G}_{SS} \boldsymbol{\Gamma}^q \boldsymbol{G}_{SS}^\dagger \right] , \tag{2.64}$$

where $\boldsymbol{G}_{SS}$ is given by,

$$\boldsymbol{G}_{SS} = \left(\boldsymbol{g}_S^{-1} - \boldsymbol{\Sigma}\right)^{-1}. \tag{2.65}$$

Since $\boldsymbol{g}_s$ is the Green's function of the non-interacting scattering region, it involves inverting a finite matrix which is numerically possible.

2.8 Thermoelectric properties of materials

Thermoelectric power generation in the presence of a temperature gradient is known as the Seebeck effect and its efficiency is described by the figure of merit, ZT,

$$ZT = \frac{GS^2T}{\kappa_{ph} + \kappa_e}, \tag{2.66}$$

where G is the electrical conductance, S is the Seebeck coefficient and κ_e and κ_{ph} are the electronic and phononic contribution to the thermal conductance.

The numerical method used in this thesis for calculating ZT, is discussed at length in appendix D.

Chapter 3

A festive strategy for suppressing phonons in single molecules: Molecular Christmas trees

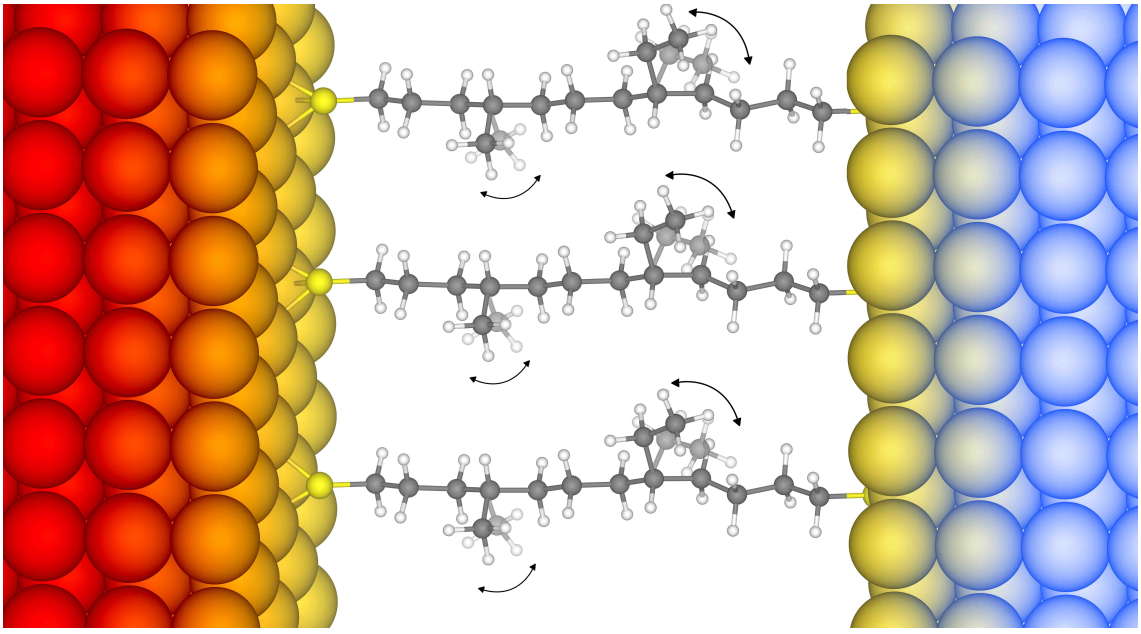

For the purpose of designing self-assembled molecular films with high thermoelectric efficiency, it is desirable to minimise the phonon contribution to their thermal conductance, whilst preserving their electrical properties. Here we highlight a new strategy for minimising the phonon thermal conductance of Christmas-tree-

like molecules composed of a long trunk, along which phonons can propagate, attached to pendant molecular branches. We demonstrate that phonon transport along the trunk is suppressed by Fano resonances associated with internal vibrational modes of the branches and that thermal conductance is suppressed most effectively in molecules with pendant branches of different lengths. As examples, we use density functional theory to demonstrate the reduction in phonon transport in tree-like molecules formed from alkane or acene trunks with various pendant branches. Suppression of thermal conductance arises from a combination of the stiffness of the attachment of the pendant branches to the trunk and the number and frequency of the normal modes of vibration of the branches. The effectiveness of this 'Christmas-tree strategy' for reducing phonon thermal conductance is further enhanced by multiple scattering of phonons from the connections between the branches and the trunk. It can be implemented without significantly affecting electrical properties.

3.1 Introduction

When a thermoelectric material is placed between a heat source and a heat sink with a temperature difference ΔT, the voltage generated between them is given by $\Delta V = -S\Delta T$, where S is the Seebeck coefficient or thermopower. Thermoelectricity in molecular films has attracted increasing interest, following the seminal works,[25,37] in which the Seebeck coefficient S of single molecules was measured for the first time. Later experimental and theoretical studies[33–35,45] reported novel strategies for controlling the sign and magnitude of S.

However these studies provide only part of the fundamental knowledge needed to understand and optimise thermoelectricity on the nanometre scale, because they ignore the crucial role of phonons. Understanding the thermopower S and electrical conductance G of nano-scale materials is not sufficient, because the key

parameter for thermoelectric power generation is the dimensionless thermoelectric figure of merit $ZT = GS^2T/\kappa$, where T is the temperature and the thermal conductance is $\kappa = \kappa_e + \kappa_{ph}$, where κ_e is the electronic contribution to thermal conductance, while κ_{ph} is the contribution from phonons. ZT is a measure of the efficiency of energy conversion from heat to electricity and unless ZT exceeds unity, a material is not competitive. Since phonons play no useful role in the conversion of heat into electricity, strategies for minimizing κ_{ph} are highly desirable. In inorganic materials, nanostructuring has been utilised to reduce κ_{ph}.[69,102–106] Recently some theoretical studies have probed this issue in single molecules.[107–109] These studies introduce single molecules which have low phonon conductance. Herein, we take a significant step forward by introducing a general strategy to design molecules which reduce phonon transport. We show that this method can be applied to any molecule. In what follows, our aim is to develop a new strategy for reducing molecular-scale phonon transport by attaching pendant 'branches' to the backbones or 'trunk' of molecules. Figure 3.1*a* shows an example of a SAM formed from molecules with alkane trunks (oriented vertically), while figure 3.1*b* shows examples of molecules to which various pendant branches are attached to the trunks (in this case the trunks are oriented horizontally). In what follows we demonstrate that these branches can be designed to suppress phonon transport over a range of frequencies, leading to a significant reduction in κ_{ph}.

3.2 Dynamics of model Christmas trees

To illustrate why pendant branches suppress phonon transport, consider an infinite linear harmonic chain of single-degree-of-freedom masses m, connected by nearest neighbour springs of force constant γ, whose dispersion relation is given by the textbook expression $m\omega^2 = 4\gamma sin^2 ka/2$, where a is the spacing between the masses, ω is the phonon frequency and k is their wavenumber. The brown vertical trunks of figure 3.2 are composed of such a chain. For such an ideal crystalline

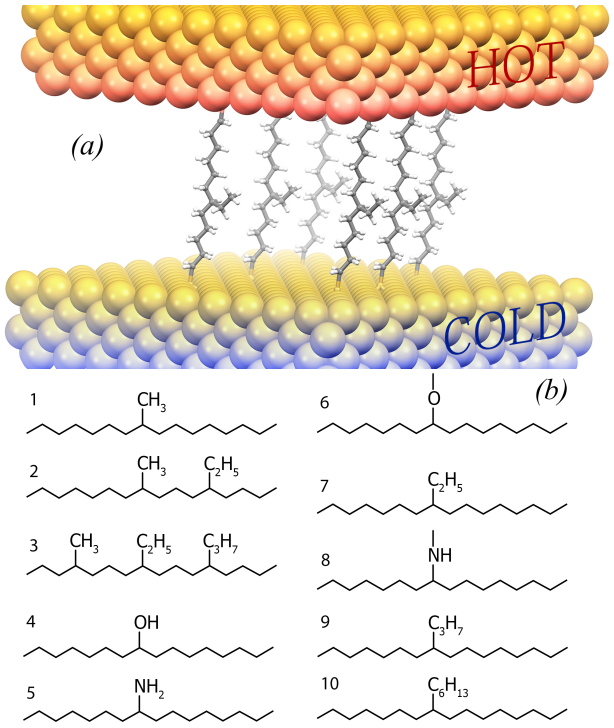

Figure 3.1: (*a*) A SAM connected between hot and cold electrodes. (*b*) Examples of molecules possessing pendant groups (oriented vertically) connected to molecular trunks (oriented horizontally) formed from alkyl chains.

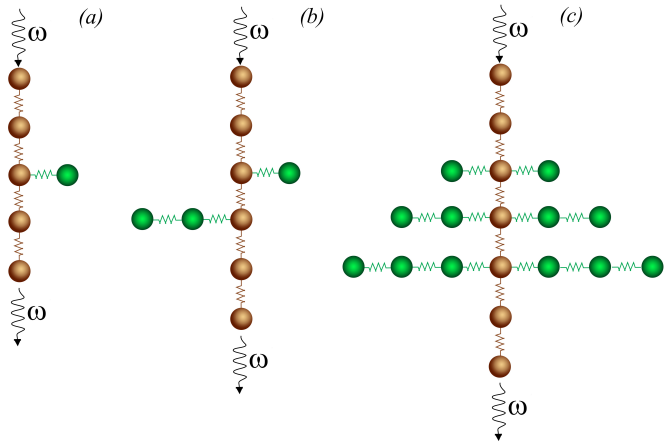

Figure 3.2: Idealised examples of vertical molecular backbones, with pendant side branches. The mass of the brown 'atoms' is m and the mass of the green 'atoms' is M. The brown spring constants are γ and the green spring constants are α.

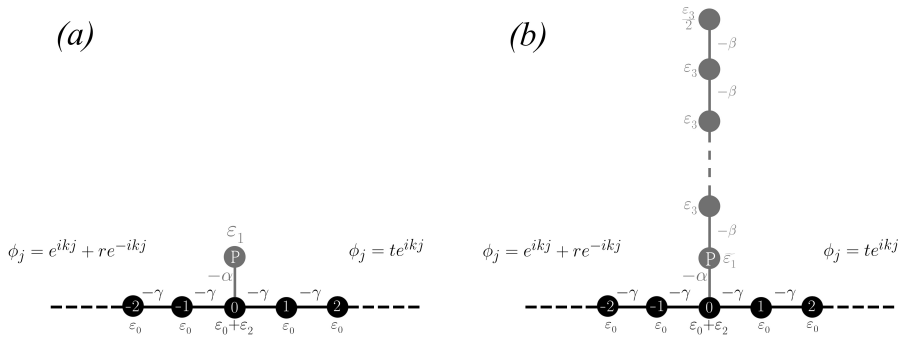

Figure 3.3: (a) Single side branch. (b) Chain side branch with N sites. γ, α and β are the Hessian matrix elements between the illustrated sites.

chain, the transmission coefficient $T(\omega)$ describing phonons of frequency ω entering the chain from the top and exiting from the bottom (ie. travelling from $-\infty$ to $+\infty$) is unity, provided the phonon frequency ω lies between zero and the Debye frequency Ω_D of the chain, where $\Omega_D^2 = 4\gamma/m$. Now consider a pendant mass M attached by a spring of force constant α, to one of the atoms of such a chain, as shown in figure 3.3a. In order to obtain the phonon transmission through such system we solve the dynamical equation. Dynamical equation for a set of masses labeled i connected to their nearest neighbours, is given by:

$$m_i\omega^2\psi_i = (\sum_j \gamma_{ij})\psi_i - \sum_j \gamma_{ij}\psi_j, \tag{3.1}$$

where γ_{ij} is the spring constant between i and j. This equation can be written in terms of the force constant matrix (Hessian matrix) by introducing the amplitudes $\phi_j = m^{1/2}\psi_i$, which satisfy

$$\omega^2\phi_i = \sum_j H_{ij}\phi_i. \tag{3.2}$$

Hence, the force constant matrix is given by:

$$H_{ij} = \begin{cases} \sum_j \frac{\gamma_{ij}}{m_i} \text{ if } i = j \\ -\frac{\gamma_{ij}}{\sqrt{m_i m_j}} \text{ if } i \neq j \end{cases} \tag{3.3}$$

As an example, for the lattice in figure 3.3, $H_{ij} = -\gamma'/m = -\gamma$ for sites i and j on the trunk and $H_{ii} = 2\gamma'/m = 2\gamma = \varepsilon_0$ for all sites on the trunk except for site zero. For the pendant site P, which is coupled to site 0 by a spring of strength α', $H_{PP} = \varepsilon_1 = \alpha'/M$ and the matrix element between the pendant site and site 0 of the trunk is $H_{0P} = -\alpha'/\sqrt{mM} = -\alpha$. Finally for site 0 of the trunk, $H_{00} = \varepsilon_0 + \varepsilon_2$ where, $\varepsilon_2 = \alpha'/m$. Therefore, the sub-block of the infinite Hessian matrix involving sites in the vicinity of P and 0 is of the form:

$$H = \begin{array}{c} \begin{matrix} -2 & -1 & 0 & P & 1 & 2 \end{matrix} \\ \begin{pmatrix} \varepsilon_0 & -\gamma & 0 & 0 & 0 & 0 \\ -\gamma & \varepsilon_0 & -\gamma & 0 & 0 & 0 \\ 0 & -\gamma & \varepsilon_0+\varepsilon_2 & -\alpha & -\gamma & 0 \\ 0 & 0 & -\alpha & \varepsilon & 0 & 0 \\ 0 & 0 & -\gamma & 0 & \varepsilon_0 & -\gamma \\ 0 & 0 & 0 & 0 & -\gamma & \varepsilon_0 \end{pmatrix} \end{array} \begin{matrix} -2 \\ -1 \\ 0 \\ P \\ 1 \\ 2 \end{matrix} \tag{3.4}$$

Using decimation or equivalently the recursive Green's function method,[110] the above problem can be mapped onto an equivalent infinite chain with one impurity (Fig.3.4), where the onsite energy of the scatterer is given by,

$$\varepsilon = \varepsilon_2 + \frac{\alpha^2}{E - \varepsilon_1}. \tag{3.5}$$

For the decimated problem, the dynamical equation takes the form

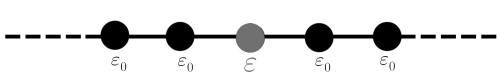

Figure 3.4: The side branch in figure 3.3*a* can be decimated to yield an infinite chain with a single impurity whose onsite energy is ε.

$$(\varepsilon_0 + \varepsilon)\phi_0 - \gamma\phi_1 - \gamma\phi_{-1} = E\phi_0, \tag{3.6}$$

where, the dispersion relation of the infinite chain is $E = \varepsilon_0 - 2\gamma\cos(k)$. For such a lattice, matching the wave amplitude ϕ_j on the left and right of the scatterer yields the following amplitude t of transmitted phonons.

$$t = \frac{1}{1 - \frac{\varepsilon}{2i\gamma\sin(k)}}, \tag{3.7}$$

and consequently,

$$T = |t|^2 = \frac{1}{1 + (\frac{\varepsilon}{2\gamma\sin(k)})^2}. \tag{3.8}$$

Therefore the transmission coefficent is

$$T(\omega) = 1/[1 + x], \tag{3.9}$$

where $x = (\frac{\varepsilon}{2\gamma\sin(k)})^2$. The dispersion relation can be written in the form

$$(\varepsilon_0 - E)^2 - 4\gamma^2 = 4\gamma^2\sin^2(k) \tag{3.10}$$

and therefore,

$$x = \frac{\varepsilon^2}{4\gamma^2 - (\varepsilon_0 - E)^2} = \frac{\varepsilon^2}{E(4\gamma - E)}. \tag{3.11}$$

We can decimate the problem with one side branch to an infinite chain with one scatterer, where the onsite energy of the scatterer is given by ε.

$$\varepsilon = \varepsilon_2 + \frac{\alpha^2}{E - \varepsilon_1} \tag{3.12}$$

From equation 3.12 and equation 3.11 we can conclude,

$$x = \frac{\Omega_m^4\omega^2}{(\Omega_M^2 - \omega^2)^2(\Omega_D^2 - \omega^2)}, \tag{3.13}$$

where $\Omega_m^2 = -\alpha'/m$, the Debye frequency of the chain is given by $\Omega_D^2 = 4\gamma'/m$ and transmitted phonons frequency is ω. To quantify this effect (known as a Fano resonance,[22]) we note that if the brown masses in the trunk of figure 3.2*a* are of

infinite mass, then the green pendant mass would behave as a harmonic oscillator with a single vibrational normal mode of frequency Ω_M given by $\Omega_M^2 = \alpha/M$. For the structure of figure 3.2*a*, when the brown masses are finite, one finds equation 3.13. Now consider the more general problem (Fig. 3.3*b*) with N atoms in the pendant branch β. In what follows β' is the spring constant between two sites in the pendant branch, M is the mass of sites on the pendant branch and α' is the spring constant connecting atom 0 of the trunk to atom P of the side branch for which the Hessian matrix element $H_{0P} = -\alpha'/\sqrt{mM} = -\alpha$. When $H_{0P} = 0$, the dynamical matrix H is block diagonal, with an infinite block h_{AA} describing couplings involving sites belonging to the trunk only and a finite block h_{BB} describing coupling between sites belonging to the branch only. For a pendant branch comprising a simple linear chain h_{BB} is an $N \times N$ matrix of the form

$$h_{BB} = \begin{pmatrix} \varepsilon_1 & -\beta & & & \\ -\beta & \varepsilon_3 & -\beta & & \\ & -\beta & \varepsilon_3 & -\beta & \\ & & & \ddots & \\ & & & & \varepsilon_3/_2 \end{pmatrix}, \tag{3.14}$$

where, similar to the previous description of the Hessian matrix (Eq. 3.3), $\beta = -\beta'/M$ and $\varepsilon_3 = 2\beta'/M$. More generally, h_{BB} is a matrix of dimensions equal to the number of normal modes of the branch. The Green's function associated with the branch is given by

$$g_B = (E - h_{BB})^{-1}. \tag{3.15}$$

Similarly the Green's function associated with the trunk is

$$g_A = (E - h_{AA})^{-1}, \tag{3.16}$$

where, h is an $N \times N$ matrix , The only present connection between the side branch and the infinite chain is $-\alpha$. Therefore, according to Dyson's equation,

when H_{0P} is non-zero, the Green's function sub-matrix G_{AA} involving sites l and m belonging to the trunk is

$$(G_{AA})_{lm} = (g_A)_{lm} + (g_A)_{lp}(h_{AB})_{qp}(G_{BB})_{qr}(h_{BA})_{rs}(g_A)_{sB}, \tag{3.17}$$

where

$$\begin{aligned}(G_{BB})_{PP} &= (g_B^{-1} - \Sigma)^{-1} \\ &= [(g_B)_{PP}^{-1} - \alpha^2(g_A)_{00}]^{-1}\end{aligned} . \tag{3.18}$$

More generally for the branch of N degrees of freedom in the lattice of figure 3.3*b*, we define

$$\varepsilon_1 = E - \frac{1}{(g_B)_{PP}} \tag{3.19}$$

which is simply the energy-dependent site energy that would arise if all sites of the branch except site 1 were decimated. This means that if the site energy ε_1 in the lattice of figure 3.3*a* is replaced by ε_1 of equation 3.19, then the resulting scattering properties are identical to those of the lattice of figure 3.3*a*. From equation 3.19 and 3.5 is replaced by

$$\varepsilon = \frac{\alpha'}{m}[1 + \frac{\alpha'(g_B)_{PP}}{M}] = \Omega_m^2[1 + \Omega_M^2(g_B)_{PP}], \tag{3.20}$$

where, $\Omega_m^2 = \frac{\alpha'}{m}$ and $\Omega_M^2 = \frac{\alpha'}{\rho}$.
Consequently x is replaced by

$$\varepsilon = \Omega_m^2[1 + \Omega^2 g_{11}]. \tag{3.21}$$

$$x = \frac{\Omega_m^2}{\omega^2(\Omega_D^2 - \omega^2)}\left[1 + \Omega_M^2(g_B)_{PP}\right] \tag{3.22}$$

Since $(g_B)_{PP}$ diverges when ω coincides with a normal mode frequency of the pendant chain, x also diverges and phonon transmission vanishes.

It is interesting to note that at zero frequency, this expression yields $x = 0$ and

the transmission coefficient equals unity, as it must by translational invariance. To demonstrate this feature, we note that the relationship between the Greens function $(g_B)_{PP}$ of the chain attached to a wall and the Greens function g_0 of the chain in free space (ie when $\varepsilon_1 = 0$), is

$$(g_B)_{PP} = (g_0^{-1} - \varepsilon_2)^{-1} = \frac{g_0}{1 - g_0\Omega_M^2}, \tag{3.23}$$

Hence,

$$x = \frac{\Omega_m^2}{\omega^2(\Omega_D^2 - \omega^2)[1 - g_0\Omega_M^2]} \tag{3.24}$$

Since g_0 diverges and x vanishes when ω coincides with a normal mode frequency of the pendant chain in free space and since one of these modes is a zero frequency translationally-invariant mode, the zero-frequency transmission coefficient is equal to unity.

Therefore, at lower frequencies g_0 becomes infinite and $x = 0$. On the other hand, if $\omega^2 = \Omega_M^2$, g diverges, therefore $x = \infty$ and consequently the transmission coefficient (Eq. 3.9) is suppressed. Unsurprisingly, the presence of the pendant mass reduces the value of $T(\omega)$ below the ideal value of unity. However perhaps more surprisingly, at a certain frequency Ω, the presence of the pendant group causes x to diverge and $T(\omega)$ to vanish. This suppression of transmission along a chain, which occurs when the frequency ω of a phonon travelling along the trunk resonates with a normal mode Ω_M of a pendant branch, is a generic feature, which we aim to exploit in the design of molecules with low phonon thermal conductance. Figure 3.2*b* shows an example of a vertical trunk (coloured brown) with two pendant branches (coloured green) of different lengths, which would cause $T(\omega)$ to vanish at their respective normal mode frequencies.

To minimise the phonon thermal conductance κ_{ph}, it will be necessary to eliminate phonon transmission along a molecular trunk at all frequencies between zero and

k_BT and for this purpose, it is desirable to attach multiple pendant groups with a variety of different normal mode frequencies to the trunk. Figure 3.2c shows an example of a 'Christmas tree' type structure with pendant branches of increasing lengths connected to a vertical molecular trunk. In this model, as the number of branches increases along the trunk, the number of sites per branch is increased by one (therefore, in a system with 6 side branches the maximum length is 3 sites). In this case the variety of normal-mode frequencies associated with different-length branches suppresses phonon transmission over a wide range of frequencies. This Christmas tree strategy is illustrated in figure 3.5, which shows the transmission coefficient $T(\omega)$ for structures with 3.2a, 3.2b and 3.2c containing side branches of one, three and ten different lengths respectively and demonstrates that the number of zeros in $T(\omega)$ increases with the number of side branches. Figure 3.5d shows the

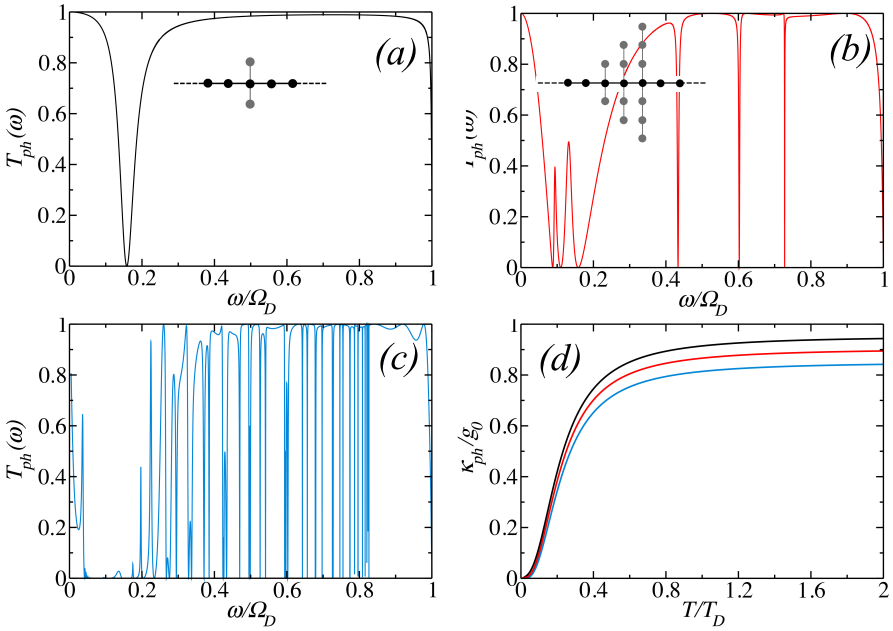

Figure 3.5: For model Christmas trees formed from single-degree-of-freedom masses, such those shown in figure 3.2, (a), (b) and (c) show the transmission coefficient for N=1, 3 and 10 side branches respectively. In each case, the lengths of the branches increase sequentially from 1 to N. (d) The phonon thermal conductances of structures 3.5a (black), 3.5b (red) and 3.5c (blue) obtained by combining the transmission coefficients $3(a-c)$ with equation 3.27. Results are shown on the scale of Debye temperature $T_D = \hbar\Omega_D/K_B$.

effect of these zeros on the phonon thermal conductance $\kappa_{ph}(T)$ at temperature T,

obtained by evaluating the formula

$$\kappa_{ph}(T) = \frac{1}{2\pi}\int_0^\infty \hbar\omega T_{ph}(\omega)\frac{\partial f_{BE}(\omega,T)}{\partial T}d\omega, \tag{3.25}$$

where, $f_{BE}(\omega,T) = (e^{\hbar\omega/k_BT}-1)^{-1}$ is the Bose-Einstein distribution function and $T_{ph}(\omega)$ is the transmission coefficient for phonons of energy $\hbar\omega$[22] travelling along a backbone. Since

$$\frac{\partial f_{BE}(\omega,T)}{\partial T} = \frac{\hbar\omega}{k_BT^2}\frac{e^{\hbar\omega/k_BT}}{(e^{\hbar\omega/k_BT}-1)^2}, \tag{3.26}$$

$$\kappa_{ph}(T) = \frac{k_B}{2\pi}\int_0^\infty T_{ph}(\omega)\frac{\hbar\omega}{k_BT}\frac{e^{\hbar\omega/k_BT}}{(e^{\hbar\omega/k_BT}-1)^2}d\omega. \tag{3.27}$$

In this expression, the quantum of thermal conductance is $g_0 = \frac{(\frac{\pi}{6})(k_B)^2}{\hbar}T = 9.456\times10^{-13}(\frac{W}{K^2})T$. As an example, at room temperature, the quantum of thermal conductance g_0 is $284pW/K$, which is the maximum room-temperature phonon thermal conductance per channel and occurs only if the upper cut off of the phonon channel is greater than approximately $5k_BT$. Figure 3.5d shows the thermal conductance versus temperature for each of the structures in figures 3.5$a-c$ and demonstrates that thermal conductance is suppressed by the presence of pendant branches. To suppress phonon transmission further, one possible strategy is to increase the width of the Fano resonances by increasing the strength of the coupling α between the side branches and the trunk. For a system with 5 side branches, figures 3.6$a-c$ shows $T_{ph}(\omega)$ when $\alpha = 0.2, 0.4$ and 0.7 respectively and demonstrate that the width of Fano resonances increases with increasing α. Figure 3.6d shows that this leads to a corresponding suppression of the thermal conductance.

It is worth mentioning that when a trunk is attached to more than one branch, as in figures 3.2b and 3.2c, then in addition to suppression due to Fano resonances, phonons also undergo multiple scattering from the points of attachment of the branches to the trunk. To distinguish between these two effects and to highlight the importance of Fano resonances, figure 3.7a shows the transmission coefficient (black curve) of the six-branch Christmas tree shown on the same panel. For com-

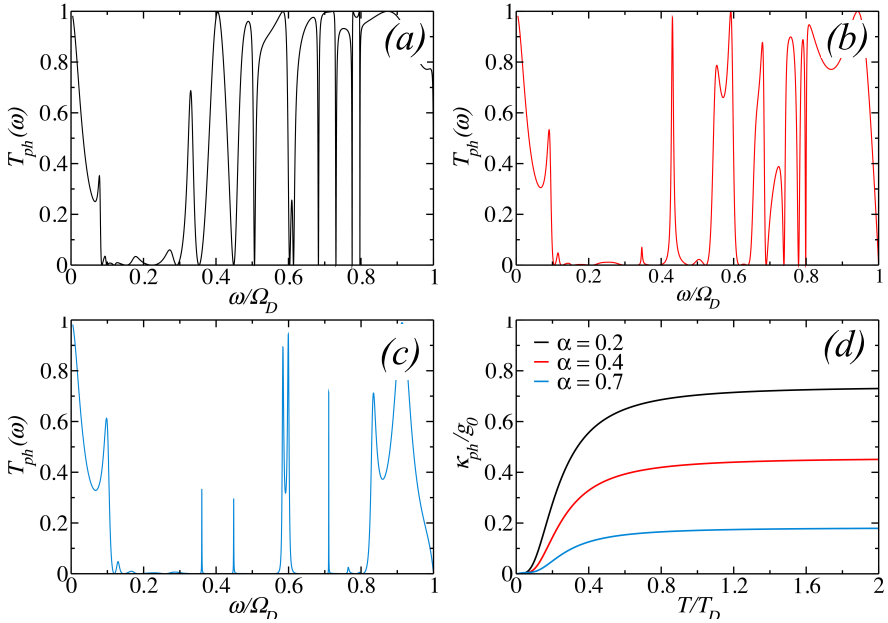

Figure 3.6: $(a-c)$ Transmission coefficients of a Christmas-tree with 10 side branches, when $\alpha = 0.2, 0.4$ and 0.7. (d) The corresponding thermal conductances versus temperature.

parison, the red curve of figure 3.7a shows the transmission coefficient obtained when the masses of the branches are set to infinity, so that their normal mode frequencies are also at infinity, therefore Fano resonances are absent and only multiple scattering from the attachment point remains. Clearly the latter contributes to a reduction in phonon transmission. Figure 3.7b shows the corresponding thermal conductances and demonstrates that the lowest thermal conductance (black curve) is obtained when both Fano resonances and multiple scattering are present.

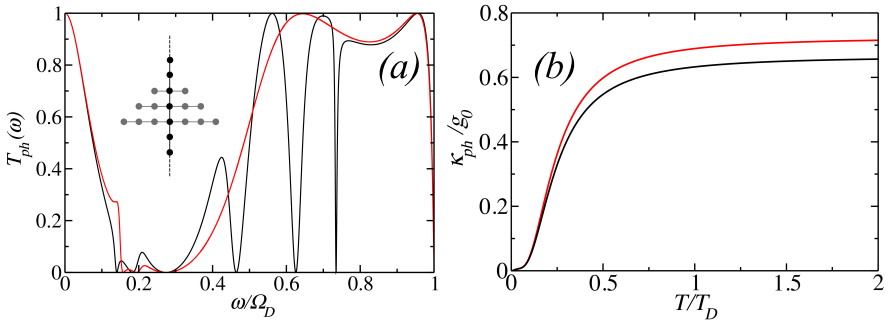

Figure 3.7: Red and black cures curve shows the $T_{ph}(\omega)$ (on the left) and κ_{ph} (on the right) for chain attached to wall and chain with three side branches respectively.

Molecular Christmas trees formed from branches of different lengths are typically asymmetric and therefore it is of interest to ask if asymmetry is important. As shown in figure 3.8, symmetry can be restored by adding further branches. However, such additions barely change the thermal conductance; therefore we conclude that presence of asymmetry or otherwise is not central to the Christmas tree strategy.

Although many of the molecules studied above are asymmetric, such asymmetry is not crucial. Figure 3.8*a* compares the transmission probability and phonon thermal conductance of a model asymmetric molecule with branches of 1, 2, 3 masses (black curves) with that of a symmetric molecule formed by adding further branches of 3, 2 and 1 masses (red curves). In the symmetric scatterer, repetition of branches does not introduce more Fano resonances and therefore the thermal conductance of the symmetric molecule is close to that of the asymmetric molecule.

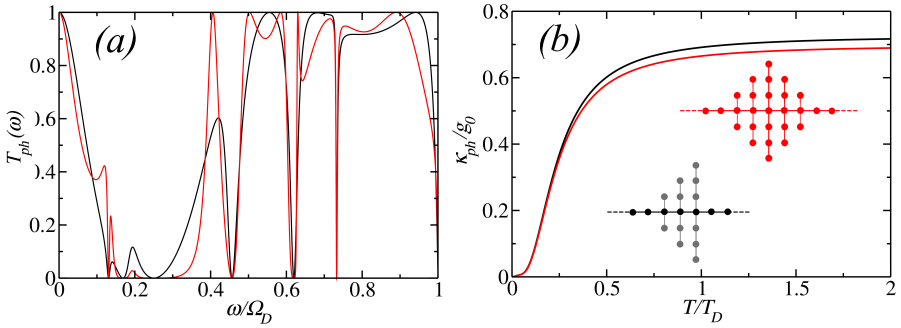

Figure 3.8: (a) Transmision coefficient comparison for illustrated models. (b) The phonon conductance. This demonstrates that the presence of branches of different lengths is desirable.

3.3 Dynamics of molecular Christmas trees

So far we have considered only an ideal model of vibrations, using artificial single-degree-of-freedom masses. To examine whether or not the 'Christmas-tree' phonon-reduction strategy applies to more complicated molecules, we now use density-functional theory (DFT) to analyse phonon transmission along the alkane chains

shown in figure 3.1*b*, containing various pendant branches using the method of reference,[74] in which the dynamical matrix is constructed from the forces calculated using DFT[88] and the Gollum transport code[101] is used to calculate the phonon transmission coefficient.

Figure 3.9 shows the transmission coefficients and thermal conductances of molecules 1, 2 and 3 of figure 3.1*b*, with side branches of CH_3 for molecule 1, CH_3 and C_2H_5 for molecule 2 and CH_3, C_2H_5 and C_3H_7 for molecule 3. This demonstrates that the Christmas tree strategy successfully suppresses phonon transport in a realistic molecule. To allow us to focus on phonon scattering due to pendant branches only,

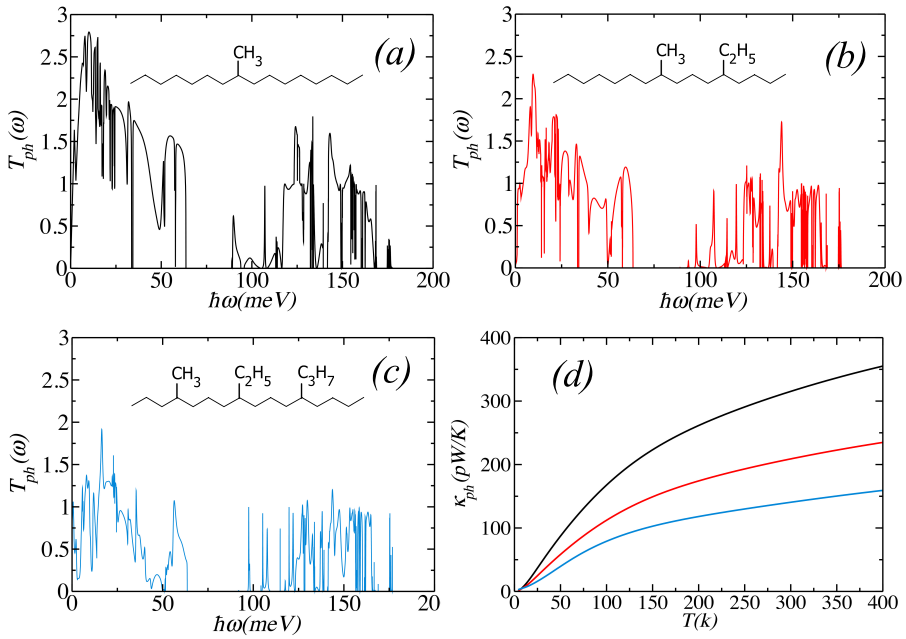

Figure 3.9: DFT results for the transmission coefficients and thermal conductances of molecules 1 (black), 2 (red) and 3 (blue) of figure 3.1*b*, where the trunks are formed from infinitely-long alkyl chains.

the side branches in the molecules of figure 3.9 are attached to an infinitely-long alkane trunk, which also acts as a waveguide for phonons entering and leaving the scattering region. This idealisation avoids interface scattering at electrode molecule interfaces that would be present in a real device and would further reduce phonon transport. In the absence of pendant branches, the transmission coefficient is simply equal to the number of open scattering channels, which is plotted as a function of frequency in figure 3.10 and vanishes in the approximate

frequency ranges $63-87meV$. Since the number of open channels is also an upper bound to $T_{ph}(\omega)$, this leads to gaps in $T_{ph}(\omega)$ over these frequency ranges, which are visible in figures 3.9 $a-c$.

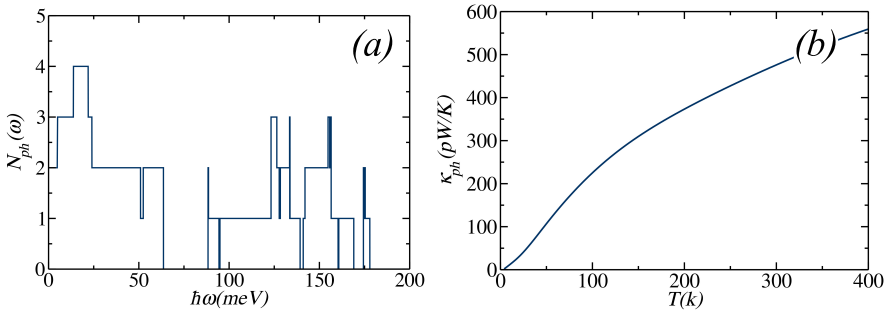

Figure 3.10: (a) Number of open phonon channels in an infinite alkyl chain versus frequency. (b) Phonon conductance for a perfect infinite alkane chain.

For an isolated molecule, the weight of a normal mode of vibration on the side branches can be characterised using the participation ratio PR defined by

$$PR = \sum_{i}^{3N} |\psi_i|^2 \tag{3.28}$$

where the sum is over all degrees of freedom belonging to the side branches and is the amplitude of an eigenstate on the degree of freedom of a branch. To show that the Fano resonances are associated with the side branches, we compare the PR of all degrees of freedom of atoms in side branches of molecule 3 in figure 3.1b in a frequency range of $80mev$ to $110mev$. As figure 3.11 illustrates, a high value of PR corresponds to a nearby Fano resonance in transmission function and in the regions that the PR of side branches is low, the transmission is high. This is found to be a generic feature of all molecules studied here.

Figure 3.12 shows the total participation ratio of side branches, as well as the participation of each side branch. The animation of the named vibrational modes are provided in the supplementry information of reference.[111]

The difference between connecting a phonon guide to a heavy stationary mass,

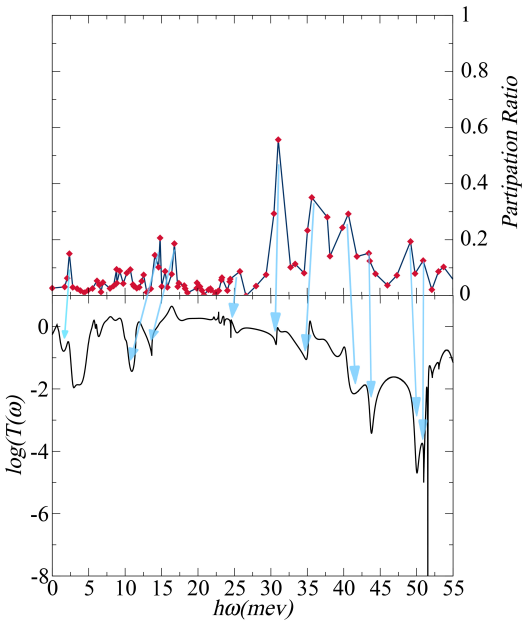

Figure 3.11: Comparison between the participation ratio (upper panel) and the transmission coefficient (lower panel).

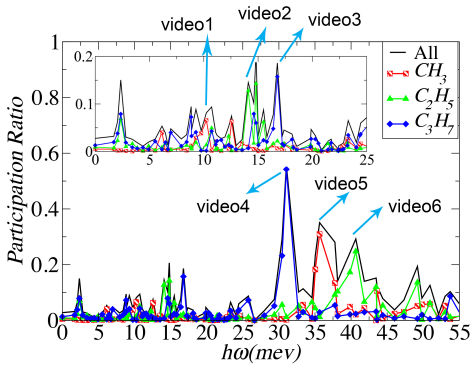

Figure 3.12: Participation ratio of CH_3 side branch(red), C_2H_5 side branch (green) and C_3H_7 (blue). The sum of participation ratio of all side branches(black).

heavy moving branch with no internal degrees of freedom, and a side branch with internal degrees of freedom are discussed in this section. In the first case, phonon waves reflect from the point of contact. In the second case, we allow this heavy object to move. Therefore, the object has modes of vibration in lower frequencies according to the movements of the entire object. In the third system, we have a side branch with internal degrees of freedom, for example a C_2H_5 branch attached to an alkane chain. This side branch has degrees of freedom related to the movements of the entire branch in lower frequencies as well as the internal modes of vibration in higher frequencies. This concept is shown in figure 3.13, where

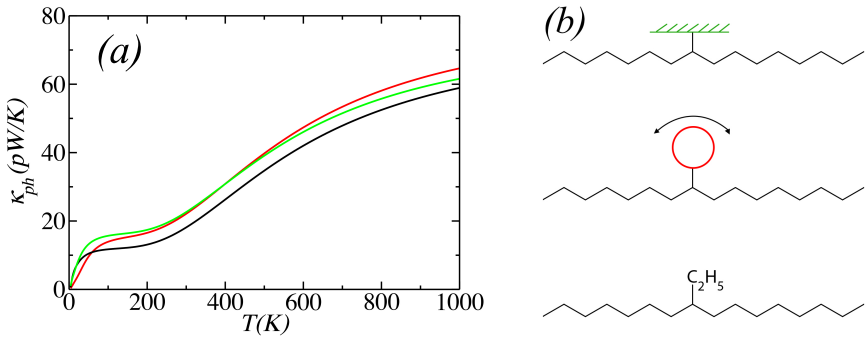

Figure 3.13: Black shows the Alkane with C_2H_5 branch, red is alkane with heavy side branch(no internal degrees of freedom) and green is an alkane branch attached to a wall.

the phonon conductances of the systems discussed (shown on the right hand side) are shown. As explained earlier, a system with a heavy moving mass(red) has a lower conductance in lower frequencies due to the appearance of Fano resonances in lower frequencies (centre of mass movements). However, a system with a C_2H_5 side branch, although it has a lighter mass, has the overall lower phonon conductance due to the appearance of many Fano resonances associated with the modes of vibration of the side branch.

As discussed earlier, stronger coupling to the main branch can further suppress phonon transmission along the trunk. In real molecules, this can be achieved by changing the type of atom connecting the side branch to the trunk, which will change the length and the stiffness of the bond connecting the branch to the trunk. To show this we first compare the transmission coefficients of molecule 1, 4 and 5 (CH_3, OH and NH_2) of figure 3.1b. Each of these molecules contain a single side branch, but with terminal branch atoms C, N and O connected to the trunk. Our DFT calculations shows that the minimum-energy bond lengths of terminal branch atoms C, N, and O connected to the alkyl trunk are 1.51, 1.44 and 1.41 $\mathring{A}$ respectively. The transmission coefficient for the named 3 molecules are shown in figure 3.15$a-c$. As expected, figure 3.14d shows that phonon thermal conductance is smaller in the presence of the shorter bond lengths between the $N-$ and $O-$ terminated side branches and the trunk. Similarly thermal conductance is higher

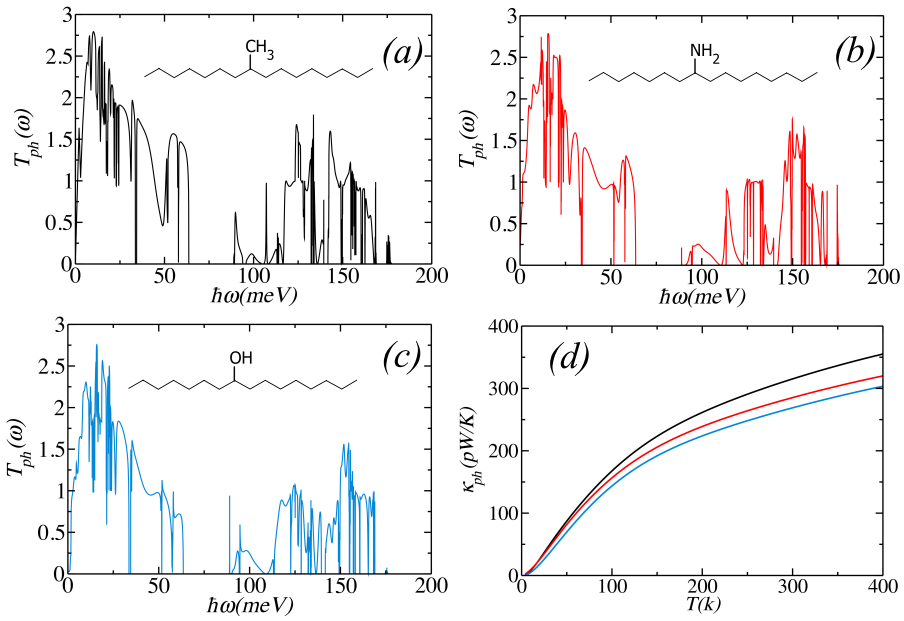

Figure 3.14: Figures (a), (b), (c) show the phonon transport through molecules 1, 4 and 5 of figure 3.1 b respectively. Figure (d)compares the phonon conductance in molecules a, b and c.

in the presence of the longer bond length between the $C-$terminated branch and the trunk.

To show that this effect is purely due to the strength of coupling and is not affected by the length of the side branch, we repeat the same calculation for molecules 6, 7 and 8 of figure 3.1b. The side branches on these three molecules (C_2H_5, OCH_3 and NCH_3) are longer than molecules 4 and 5. Therefore, the number of vibrational modes of the side branches of these molecules are more. Consequently, these molecules have lower phonon conductance in comparison with molecules 4 and 5. Since the overal conductance is lower, the effect of the coupling strength is subtle. Similar to molecules 1, 4 and 5, for the molecules 6, 7 and 8 the more strongly coupled side branch (OCH_3) has the lowest phonon conductance. (Fig. 3.14d)

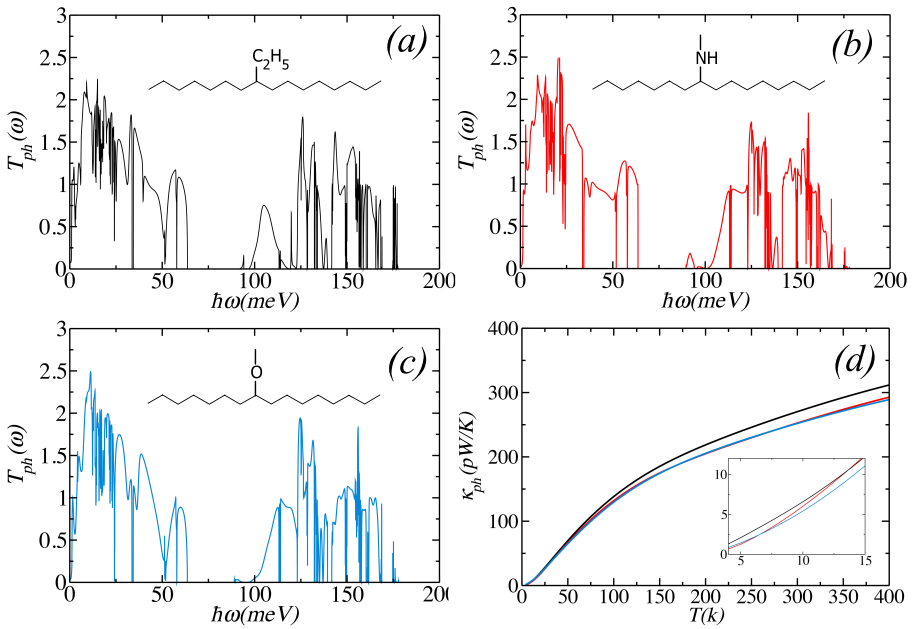

Figure 3.15: Phonon transmission through alkane trunks with (a) C_2H_5, (b) NCH_4 and (c) OCH_3 side branches Figure (d) shows the phonon thermal conductances of alkyl trunks with OCH_3 (blue), C_2H_5 (black) m,kand NCH_4 (red) branches.

3.4 Shape vs number of branches

A subtle question is whether or not it is more favourable to incorporate a larger number of small though different side branches or a smaller number of more complex branches. In order to understand the best choice of side branches, we have compared a system with two side branches, CH_3 and C_2H_5 and a system with one single side branch with equivalent mass and number of atoms (C_3H_7). Figure 3.16 shows that CH_3 and C_2H_5 have 8 modes of vibration in the frequency range of 0 to 55, when attached to a rigid wall. However C_3H_7 has only 6 modes in the same frequency range. This is due to the fact that each side branch has a number of lower frequency modes which are controlled by the side branch weak coupling to the trunk. Although C_3H_7 has the same number of atoms and more modes of vibration they appear at higher frequencies, since they are controlled by intra molecule coupling which are stronger bonds. Due to the appearance of more modes of vibration and consequently more Fano-resonances in the transmission function, phonon conductance of the system with two side branches (CH_3 and C_2H_5) is

significantly lower than the system with a single long branch (C_3H_7). Therefore, we conclude that a larger number of simple branches is more favourable than a single but more-complicated side branch.

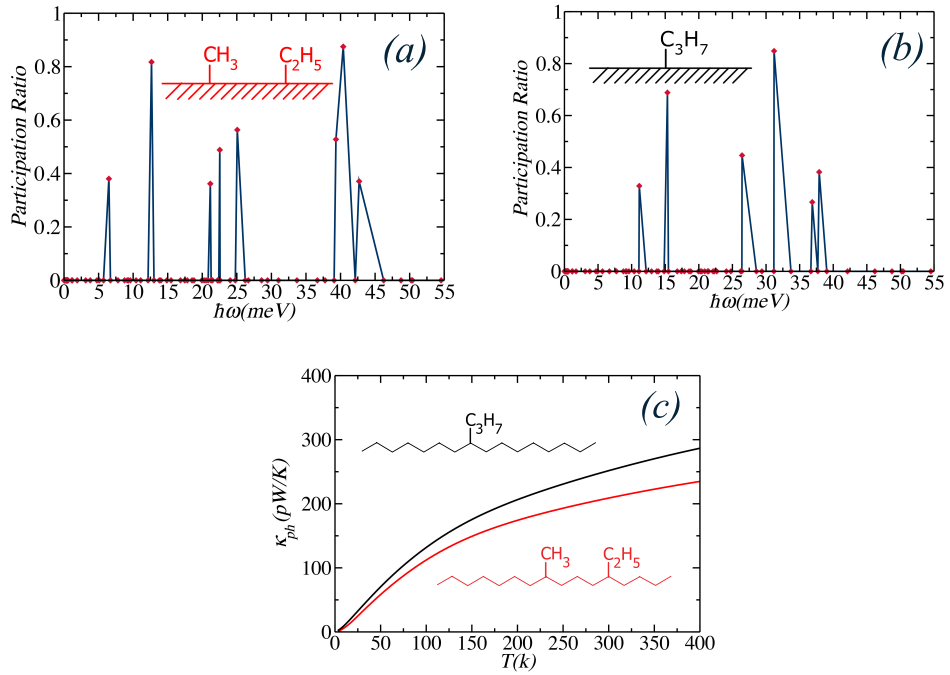

Figure 3.16: (a) Participation ratio of two side branches CH_3 and C_2H_5 when attached to a rigid wall and (b) for C_3H_7. (c) Comparison of the phonon conductances of the illustrated system.

The participation ratios of each branch typically show peaks at different frequencies. The total participation ratio is the sum of the participation ratios of each branch. This means that having a greater number of side branches creates more Fano resonances in the transmission function in the energy range of interest.

As demonstrated in figure 3.16, at least for alkane branches the former is the more effective. For example a structure with one methyl and one ethyl side branch has a lower thermal conductance than a structure with a single propyl side branch. Similarly a structure with single methyl, ethyl and propyl side branches has a lower thermal conductance than a structure with a single hexyl branch. This occurs because each side branch contributes a number of low frequency modes controlled by the relatively-weak coupling between the branches and the backbone

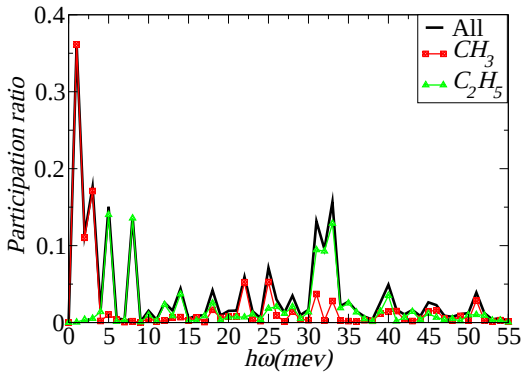

Figure 3.17: Participation ratio of all side branches in molecule 2 in figure 3.1*b* (Black) participation ratio of C_2H_5 side branch (Green) and participation ratio of CH_3 (Red).

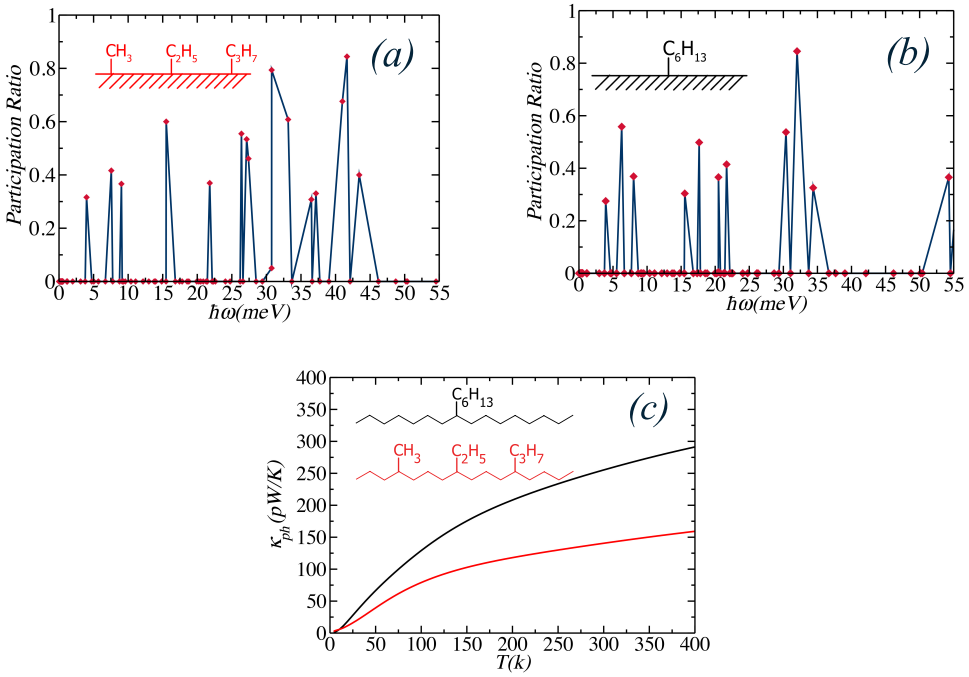

Figure 3.18: (*a*) Participation ratio of three side branches CH_3, C_2H_5 and C_3H_7 when attached to a rigid wall and (*b*) for C_6H_{13}. (*c*) Comparison of the phonon conductances of the illustrated system.

and therefore the number of such modes increases with the number of branches. In contrast, although a longer branch has more low frequency modes than a short branch, these are controlled by the intra-molecular couplings, which are generally stronger than intermolecular couplings. Consequently, many shorter branches of different lengths with a collective total of N alkyl units, lead to more low-frequency modes than a single large branch, with the same number of N alkyl units.

3.5 Heavier side branches

Clearly thermal conductance below a temperature T can only be affected by Fano resonances of frequency ω lower than $k_BT/\hbar$ and therefore to reduce the low-temperature thermal conductance high-mass pendant branches with low-frequency normal modes of vibration are of interest. To illustrate this feature, figure 3.19 compares the phonon transmission and thermal conductance of molecule 3 of figure 3.1*b*, with the same molecule where all carbons on side branches are replaced by ^{13}C.

Figure 3.19 *c* clearly demonstrate that heavier side branches move the Fano-resonances to lower frequencies and suppress the phonon conductance further, in the temperature range of desire.

3.6 Christmas-tree strategy for an acene trunk

To demonstrate that the Christmas-tree strategy is generic and applies to different molecular trunks, we have also examined phonon transport along molecules with an acene trunk, which is more rigid than an alkane chain. As expected, phonon transmission is suppressed by the presence of pendant branches. A systematic study is conducted on an infinite acene chain, with the side branches illustrated in figure 3.20.

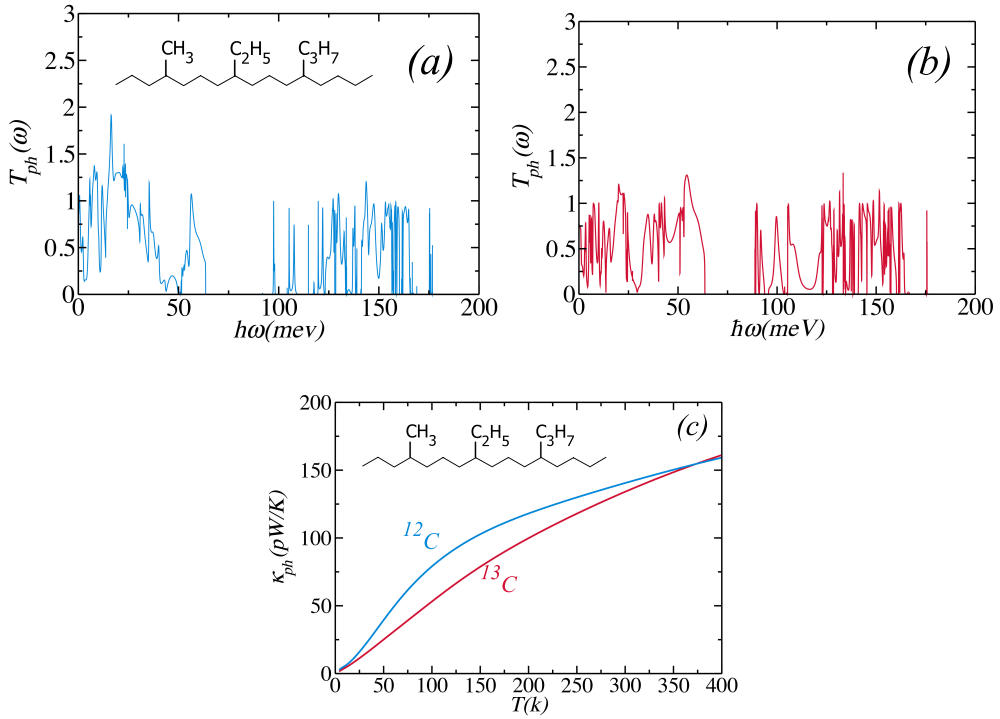

Figure 3.19: Phonon transmission through molecule 3 in figure 3.1*b* (b) Phonon transmission for molecule 3 where all the carbons in the side braches are replaced by ^{13}C. (c) Comparison between the phonon thermal conductance of both systems.

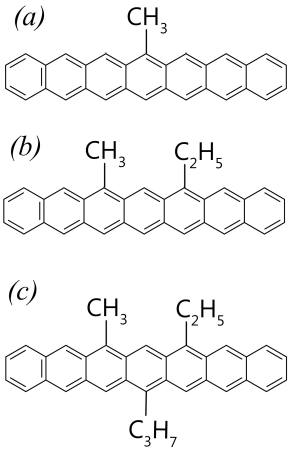

Figure 3.20: Examples of acene branch with various side branches.

Phonon transmission for molecules a, b and c in figure 3.20 are shown in figure 3.21$(a-c)$. Comparing the phonon conductances of these three molecules in figure 3.21d shows that the phonon conductance is suppressed by increasing the number of side branches. The phononic open channels of an infinite acene chain are shown in figure 3.22.

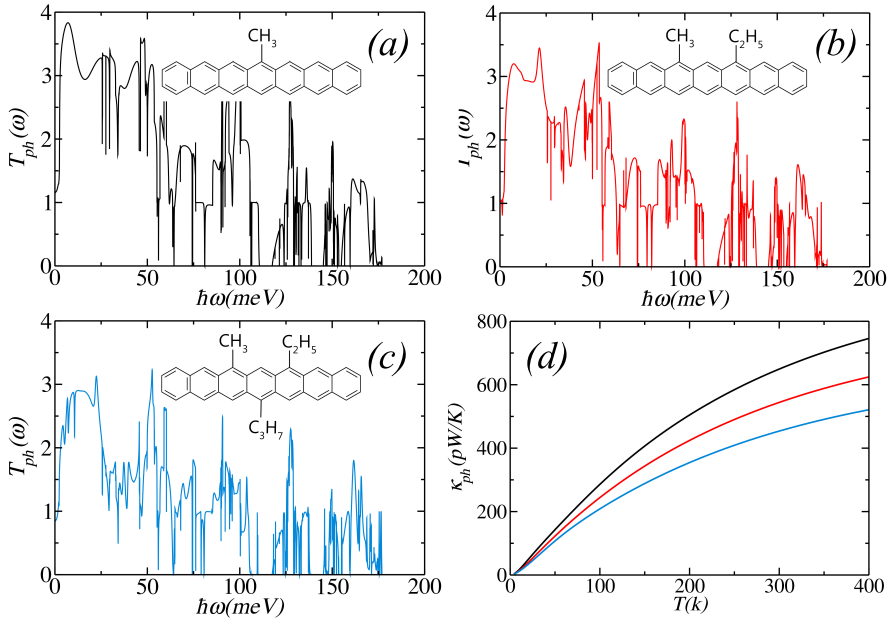

Figure 3.21: $(a-c)$ Transmission coefficient for phonons through molecules $a-c$ in figure 3.20. (d) Phonon conductance for molecule $a-c$ respectively.

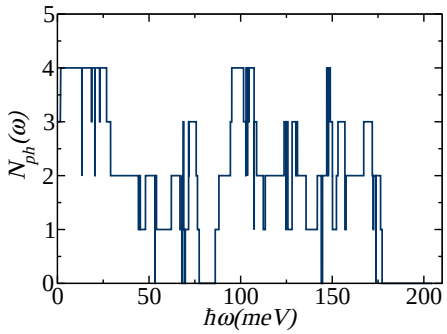

Figure 3.22: The number of open channels in an infinite acene chain.

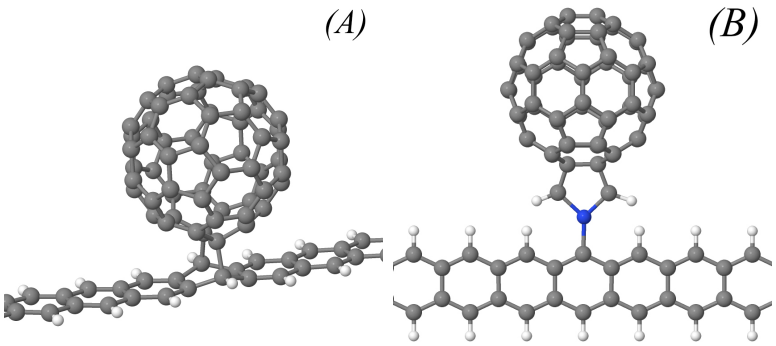

Figure 3.23: The relaxed geometry of two systems with acene trunk and $C60$ side branch where $C60$ is attached to the trunk via different connections.

To show that the strength of the coupling between the side branch and the trunk can be utilised to tune the phonon transmission and thermal conductance for an acene trunk as well, we consider two separate systems shown in figure 3.23. In system A two single $C-C$ bonds are formed on either side of the acene and $C60$. In system B, $C60$ is attached to acene using a pyrrole. Figure 3.24a and b shows the phonon transmission through the above systems over a frequency range of 0 to 30 meV and figure 3.24 shows the resulting thermal conductances. As expected,

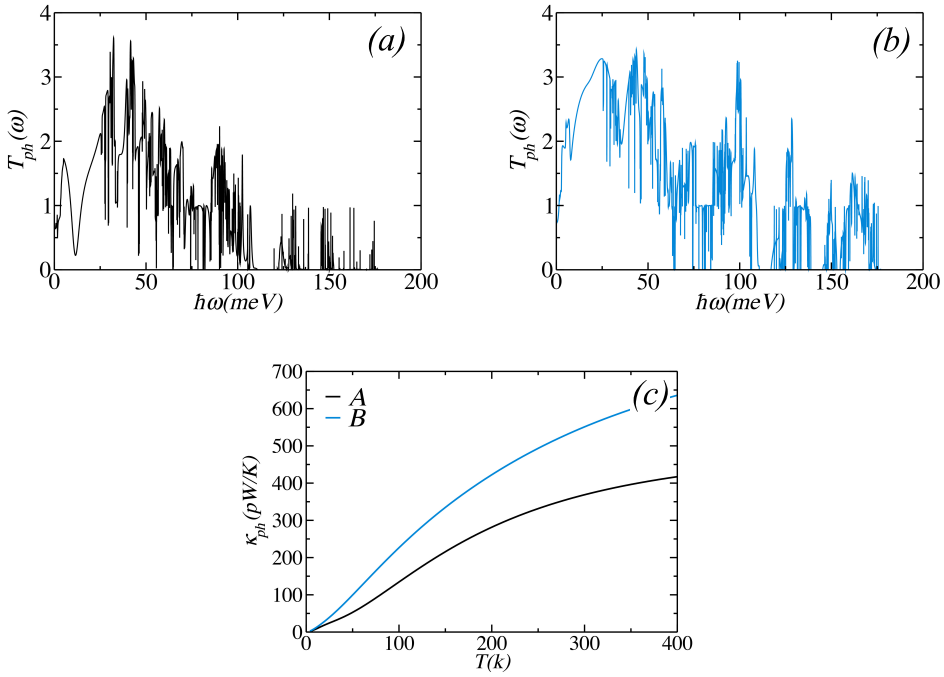

Figure 3.24: Comparison between the phonon conductances for the structures A and B. (c) Comparison between the phonon conductances for the structures A and B.

structure A, in which the pendant $C60$ is attached to the trunk via two covalent bonds has a lower conductance in comparison with system B since nitrogen forms a weaker bond with the trunk.

Figure 3.9d clearly demonstrates that the suppression of thermal conductance increases with the number of branches. It is interesting to note that in contrast with studies of energy transfer in conjugated dendrimers, the reflection of phonons due to Fano resonances is energy conserving and involves no energy transfer into the branches.

3.7 Gold lead

Finally, to demonstrate that molecular Christmas tree strategy is effective in the presence of metallic electrodes, figure 3.25 shows the phonon conductance of molecules 2 and 7 when attached to gold leads by $S-Me$ anchor groups. This shows that increasing the number of pendant branches from one to two causes a 18% decrease in phonon conductance and demonstrates that the Christmas tree strategy remains effective.

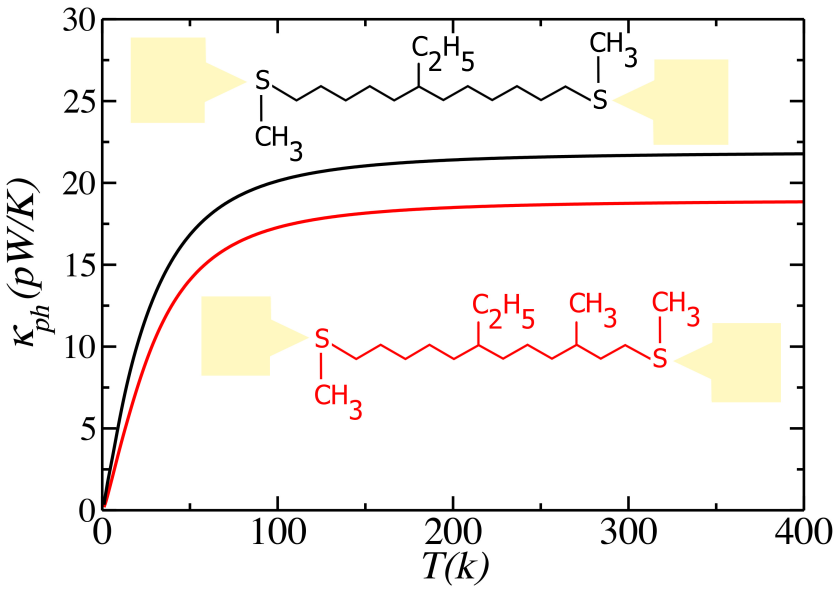

Figure 3.25: Phonon conductance through molecule 2 and 7 when placed between two gold leads.

3.8 Conclusion

We have demonstrated that when pendant branches are attached to a long molecular trunk, phonon transport along the trunk is suppressed by Fano resonances associated with internal vibrational modes of the branches. We first presented the principles of this strategy using a simple idealised model of vibrations and then used density functional theory to demonstrate its efficacy in real molecules with

trunks made from alkyl chains. In both cases, thermal conductance suppression arises from a combination of the stiffness of the attachment of the pendant branch to the trunk and the number and frequency of the normal modes of vibration of the branches. This 'Christmas-tree strategy' for reducing phonon thermal conductance is further enhanced by multiple scattering of phonons from the connections between the branches and the trunk. For the purpose of increasing the thermoelectric efficiency of molecular films, this strategy for the molecular engineering of phonons is attractive because electrically-inert pendant groups are often attached to molecular trunks to increase their solubility in common solvents. Such group barely affect electrical properties, but as demonstrated above can have a marked effect on thermal properties. Therefore the Christmas tree strategy allows us to engineer the denominator of ZT, without affecting the numerator.

Chapter 4

Thermoelectric properties of thiophene and EDOT molecular wires

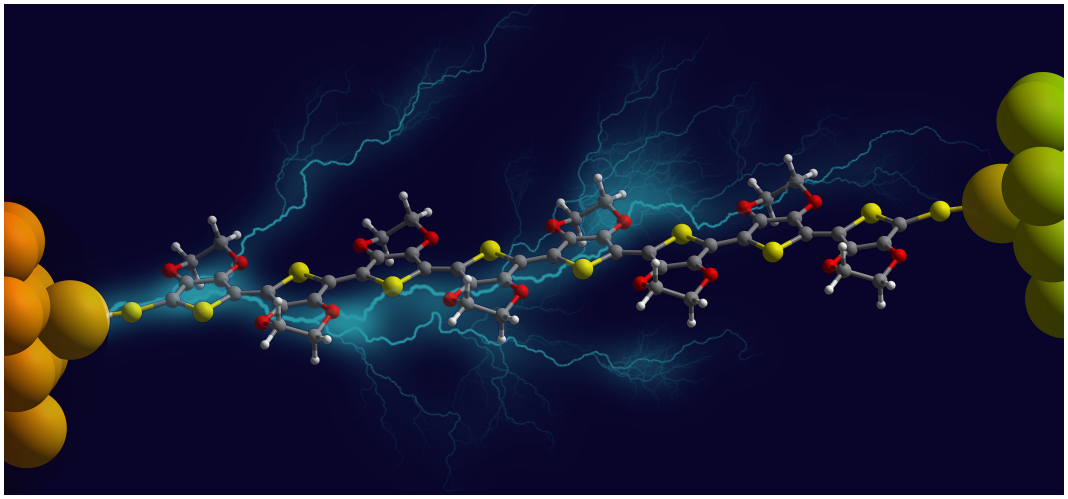

The design of thermoelectric materials for the efficient conversion of waste heat into electricity requires simultaneous tuning of their electrical and thermal conductance. A comparative theoretical study of electron and phonon transport in thiophene and ethylenedioxythiophene (EDOT) based molecular wires is performed. It is shown that modifying thiophene by substituting ethylenedioxy enhances the thermoelectric figure of merit ZT for molecules of the same length. Furthermore, it

is demonstrated that the electrical conductance of EDOT-based wires decays more slowly with length than that of thiophene-based wires and that their thermal conductance is lower. The room-temperature ZT of undoped EDOT is found to be rather low. However, doping of EDOT by the electron acceptor tolunenesulfunate increases the Seebeck coefficient and electrical conductance, while decreasing the thermal conductance, leading to a thermoelectric figure of merit as high as $ZT = 2.4$.

4.1 Introduction

The key property characterising the efficiency at which thermal energy is converted into electrical energy is the dimensionless thermoelectric figure of merit $ZT = GS^2T/\kappa$, where G is the electrical conductance, S is the Seebeck coefficient, T is temperature and κ is the thermal conductance. Therefore optimisation of ZT requires design of materials which maximise the numerator (ie. the power factor GS^2) and simultaneously minimise the denominator (ie. the thermal conductance). Strategies for increasing the power factor GS^2 of single-molecule junctions focus on optimising electron transport properties by tuning the energetic position of the frontier orbitals of the molecule relative to the Fermi energy E_F of the electrodes. If $T_{el}(E)$ is the transmission coefficient of electrons of energy passing from one electrode to the other through a molecule, then the Seebeck coefficient S is approximately proportional to the slope of the $-lnT_{el}(E)$, evaluated at E_F, whereas the electrical conductance is proportional to $T_{el}(E_F)$. Therefore, it is favourable to use molecular design to control the position of the resonances in $T_{el}(E)$, which occur when the electron energy E coincides with a molecular energy level.[35,112,113] The thermoelectric properties of bulk oligothiophene derivatives have received attention,[76,77,114–123] due to their conjugated nature, which provides π orbital overlap along the backbone of the molecule and favours electron transport. Moreover, chemical modification of the oligothiophenes can be used

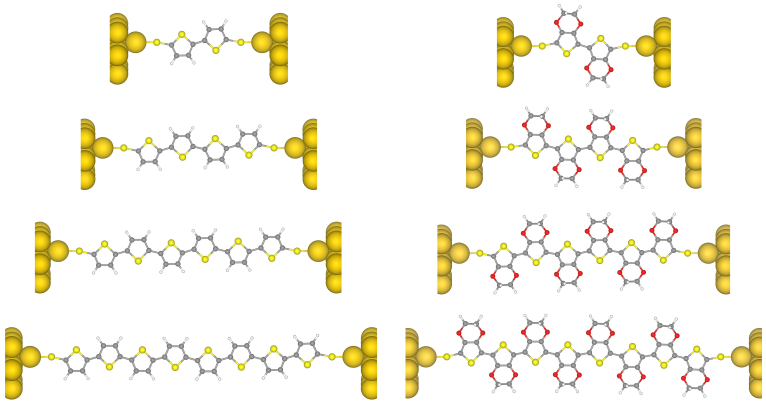

Figure 4.1: Optimised geometry of the thiophene series (left) and EDOT series (right) for n=1 to 4 units contacted between gold electrodes.

as a tool to improve their conductance.[34,116–123] Ethylenedioxythiophene (EDOT) is a derivative of thiophene obtained by ethylenedioxy substitution, which in its polymeric form is reported to reduce the charge carrier effective mass and the HOMO-LUMO gap.[116,122,123] The EDOT based organic polymer, in its doped form (PEDOT:PSS) has the highest recorded $ZT = 0.42$ for a bulk organic semiconductor.[76,77,120] Here we calculate and compare the ZT of a family of oligothiophene and EDOT-based single-molecule junctions as a function of their length. Our calculations reveal that in all cases, the ZT of EDOT exceeds that of the corresponding oligothiophenes. Furthermore, we have used Tolunenesulfunate (TOS) which is the building block of PSS,[77] an electron acceptor, for doping the EDOT monomer which results in significant improvement of ZT.

4.2 Conductance

The calculated room-temperature electrical conductances for the two series of thiophene and EDOT-based wires are shown in figure 4.3*a* and 4.3*b* respectively. All energy axes are plotted so that the DFT predicted Fermi energy (E_F^{DFT}) is at zero therefore the axes read $E - E_F^{DFT}$. The DFT-predicted Fermi energy ($E - E_F^{DFT} = 0eV$) sits close to the HOMO resonance in both cases and would lead to high conductance values (T1 has a value of $0.47G_0$ and E1 $0.48G_0$). Experi-

mental measurements on a thiophene series show a measured conductance value of $G = 3 \times 10^{-3} G_0$ and a Seebeck coefficient of $S = 8\mu V/K$ for molecule T1.[114] The discrepancy arises from the incorrect energy level alignment of the molecules with the Fermi energy of gold leads. This is a known problem in DFT-based quantum transport calculations and leads to overestimation of the conductance. Various methods have been employed to correct this including the DFT+Σ[124] and scissor corrections.[125] In the case of thiol based anchor groups, where the molecule desorbs a hydrogen atom on the gold, the application of these corrections is somewhat artificial, since the molecule without hydrogens does not exist in the gas phase. Therefore, in what follows, we use the measured conductance and Seebeck coefficient of T1 molecule to locate the relative position of the HOMO. Shifting the DFT predicted Fermi energy to $E_F - E_F^{DFT} = 0.35eV$ yields $G = 8 \times 10^{-3} G_0$ and $S = 20.3\mu V/K$ which is in reasonable agreement with the experimental measurements. Therefore, in what follows, we adopt this value of Fermi energy. (Fig. 4.2) Figure 4.3*c* shows the conductance $ln(G/G_0)$ vs L for the four different lengths of

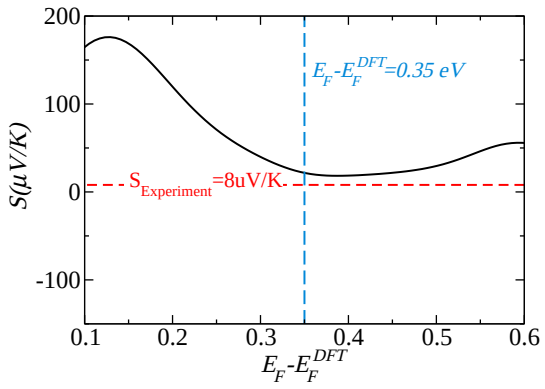

Figure 4.2: The Seebeck coefficient of T1 (black), Experimental value for the Seebeck coefficient of T1 (red) and the relatively chosen Fermi energy.

EDOT (red) and thiophene (black), and as expected for coherent tunneling, we find a clear exponential decrease of conductance with oligomer length in both cases ($G \sim e^{-\beta L}$). Figure 4.3*d* shows that the beta-factor obtained from the slopes of such plots at different Fermi energies (E_F), and demonstrates that the beta-factor of the EDOT series (E1-E4) is lower than that of thiophene ($1nm^{-1}$ to $1.75nm^{-1}$

respectively) over a range of Fermi energies in the vicinity of our chosen Fermi energy $E_F - E_F^{DFT} = 0.35eV$. Figures 4.3a and 4.3b show that the off-resonant conductance in the HOMO-LUMO gap is lower for the thiophene, due to the fact that the EDOT has a smaller HOMO-LUMO gap. This mirrors the comparable behaviour in polymers[116] and suggests that the observed reduction in the HOMO-LUMO gap is purely due to the chemical modification of the molecule. As noted in the literature,[116] the donor-type ethylenedioxy substitution causes anti-bonding interactions between the O and C on the molecule backbone, which destabilizes both HOMO and LUMO and leads to reduction of the gap. To optimise the nu-

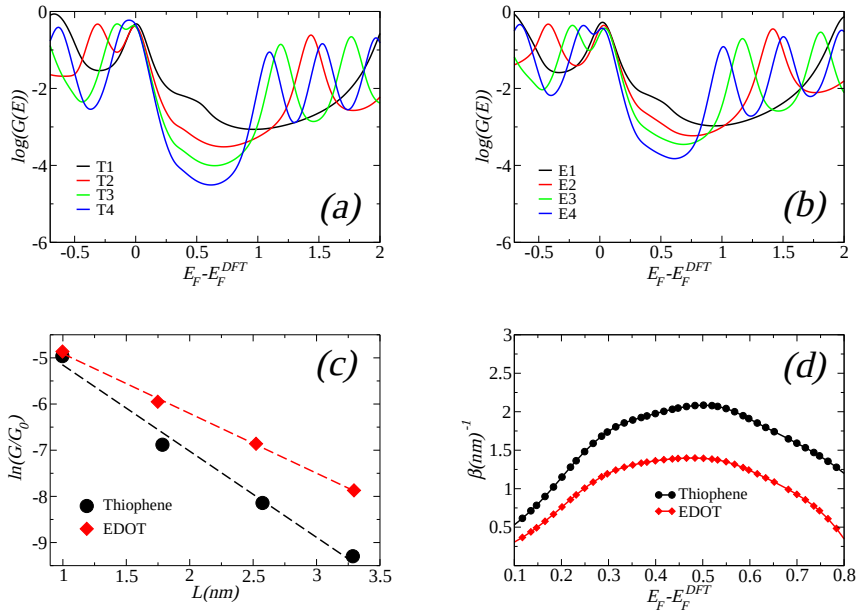

Figure 4.3: Room temperature conductance for the (a) thiophene (a) and (b) EDOT molecular wires shown in figure 4.1. (c) Conductance vs length at $E_F - E_F^{DFT} = 0.35eV$. (d) Beta factor vs. Fermi energy. The predicted value for the decay constant of oligothiophene is somewhat lower than the experimental value of $\beta = 2.9nm^{-1}$,[30,114] because DFT underestimates the HOMO-LUMO gap.

merator of ZT, we next investigate the Seebeck coefficient S. The value of S is proportional to the slope of the transmission at the Fermi Energy. This means that S is high when E_F is greater than the energy of HOMO resonance and smaller than the energy of the middle of the HOMO-LUMO gap. Figure 4.4 shows a comparison between the Seebeck coefficient of the thiophene and EDOT series in the vicinity of $E_F - E_F^{DFT} = 0.35eV$ For the same length of oligomer, the Seebeck co-

efficients of the EDOT series are lower than those of the thiophene series, because the higher HOMO-LUMO gap of the former leads to a lower mid-gap transmission coefficient and therefore to a higher slope. Figure 4.4 also demonstrates that in both molecular series, S increases with molecular length in agreement with previous work.[114,115] As shown in figure 4.4, this trend does not depend on the value of the Fermi energy.

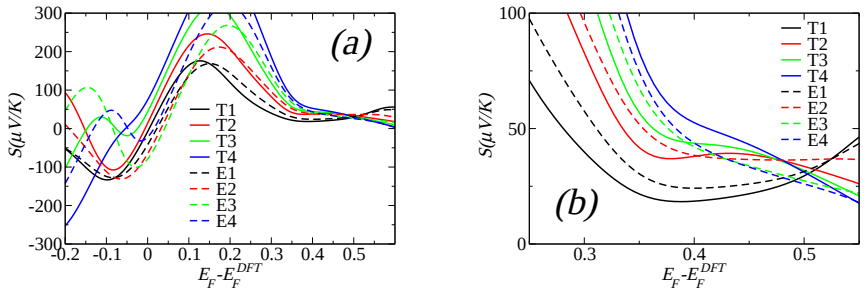

Figure 4.4: (a) Seebeck coefficient against Fermi energy for thiophenes and EDOTs over a range of $-0.2 < E_F - E_F^{DFT} < 0.6$ (b) Seebeck coefficient over a range of Fermi energy in the vicinity of chosen Fermi energy $E_F - E_F^{DFT} = 0.35eV$.

4.3 Thermal conductance

The thermal conductance $\kappa = \kappa_e + \kappa_{ph}$ in the denominator of ZT is composed of two terms: the thermal conductance due to electrons (κ_e) and the thermal conductance due to phonons (κ_{ph}). For both series, increasing the length of molecular wire has two effects on the transmission coefficient. The first is a narrowing of the phonon transmission resonances with increasing length, which reduces the thermal conductance. The second is an increase with length of the number of phonon modes below the Debye frequency of the electrodes, which tends to increase the thermal conductance ($23meV$ in the present calculations).[74] This trend can be followed in the transmission coefficient of both series in figure 4.5 and figure 4.6. These two factors control the area under the phonon transmission curves and therefore the integral in equation 3.27.[74]

As a result of this competition, for the EDOT series, although the longer molecules E3 and E4 have a lower thermal conductance than the shorter molecules E1 and E2, there is very little difference between E1 and E2, whilst E4 a slightly higher thermal conductance than E3. Similarly for the thiophene series, the phonon conductance of T2 is lower than that of T1, as expected. However, the thermal conductance then increases for T3 and T4, because due to mode softening, the number of modes entering the Debye window dominates. Similar non-conventional behaviour has been observed in recent measurements of alkane chains.[73]

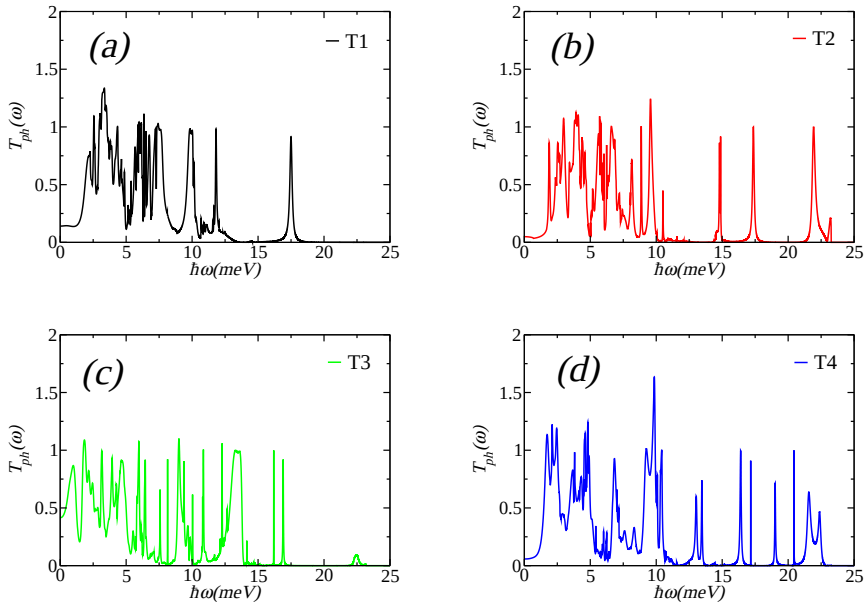

Figure 4.5: Phonon transport through the thiophene series.

As expected due to the discussion above, comparison between figure 4.7*a* and figure 4.7*b* reveals that the phonon contribution is greater than the electronic contribution. However the ratio κ_{ph}/κ_e is lower for the EDOT series than for the thiophene series, which makes the former more attractive for thermoelectricity. This is due to the higher value of κ_{ph} for thiophenes, which arises from rotational vibrational modes of the thiophene rings. These become more restricted after ethylenedioxy substitution and the phonon conductance of the EDOT series is lower than that of the thiophene series.[111]

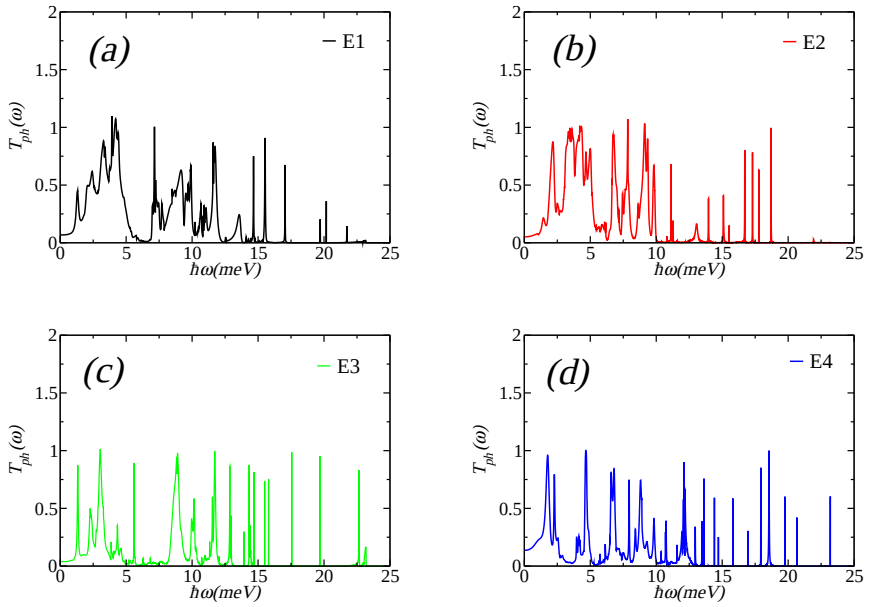

Figure 4.6: Phonon transmission through the EDOT series.

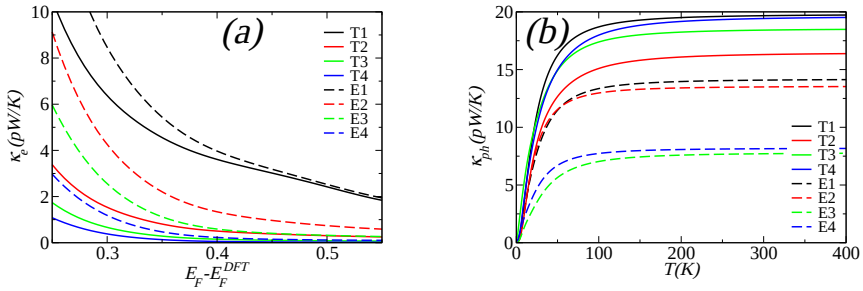

Figure 4.7: (a) The electronic thermal conductance at 300 K over a range of $E_F - E_F^{DFT}$ (b) the phonon thermal conductance of both the EDOT and thiophene series.

4.4 Figure of merit ZT

Figure 5 shows the thermoelectric figure of merit (ZT). At the benchmarked Fermi energy of $E_F - E_F^{DFT} = 0.35eV$ the value of ZT is much less than 1. However, at lower values of the Fermi energy, ZT of molecule E4 is as high as 3, because the system is closer to the HOMO resonance.

The combination of higher Seebeck coefficient and electrical conductance, as well as a lower κ_{ph}/κ_e ratio results in a much higher ZT for EDOT series in comparison with the thiophene series.

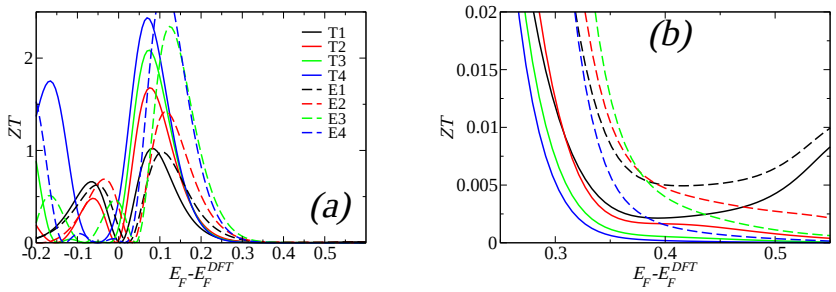

Figure 4.8: (a) ZT in a range of Fermi energy from -0.2 to 0.6 (b) over a range of Fermi energy in the vicinity of chosen Fermi energy $E_F - E_F^{DFT} = 0.35eV$

4.5 Doping EDOT

This suggests that ZT could be enhanced by doping with an electron acceptor, which would cause the molecular energy levels to increase in energy relative to the Fermi energy. To investigate the tunability of ZT via doping, we have doped EDOT monomer (E3) with Tolunesulfonate (TOS) which is an electron acceptor. The charge transfer process in an EDOT:TOS complex is discussed at length in the literature.[77]

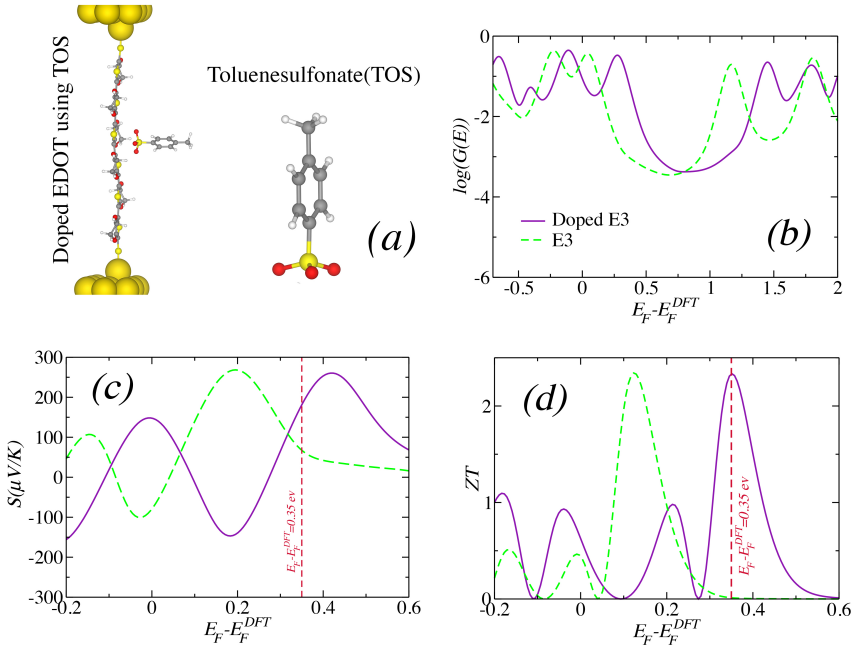

Figure 4.9: (a) Toluenesulfonate (TOS) and EDOT:TOS in the junction and the comparison between the logarithm of conductance (b), Seebeck coefficient (c) and the (d) ZT of E3 in a doped and undoped state.

The gold electrodes are the same in both calculations (with and without the dopant). Therefore, the Fermi energy is kept constant for both calculations and is $E_F - E_F^{DFT} = 0.35eV$. As expected, doping shifts the HOMO and LUMU hence bringing a higher slope towards the Fermi energy which yields to a significantly larger Seebeck coefficient and value of conductance. This results in a ZT value of 2.4.

4.6 Conclusion

We have studied the length dependence of the thermoelectric properties of thiophene and EDOT molecular wires. By converting the basic thiophene unit to EDOT, where a thiophene oligomer is modified by adding ethylenedioxy, we have demonstrated that the electronic conductance decay factor is smaller for EDOT and its thermal conductance is lower. Consequently, the thermoelectric performance of EDOT exceeds that of the corresponding oligothiophenes for all lengths studied. The room-temperature ZT of undoped EDOT was found to be rather low. However, doping of EDOT by the electron acceptor Toluenesulfonate (TOS), which moves the HOMO closer to the Fermi energy leads to room-temperature ZT values as high as 2.4.

Chapter 5

Cross-plane Conductance through a Graphene-Molecular Monolayer-Gold Sandwich.

The functionality offered by single-molecule electrical junctions have yet to be translated into monolayer or few-layer molecular films, where effective and reproducible electrical contact represents one of the challenging bottlenecks. Here we take a significant step in this direction by demonstrating that excellent electrical contact can be made to a monolayer biphenyl-4, 4'-dithiol (BPDT) molecular film, sandwiched between gold and graphene electrodes. This sandwich device structure is advantageous, because the current flows through the molecules to the gold substrate in a 'cross-plane' manner, perpendicular to the plane of the graphene, yielding high-conductance devices. We elucidate the nature of cross-plane graphene-molecule-gold transport using quantum transport calculations and introduce a simple analytical model, which captures generic features of the current-voltage characteristic. Asymmetry in junction properties results from the disparity in electrode electrical properties, the alignment of the BPDT HOMO-LUMO energy levels and the specific characteristics of the graphene electrode. The exper-

imental observation of scalability of junction properties within the junction area, in combination with the theoretical description of the transmission probability of the thiol-graphene contact, demonstrate that between 10%-100% of the molecules are contacted to the electrodes, which is several orders of magnitude greater than achieved to date in the literature.

5.1 Introduction

Single-molecule electronic devices, have been widely studied as a possible route to drive Moore's Law to the next level of sub-10 nm electronics.[126–128] Various methods have been used to explore electron transport characteristics of molecular structures, including scanning tunneling microscopy,[129] mechanical break junctions and eutectic gallium–indium junctions.[130,131] At the single-molecule level, quantum interference effects are particularly evident and open up many possibilities for functional design of electronic and thermoelectric devices.[132,133] However, for many of these applications, those features that are attractive at the single molecular level, should be scaled up to self-assembled molecular (SAM) films without losing the single-molecule functional advantages through inhomogeneous broadening, intermolecular interactions and defects.[134] For the study of vertical transport through SAM layers, direct evaporation of a metal top electrode onto organic molecules has not proved feasible as it leads to short circuits via pinholes in the organic layer. Various attempts have been made to overcome this problem, such as the addition of a conducting protective layer between the organic molecules and the top electrode.[61,135] Also, a mechanically transferred electrode has recently been reported to replace the direct formation of the metal electrode onto the SAM.[136] Nevertheless, a widespread observation is that scale up of junctions to practical device dimensions produce irreproducible properties that vary with the electrode choice. Moreover, it is observed that the (apparent) resistance per molecule increases by up to a factor of 108 in large area junctions (consisting of 103 to 108

molecules).[137–139] In addition, the unique properties of the organic molecules can be lost by the addition of the protective layer, and the minimum thickness of the transferred metal may limit miniaturization of the molecular devices. Graphene, as a monolayer of sp2 - hybridised carbon atoms,[140] offers an opportunity in this regard as it presents electron mobility of up to 106 $cm^2V^{-1}s^{-1}$ at room temperature,[141] ultralow resistivity,[142] ultrahigh breaking strength of 1 TPa and a controllable doping level.[143] However to date, monolayer CVD graphene-based solid state vertical transport devices have rarely been explored.[135,144]

The aim in this present work is to study the tunneling current through a self-assembled monolayer (SAM) of molecules sandwiched between two electrodes and to demonstrate that excellent electrical contact can be achieved. For this purpose, we sandwich a monolayer biphenyl-4, 4'-dithiol (BPDT) molecular film, between gold and graphene electrodes and measure the cross-plane current flowing perpendicular to the plane of the graphene, through the SAM and the gold. The aim of this study is to understand the fundamental characteristics of such graphene-SAM-gold devices. We chose BPDT for the molecular layer, because the single-molecule electrical conductance of BPDT has been measured and calculated and it is known to form a tightly packed SAM on gold.[145–147] In addition to detailed characterisation of the graphene-BPDT-gold sandwiches, we carry out calculations of their electrical conductance using density functional theory (DFT) combined with quantum transport theory. We also develop a simple analytical model, which captures the key features of room-temperature transport through such devices and enables qualitative understanding of device characteristics.

This project was a combined project with experimental groups in Imperial College London and Birmingham University.

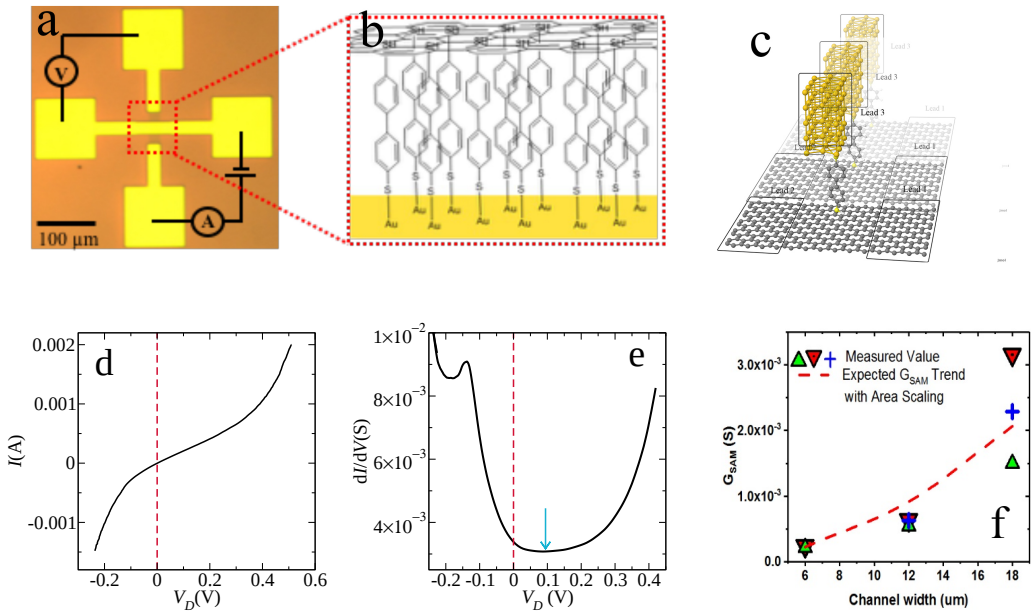

Figure 5.1: (a) Optical image (graphene is shown as light grey colour) (b) cross-section schematic illustration of the vertical transport device. (c) Au/BPDT/graphene model used for calculations. Representative (d) I-V and (e) dI/dV vs V characteristics of the vertical transport device (offset of the minimum differential conductance indicated by the blue arrow). (f) The experimentally determined zero bias conductance (G_{SAM}) versus junction width. The red dash curve is a guide to show the expected trend of G_{SAM} with junction area assuming 100% coverage.

5.2 The I-V characteristics of the device

To characterise precisely the conductance across graphene/BPDT/Au sandwiches, individual devices are designed in a four-probe configuration. The horizontal bottom electrode is made of Cr($2nm$)/Au($60nm$) on top of SiO_2/Si substrate, while the top graphene electrode is located between two Au contacts. The current imposed between one pair of graphene/Au arms and the voltage drop is measured across the other pair, as shown in figure 5.1a.

Due to the π-π interaction between parallel benzene rings in BPDT molecules, the molecular layer is packed tightly onto the surface of the Au electrode, avoiding a short circuit between the graphene and Au electrodes, as shown in figure 5.1b.

Figure 5.1d shows the experimentally measured current-voltage (I-V) characteris-

tic of a $18 \times 18\mu m^2$ graphene/BPDT/Au device. The corresponding differential conductance dI/dV is shown in figure 5.1*b*. Figure 5.1*f* illustrates how the zero bias conductance varies with junction width. The scaling is close to that expected from the variation of the junction area, which suggests a rather uniform connectivity of molecules to the graphene top contact particularly for the smaller junctions. The zero-bias conductance of the $18\times18\mu m^2$ junction is estimated to be $G_{SAM} = 3 \times 10^{-3}S$ (the value of conductance at $V = 0$ in figure 5.1*e*). To obtain the average zero-bias conductance per molecule G_M of the SAM, we first estimate the number of molecules (N) in the film and then write, $G_M = G_{SAM}/N$. To estimate the number of molecules per unit area x of our thin film, we carried out cyclic voltammetry analysis, which yielded a charge density of $(62 \pm 2) \times 10^{-6}(C \cdot cm^{-2})$. The corresponding number of molecules per unit area is therefore,

$$x = \frac{(62 \pm 2)\Delta 10^{-6}}{1.602 \times 10^{-19}C} = (3.75 \approx 4.00) \times 10^{6}(\mu m)^{-2}. \tag{5.1}$$

Since the area of the SAM is $18 \times 18\mu m^2$, the total number of molecules is $N = (1.2 \sim 1.3) \times 10^9$ and therefore $G_M = G_{SAM}/N = (2.3 \sim 2.5) \times 10^{-3}nS$. Ideally, we would like to compare this with a direct measurement of the single-molecule conductance of BPDT in a single-molecule gold-BPDT-graphene device. Unfortunately, such measurement is not straightforward: in the absence of a covalent BPDT-graphene interaction, this would most likely require a graphene-based (flat) 'tip' to contact an individual BPDT molecule immobilised on Au. When both electrodes are gold, the measured conductance of a single BPDT molecule obtained by STM is $1.82nS$ under ambient conditions. However, the DFT modelling (Fig.5.2*a*.) predicts that the conductance of a single BPDT molecule calculated between gold and graphene electrodes should be approximately a factor of $10^{-2} \sim 10^{-3}$ lower than this value, which leads to a calculated G_M of $G_M = 10^{-2} \sim 10^{-3}nS$. Bear in mind that the experimental value of conductance for single molecule between gold and graphene electrodes can be predicted using the calculated ratio given in the

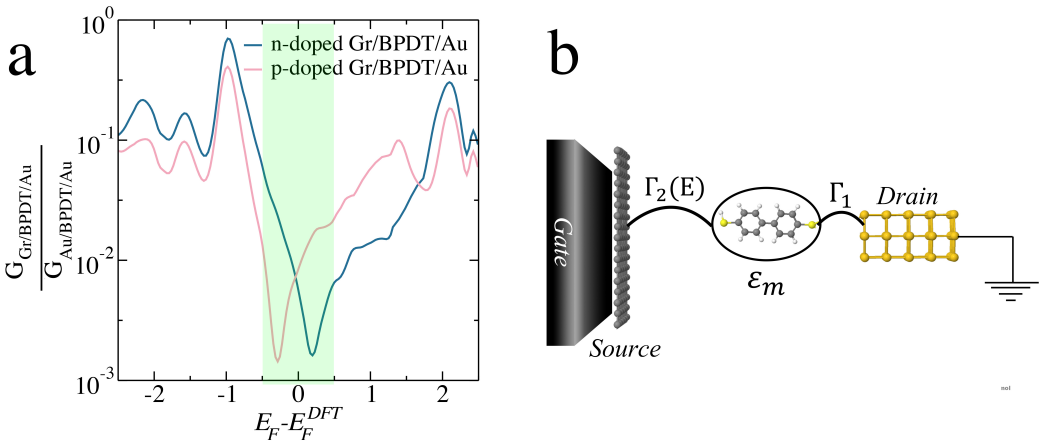

Figure 5.2: (*a*) The predicted room-temperature electrical conductance of a n-doped graphene/BPDT/Au junction (blue) and a p-doped graphene/BPDT/Au (pink), divided by the room temperature single-molecule conductance of the Au/BPDT/Au junction. The predicted ratio depends on the doping of the graphene and on the precise location of the Fermi energy E_F relative to the frontier orbitals of the molecule. However, over a range of such values in the vicinity of the DFT-predicted Fermi energy (shown shaded in green) the ratio varies from 10^{-2} to 10^{-3}. (*b*) Overview of the parameters involved in the generic model where $\Gamma_{1,2}$ are level broadening due to contact with the source and drain and ε_m is maximum energy of the molecular orbital.

following equation

$$G_M = G^{exp}_{Au/BPDT/Au} \times \frac{G^{Calc}_{Au/BPDT/Gr}}{G^{Calc}_{Au/BPDT/Au}}, \tag{5.2}$$

where $G^{exp}_{Au/BPDT/Au}$ is the experimentally measured conductance of a single molecule from STM, $G^{Calc}_{Au/BPDT/Gr}$ is the calculated single molecule conductance between a gold and graphene electrode and $G^{Calc}_{Au/BPDT/Au}$ is the calculated single molecule conductance between two gold electrodes.

Comparison with our measured value of $G_M = 2.3 \times 10^{-3} nS$ as well as the approximate scaling of the conductance with junction area (shown in figure 5.1*f*, leads us to conclude that between 10% and 100% of the molecules in our SAM are electrically-connected to the electrodes.

The conductance of the $G_{Au/BPDT/Au}$, $G_{Au/BPDT/Gr}$ with n-doped and p-doped graphene is shown in figure 5.3.

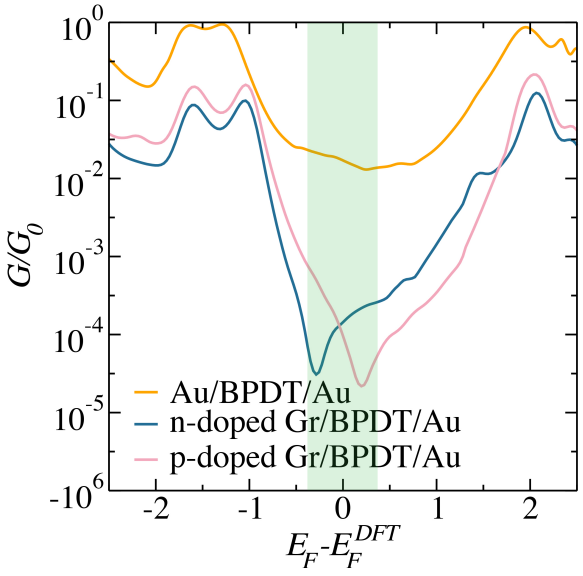

Figure 5.3: The predicted room-temperature electrical conductance of a n-doped graphene/BPDT/Au junction (blue) and a p-doped graphene/BPDT/Au (pink), and Au/BPDT/Au (yellow) in units of G_0. The predicted ratio of conductance per molecule for graphene/BPDT/Au to Au/BPDT/Au depends on the doping of the graphene and on precise location of the Fermi energy E_F relative to the frontier orbitals of the molecule. However, over a range of such values in the vicinity of the DFT-predicted Fermi energy the ratio varies from 10^{-2} to 10^{-3}.

5.3 Analytical model

To describe this interplay, we recall the Breit-Wigner formula for the transmission coefficient $T(E)$ describing electrons of energy E passing from a source to a drain via a single molecular energy level,[22]

$$T(E) = \frac{4\Gamma_1\Gamma_2}{(E-\varepsilon)^2 + (\Gamma_1+\Gamma_2)^2}. \tag{5.3}$$

In this expression, Γ_1 and Γ_2 are the level broadening due to contact with the source 1 and drain 2, while ε is the energy of the molecular orbital, shifted slightly by the real part of the self-energy due to the contacts. Clearly, when $E = \varepsilon$, $T(E)$ achieves a maximum value of

$$T(E) = \frac{4\Gamma_1\Gamma_2}{(\Gamma_1+\Gamma_2)^2}. \tag{5.4}$$

and for a symmetric junction where $\Gamma_1 = \Gamma_2$, $T_{max} = 1$. The quantity Γ_1 involves a product of the local density of states in the source electrode, the matrix element coupling the molecular orbital to the source and the amplitude of the molecular orbital in the vicinity of the contact to the source. The quantity Γ_2 involves corresponding quantities evaluated at the drain. If the source is gold, whose local density of states is almost energy independent on the scale of the level broadening and k_BT, then Γ_1 is approximately independent of energy. On the other hand if the drain is graphene, whose local density of states is reduced near the Dirac point, Γ_2 is energy dependent and is a minimum at the Dirac point. Therefore in a gold-molecule-graphene junction Γ_1 will depend on both the source-drain voltage V_D and (in a three-terminal device) on the applied gate voltage V_G. In general, ε will also depend on these voltages and therefore for a gold-SAM-graphene device, the transmission per molecule will take the form

$$T(E, V_D, V_G) = \frac{4\Gamma_1\Gamma_2(E, V_D, V_G)}{(E - \varepsilon(V_D, V_G))^2 + (\Gamma_1 + \Gamma_2(E, V_D, V_G))^2}. \tag{5.5}$$

where Γ_1 and $\Gamma_2(E, V_D, V_G)$ are the level broadenings. In a pristine monolayer device, Γ_2 would vanish at the Dirac point, but in a real device, due to inhomogeneous broadening, Γ_2 will not vanish precisely. Therefore we assume an energy dependence of the form

$$\Gamma_2(E, V_D, V_G) = \Gamma_0 + \alpha[E - E_{Dirac}]^z. \tag{5.6}$$

In this equation the exponent z characterizes the energy dependence of the average density of states in the graphene, whose spatially-averaged Dirac point is E_{Dirac}. Since the latter can be tuned by both V_D and V_G, we assume a simple linear dependence

$$E_{Dirac} = E_0^{Dirac} - \gamma_D|e|V_D - \gamma_G|e|V_G \tag{5.7}$$

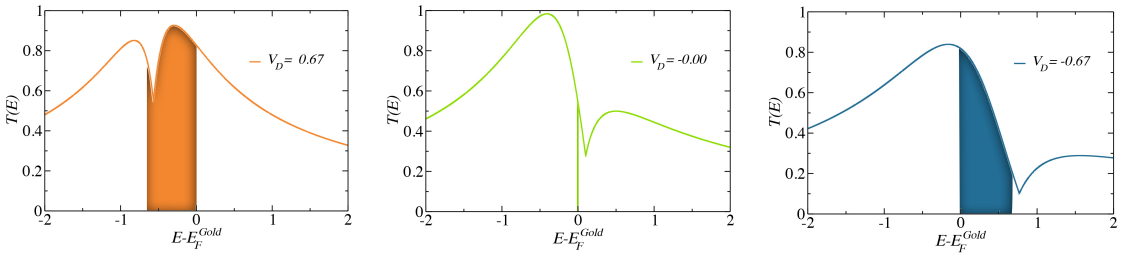

Figure 5.4: The current at a given source and gate voltage is obtained by integrating the transmission curve $T(E, V_G, V_D)$ over energies between E_F^{Gold} to $E_F^{Gold} - |e|V_D$.

and similarly we write for the location of the molecular orbital relative to the Fermi energy of gold.

$$\varepsilon - E_F^{Gold} = \varepsilon_m - \beta_D|e|V_D - \beta_G|e|V_G, \tag{5.8}$$

where β_D, β_G, γ_D and γ_G are the lever arms which can vary in different experiments. If $\gamma_D = 1$ and $V_G = 0$, then adjusting V_D does not change the charge on the graphene, whereas if $\gamma_D < 1$, the graphene acquires charge when V_D is non-zero. Since the molecule is strongly bound to the gold and very weakly bound to the graphene, the energy levels of the molecule are less affected by the source drain voltage and therefore in what follows we assume $\beta_D = 0$. The absence of an electrostatic gate in our experiments is reflected in the model by choosing $\beta_G = 0$ and $\gamma_G = 0$. The current is then given by

$$I(V_D, V_G) = \int_{E_F^{Gold}}^{E_F^{Gold} - \gamma_D|e|V_D} T(E, V_D, V_G)dE, \tag{5.9}$$

where $I_0 = 2e/h$. This means that a Dirac point entering the integration area would appear as a dip in the dI/dV curve and the position of the Lorentzian (Eq. 5.6) relative to the Dirac point would create asymmetry in the dI/dV.

Figure 5.4 shows examples of transmission functions at three different drain voltages. The asymmetry and dip in the dI/dV can appear in four different forms depending on the doping of the graphene and whether the transport is HOMO or

LUMO dominated (ie. if E_F^{Gold} lies closest to the HOMO or closest to the LUMO). As shown in figure 5.5, if the graphene is electron doped the dip will appear at negative bias voltages. For systems with p-doped graphene, it appears at positive bias voltages. It is worth mentioning that the units of conductance and current used in these plots are $G_0 = 2e^2/h$ and $I_0 = 2e/h$. Figure 5.6 shows the four possibilities for when $z = 2$.

The broad minimum in the experimental differential conductance plot figure 5.1e suggests that there is a distribution of Dirac points within the device, associated with inhomogeneities in the doping. To simulate this effect we average twenty differential conductance plots (light grey in Figure 5.7a) with slightly different Dirac points, whose average yields the red curve in Figure 5.7a. The fitted parameters in the red curve of Figure 5.7a suggest that in the experiment, graphene is overall p-doped and transport is LUMO dominated. Note that the broadening of the minima can also be modelled for higher orders of the exponent in equation 5.6 (Fig. 5.6).

To check if this is consistent with the film properties, we performed Kelvin Force microscopy (KFM) and RAMAN spectroscopy measurements to determine the doping of the graphene. Figure 5.7b shows the work function image of the graphene/ BPDT/Au junction area (blue-ish squares). From this image, it is clear that the graphene electrode over the gold/BPDT area is differently doped with respect to the graphene on the bare SiO_2 surface. Within the junction area, the graphene lying on BPDT shows a distribution of surface properties. The specific patterns are attributed to the surface arrangement of the BPDT molecules after the solvent drying process. The blurry edges between electrodes and SiO_2 are attributed to surface charging on the insulating SiO_2 substrate. Statistical analysis of the work function difference within the junction areas is compared to that of the graphene on SiO_2 presented in Figure 5.7c. The centre of the distribution shifts negatively indicating that graphene is more electron doped when transferred onto BPDT in comparison with graphene on SiO_2. The KFM images show the difference in work

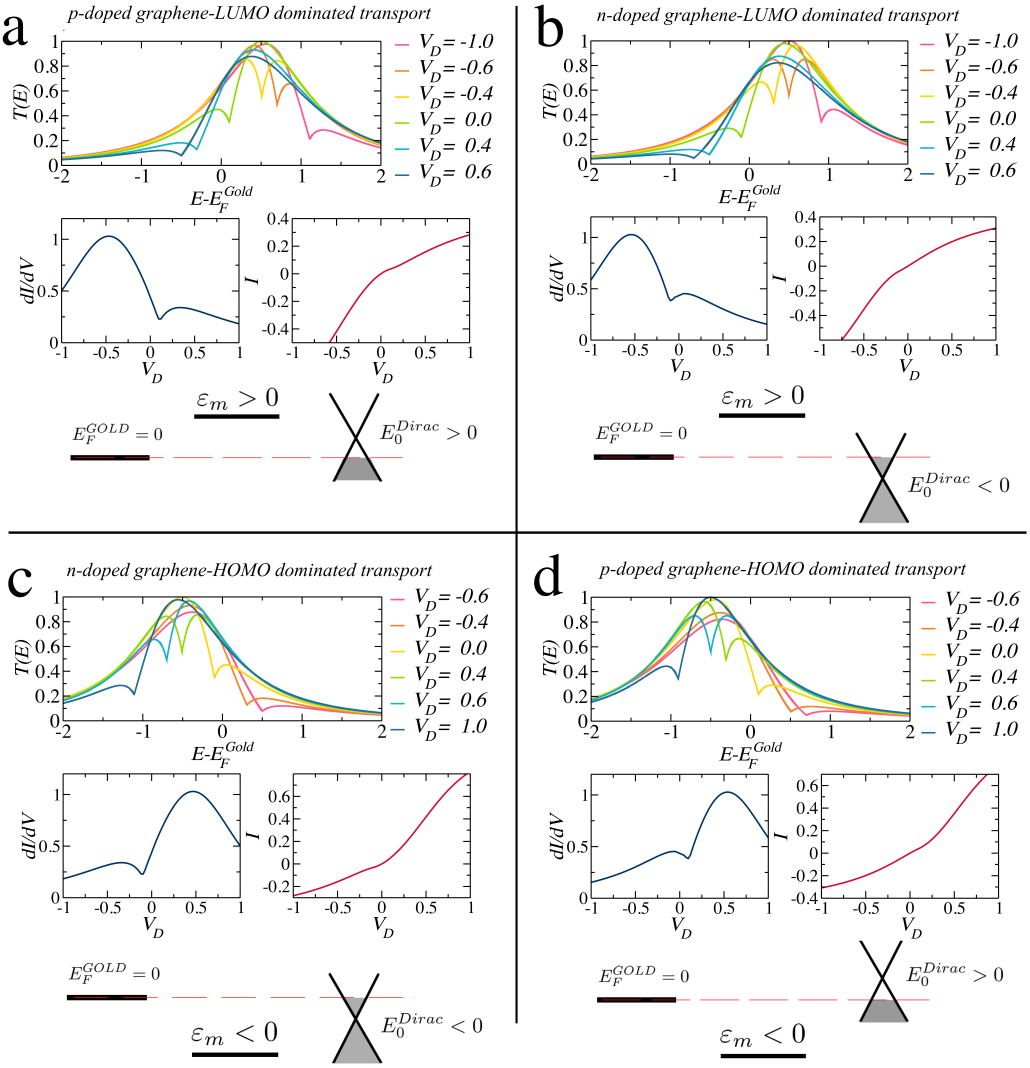

Figure 5.5: Four possible scenarios for the dip and asymmetry in dI/dV curve of $Gr/SAM/Au$ devices. The transport and graphene are (a) LUMO and p-doped ($E_{Dirac} = 0.1$ and $\varepsilon_m = 0.5$) (b) LUMO dominated, n-doped ($E_{Dirac} = -0.1$ and $\varepsilon_m = 0.5$) (c) HOMO dominated, n-doped ($E_{Dirac} = -0.1$ and $\varepsilon_m = 0.5$) and (d) HOMO dominated, p-doped ($E_{Dirac} = +0.1$ and $\varepsilon_m = 0.5$). For all four scenarios $\Gamma_0 = 0.1$, $\alpha = 1$ and $z = 1$. In each quadrant, the transmission coefficient $T_e(E)$ vs energy $E - E_F^{Gold}$ (the energy, relative to the Fermi energy of the gold) is plotted at various drain voltages V_D (top graph), the differential conductance (dI/dV) and the current (I) verses the drain voltage are plotted (middle graphs left and right, respectively) and a schematic showing the position of the Fermi energy of the gold relative to graphene (bottom diagram).

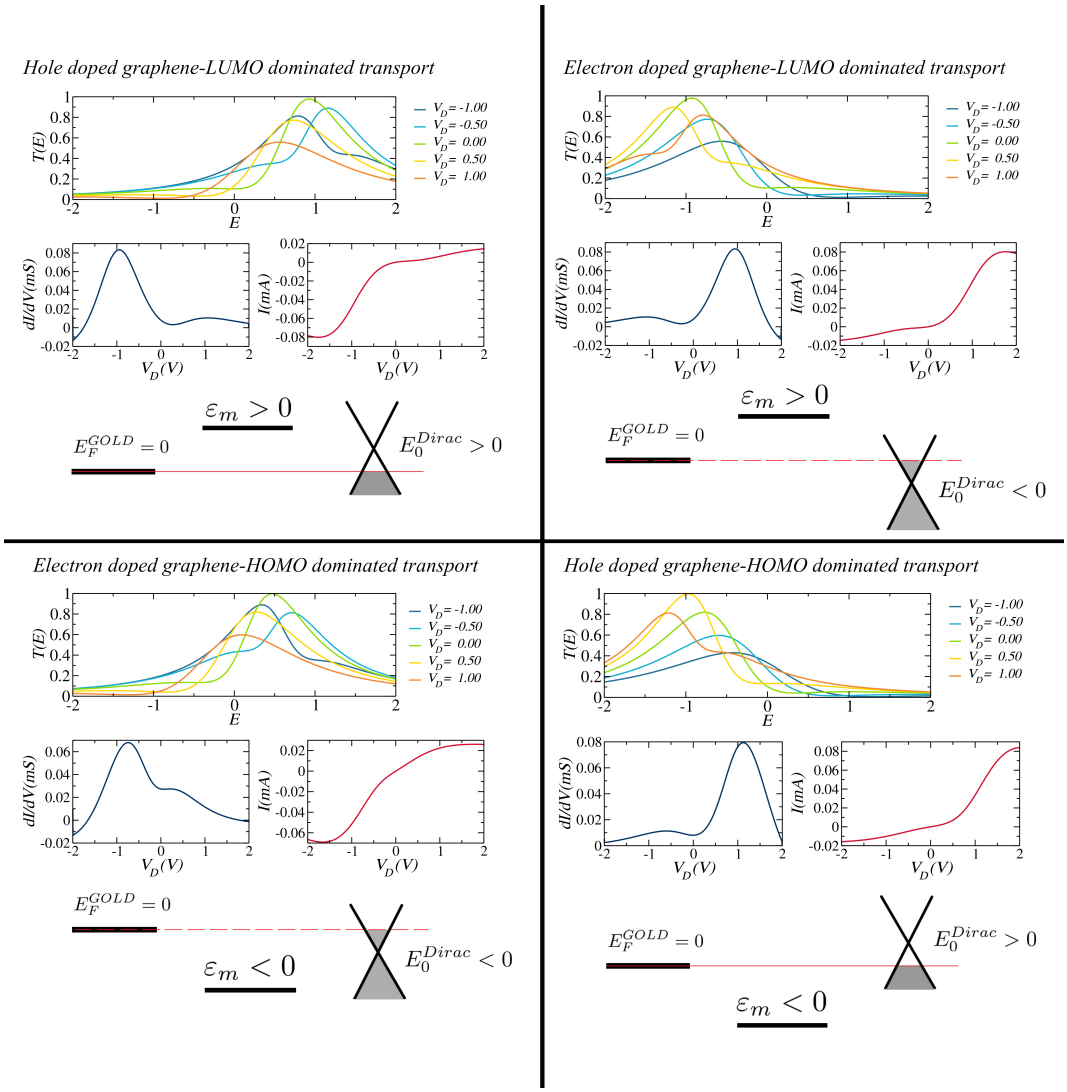

Figure 5.6: Four possible scenarios for the dip and asymmetry in dI/dV curves. All parameters are the same as 5.5 except for the exponent in equation 5.6, $z = 2$.

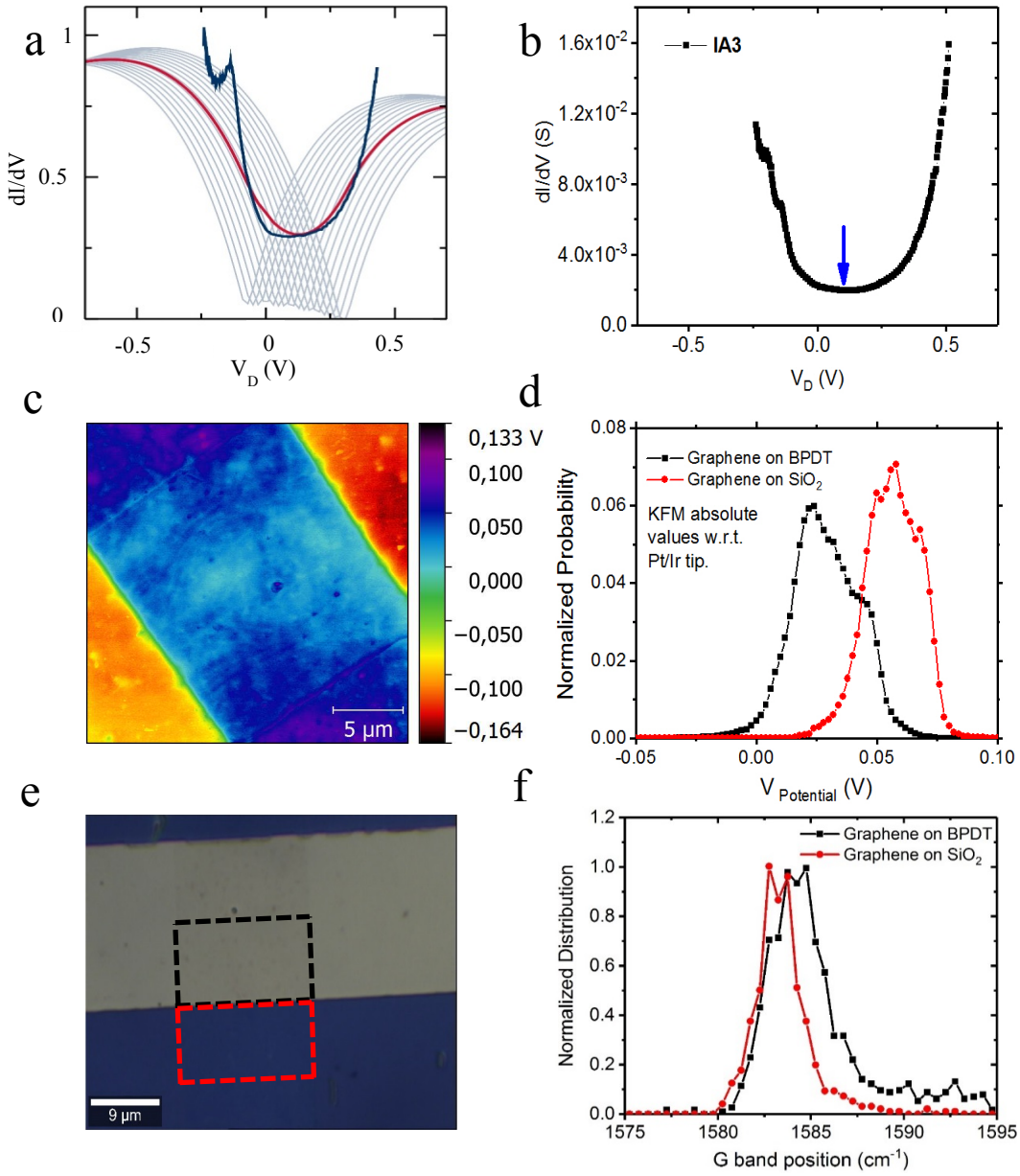

Figure 5.7: (a) The theoretical model (red) fit to the experimental dI/dV (blue) for the parameters, $\Gamma_0 = 0.003$, $\alpha = 1$, $\gamma_0 = 0.002$, $\gamma_1 = 1$, $\varepsilon_m = 0.1$ and $-0.1 < E_0^{Dirac} < 0.4$. (b) The differential conductance characteristics of IA3 (minimum indicated by blue arrows). (c) KFM work function mappings of device IA3 with respect to the gold tip. (d) The corresponding statistical analysis of the work function across the junction area on BPDT of IA3 as well as one of the areas where graphene lies on the SiO_2. (e) Optical images of the mapped graphene areas on IA3. (f) Corresponding statistical analysis of G band position.

function with respect to the work function of KFM tip; the absolute values of the peak positions do not provide quantitative information, but since they are offset by the same amount, the difference between the positions of the two peaks is a meaningful quantity. Notably, CVD graphene under ambient conditions on SiO_2, is always p-doped. This is due to the charge transfer to the substrate as well as adsorption of water molecules and other contaminations from air, which act as the hole dopants.[148] In these vertical transport devices, graphene becomes more heavily p-doped when it is transferred onto BPDT, attributed to the combined influence of the BPDT molecules and the Au electrode at the far end of the graphene strip.[149] Raman spectroscopy analysis is provided in figure 5.7*e* and *f*. The white horizontal bars are Au bottom electrodes, whilst the darker grey squares are the cross-plane SAM-based junctions. Raman spectroscopy has been carried out across a similar area including graphene on BPDT (outlined as black dash line) and graphene on bare SiO_2 (outlined as red dash line). The position of G band positively shifts from 1583 cm^{-1} to 1584 cm^{-1}, when graphene is doped by BPDT/Au stack. Positively shifted peaks indicate the graphene is p-doped as the theoretical model predicts. In addition to the shifted distribution centre, the full-width half-maximum (FWHM) of the distribution characteristics have also increased, indicating a more dispersed and inhomogeneous doping condition with the effect from BPDT/Au stack underneath.[150]

5.4 DFT Modelling the I-V characteristics of the device

In addition to the analytical model of equation 5.5, we performed DFT-based modelling of the geometry-optimised structure shown in figure 5.1*c*. To construct the system, the ground state Hamiltonian and optimized geometry of each molecule was obtain using local density approximation (LDA) exchange correlation func-

tional along with double-ζ polarized (DZP) basis sets and the norm conserving pseudo potentials. The real space grid is defined by a plane wave cutoff of 185 Ry. The geometry optimization was carried out to a force tolerance of $0.01eV/A$. This process was repeated for a unit cell with the molecule between gold and graphene electrodes where the optimized distance between graphene and the thiol anchor group was found to be $2.9\mathring{A}$. Figure 5.1*c* shows a unit cell of the system analysed, in which each unit cell contains a single BPDT molecule and the whole structure is repeated periodically by summing over k-points in the transverse direction of graphene plane. Electron flow is assumed to be from the source (gold electrode), through BPDT and into the drain (planar graphene electrode).

To model the source-drain and gate voltage in the experiment we use a model where the gold lead is earthed, therefore the Fermi energy of gold (E_F^{Gold}) is not affected by source drain or gate voltage. However, the Fermi energy of graphene is a function of source drain and gate voltage (Eq. 5.10)

$$E_F^{Gr}(V_D, V_G) = E_F^{Gold} - \gamma_D V_D - \gamma_G V_G, \tag{5.10}$$

where all variables are consistent with section 5.3. The devices in this study are not gated (ie. $\gamma_G = 0$) and mentioning the gate voltage in the formalism is purely to maintain generality. In order to introduce a source-drain voltage to the mean-field Hamiltonian obtained from DFT, consider the Bloch Hamiltonian of one of the leads

$$H_0 \left|\psi_j\right\rangle + H_1 \left|\psi_{j+1}\right\rangle + H_1^\dagger \left|\psi_{j-1}\right\rangle = ES \left|\psi_j\right\rangle, \tag{5.11}$$

where H_0 is the Hamiltonian of each building block (principle layer), H_1 is the coupling between two principle layer, S is the overlap matrix. Assuming $|\psi_j\rangle$ to be a plane wave,

$$\left|\psi_j\right\rangle = \left|\chi\right\rangle e^{ikj}, \tag{5.12}$$

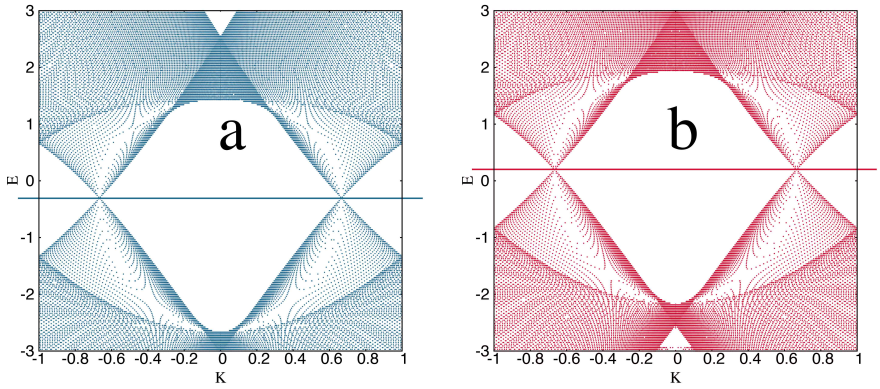

Figure 5.8: (a) n-doped and (b) p-doped graphene at zero bias voltage with 16 K points in the transverse direction.

we have,

$$\left(H_0 \left|\psi_j\right\rangle + H_1 \left|\psi_{j+1}\right\rangle + H_1^{\dagger} \left|\psi_{j-1}\right\rangle\right) \left|\chi\right\rangle = ES(k) \left|\chi\right\rangle . \tag{5.13}$$

In order to make a rigid shift in the energy spectrum (in accordance to the source-drain voltage), we make the following change to the Hamiltonian

$$H_{lj} \rightarrow H_{lj} + \varepsilon S_{lj}, \tag{5.14}$$

where $\varepsilon = -\frac{e|V_D}{2}$. One can calculate the transmission coefficient at each voltage point and then obtain the current using equation 5.9. The dI/dV curves are obtained by simply differentiating the $I-V$. The band structure of the graphene obtained using the method explained above for a p-doped and n-doped system is demonstrated in figure 5.8.

At zero bias, figure 5.9a shows the computed transmission coefficient as a function of electron energy E. Since the graphene is doped in the experiments, we apply a small shift to the band structure of the graphene to mimic hole doping (Fig. 5.9a red curve) and electron doping (Fig.5.9a blue curve), where the former is relevant to our experiments. To account for asymmetry in the junction, at finite source-drain voltage, we re-calculate the transmission coefficient at each source drain-voltage to yield the series of finite-bias transmission curves shown in figure 5.9b, from which we obtain the finite-bias current and the differential conductance

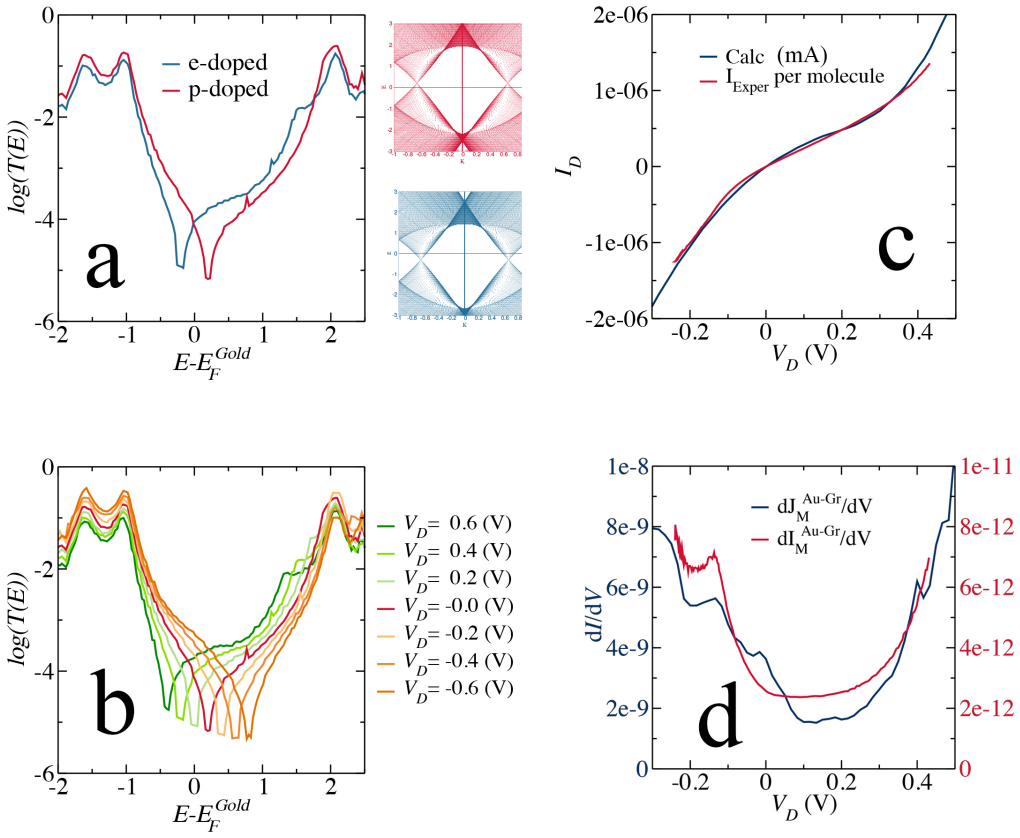

Figure 5.9: (a) Transport through a SAM with p-doped and n-doped graphene at zero bias voltage. (b) The logarithm of transmission vs the energy relative to the Fermi energy of gold at various source drain voltages. (c) Comparison between experimental and theoretical current (d) comparison of the average calculated dI/dV for differently doped systems (blue) with the experimental dI/dV (red). The units of conductance and current used in these plots are $G_0 = e^2/h$ and $I_0 = 2e/h$. Although the asymmetry and the lowest conductance point in curve is similar to the experimental data, the absolute value of the calculated conductance is greater than that of experiment, in common with DFT transport calculations reported in the literature and therefore the vertical axes have been scaled to aid comparison.

shown in figure 5.9*c* and *d*. To obtain the latter, we noted that the work function of gold is greater than that of graphene, so electrons are expected to transfer from the graphene to the SAM/gold complex. The positively-charged graphene acts like a positive electrostatic gate and lowers the energy levels of the SAM relative to the Fermi energy of gold. This moves the LUMO of the molecules closer to the gold Fermi energy and results in LUMO dominated transport, as also suggested by the analytical model. To account for this shift and the fact that the graphene doping varies over the area of the device, we computed the average of three I-V curves for Fermi energies of the gold in the range $0.6 \pm 0.1eV$. The resulting average I-V and dI/dV curves are shown in Figure 5.9*c* and *d*. The model captures all the essential features of the experimental curves.

It is important to bare in mind that the EGF method (which is used in this work) is only valid in the regime that the thermal broadening (K_BT) and the coupling to the electrodes are comparable to the coulomb energy. Therefore it can only be used for tunnelling regime. In the limits where electrons travel through an energy level at a large rate, this theory is not valid and one might adopt other approaches such as master equation approach. In this study applying the gate voltage will change the Fermi energy with respect to the molecular energy levels. Therefore for large gate voltages, on-resonance tunnelling would occur and the current method will not be valid. However, as demonstrated, this is not the case in the experiments and theoretical calculations presented in our work. Hence, the EGF method is valid and provides a good comparison with the experiments.

5.5 Conclusion

In summary, the behaviour of cross-plane electron transport through a monolayer graphene/BPDT/Au junction has been investigated using a four-probe measurement. The asymmetric electrical transport characteristics observed in both I-V

and dI/dV vs V measurements, arise from the asymmetric structure of the junction, combined with phase-coherent tunneling of electrons from the gold to the graphene via the SAM. These are described using density functional theory and a generic analytic model, which captures the interplay between the energetics of molecular orbitals, the Dirac point of the graphene and inhomogeneity of doping across the area of the graphene electrode. Comparison between single-molecule conductance measurements as a function of junction area, combined with DFT modelling suggests that between 10% and 100% of the molecules make electrical contact to the larger area electrodes and approaching 100% make contact in our smaller junctions. This result is encouraging and indicates that Au-SAM-graphene sandwiches provide an efficient route to electrically contacting SAMS, while preserving cross-plane phase-coherent transport.

Chapter 6

Quantum interference mediated vertical molecular

Molecular transistors operating in the quantum tunneling regime, represent potential electronic building blocks for future integrated circuits. However, due to their complex fabrication processes and poor stability, traditional molecular transistors can only operate stably at cryogenic temperatures. Here through a combined experimental and theoretical investigation, we demonstrate a new design of vertical molecular tunneling transistors, with stable switching operations up to room temperature, formed from cross-plane graphene/self-assembled monolayer (SAM)/gold heterostructures. We show that vertical molecular junctions formed from pseudo-p-bis((4-(acetylthio)phenyl)ethynyl)-p-[2,2]cyclophane (PCP) SAMs exhibit destructive quantum interference (QI) effects, which are absent in 1,4-bis(((4-acetylthio)phenyl)ethynyl)benzene (OPE3) SAMs Consequently the zero-bias differential conductance of the former is only about 2% of the latter, resulting in an enhanced on-off current ratio for (PCP) SAMs. Field-effect control is achieved using an ionic liquid gate, whose strong vertical electric field penetrates through the graphene layer and tunes the energy levels of the SAMs. The resulting room-temperature on-off current ratio achieved in PCP SAMs can reach

up to $\sim$ 330, about one order of magnitude higher than that of OPE3 SAMs. The demonstration of molecular junctions with combined the QI effect and gate-tunability represent f4a critical step towards functional devices in future molecular-scale electronics.

6.1 Introduction

Molecular electronics represents an attractive alternative for future electronic devices with rich functionalities beyond current scaling limits.[151,152] Since molecular electronic devices can operate in the quantum tunneling regime, even at room temperature, numerous quantum phenomena at the sub-nanometre scale can be explored, such as nuclear spin resonance,[153] quantum plasmons,[154] thermoelectric effects[37] and quantum interference (QI) effects.[22,155] Furthermore, with properly designed device structures and functional molecules,[156] various functions can be implemented in molecular tunnel junctions, such as switches,[157–159] diodes[160,161] and transistors.[162,163] Normally, molecular tunneling transistors, which are the most probable electronic element in future integrated circuits, are fabricated by placing a solid back gate[164] or electrochemical gate[165] to the side of molecular junctions to tune the energy levels of the central molecules. However, due to the complex device fabrication processes and low stability of such devices, these molecular transistors can typically only operate stably at cryogenic temperatures. Here, we report a novel design of a vertical molecular tunneling transistor with stable operation up to room temperature, based on a gate/graphene/self-assembled-monolayer (SAM)/gold cross-plane vertical heterostructure.[166,167] Since destructive QI suppresses molecular conductance at low-bias,[22] which is beneficial for creating molecular transistors with high on-off current ratio, we have investigated SAMs formed from molecules with and without destructive QI effects.[168] The conformation and binding geometry of the molecules in the SAM are fixed[169] by thiol anchor groups to the gold electrode, which promotes stable charge transport through the molec-

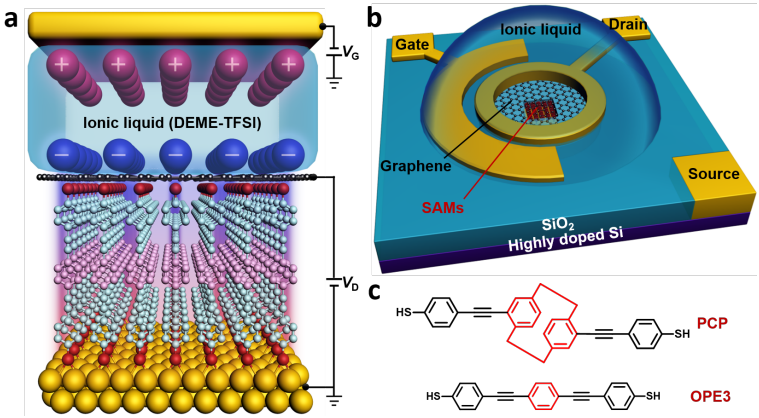

Figure 6.1: Schematic illustration of the vertical molecular tunnel transistor. (a) Schematic illustration of the device structure for the fabricated device. (b) Schematic diagrams of the molecular transistor with OPE3 SAMs and ionic liquid (DEME-TFSI) gating. DEME+ ions are the cations and TFSI- ions comprise the anions. (c) Chemical structure of the PCP and OPE3 molecules.

ular junctions. A strong gating electric field, generated from the electrical double layer (EDL) of the ionic liquid,[170] is vertically applied to the graphene/SAM/gold junctions (Fig. 6.1). Due to the partial electrostatic transparency of graphene,[171] the applied electric field penetrates through the graphene layer and tunes the energy levels of the SAM relative to the Dirac point of the graphene, resulting in effective gate control and a significant conductance modulation in the molecular transistors.

This work is a collaborative work with an experimental group in University of California, Los Angeles (UCLA).

6.2 Modelling gold-SAM-graphene devices

The ground state Hamiltonian and optimized geometry of each molecule was obtained using the density functional theory (DFT) code SIESTA.[88] The local density approximation (LDA) exchange correlation functional was used along with double zeta polarized (DZP) basis sets and the norm conserving pseudo potentials. The real space grid is defined by a plane wave cutoff of 185 Ry. The geometry optimization was carried out to a force tolerance of 0.01 $eV/$Å. This process was

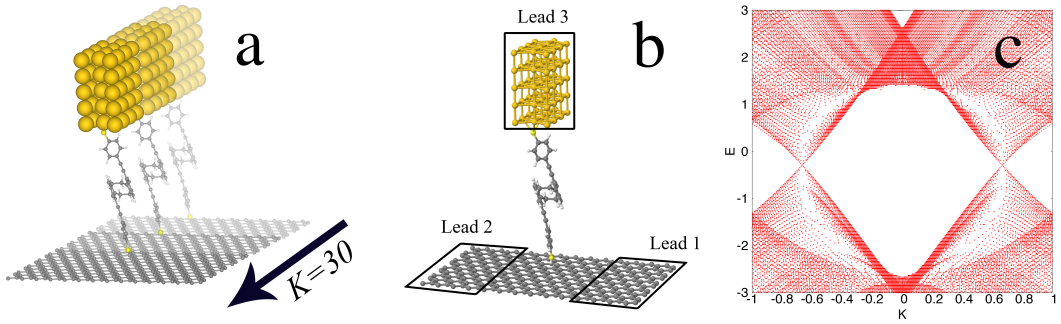

Figure 6.2: Schematic structures for theoretical calculation. (a) Simulating PCP SAM with gold and graphene electrodes. $K = 30$ k-points are employed in the direction indicated. (b) The structure for a single PCP junction. (c) Band structure of the graphene using 30 transverse k-points

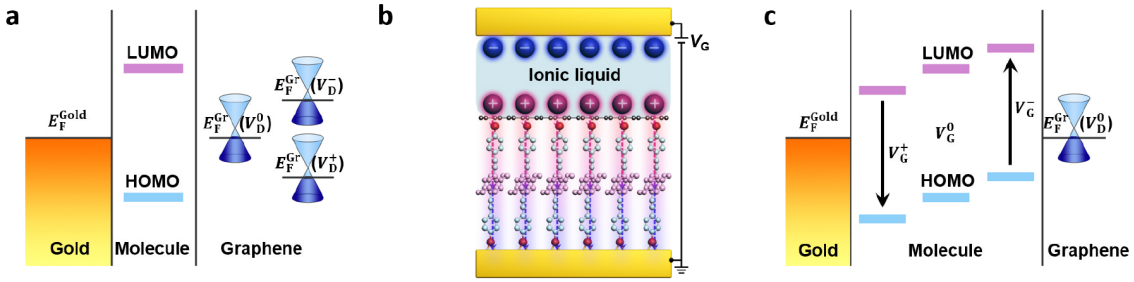

Figure 6.3: (a) Schematic band diagram of the device with changed V_D at graphene electrode. (b) Schematic illustration of the working device with electrical double layers. (c) Schematic band diagram of the device with changed V_G.

repeated for a unit cell with the molecule between gold and graphene electrodes where the optimized distance between graphene and the thiol anchor group was found to be 2.9 Å.

To model the periodicity in the graphene and interaction between the molecules in the SAM, the unit cell was repeated using a Bravais lattice with 30 k-points in the transverse direction shown in figure 6.2. This models a SAM where molecules are $2nm$ apart. The gold electrode is considered to be a nano-wire and not periodic. A mean field Hamiltonian and an overlap matrix was extracted from this converged calculation. Figure 6.3 shows the working mechanism for gate voltage (V_G) and bias voltage (V_D) dependency of the band structure of graphene and the energy levels of the molecule. Since the gold lead is earthed, the Fermi energy of gold (E_F^{Gold}) is not affected by the source-drain or gate voltage. However, the Fermi

energy of graphene is a function of the source-drain and gate voltages via the following equation

$$E_F^{Gr}(V_D, V_G) = E_F^{Gold} - \alpha V_D - \beta V_G, \tag{6.1}$$

where V_D and V_G are the source-drain and the gate voltages and α and β are the experimental lever arms, which could vary in each experiment. Similarly, applying a gate voltage can move the energy levels of the molecule up and down in energy (Eq. 6.2 and 6.3). (Fig. 6.3*c*)

$$\varepsilon^{HOMO}(V_G) = \varepsilon_m^{HOMO} - \gamma_G V_G; \tag{6.2}$$

$$\varepsilon^{LUMO}(V_G) = \varepsilon_m^{LUMO} - \gamma_G V_G. \tag{6.3}$$

The value for current is given by equation 6.4.

$$I(V_D, V_G) = \frac{2e}{\hbar} \int_{E_F^{Gold}}^{E_F^{Gr}(V_D,V_G)} T(E, V_D, V_G) dE, \tag{6.4}$$

where $T(E, V_D, V_G)$, is the transmission coefficient from lead 1 to lead 3 calculated using quantum transport code GOLLUM.[101] In what follows $\gamma_G = 1$. When comparing theory with experiment, eg. in figure 6.6, a lever arm of $\alpha = 0.44$ is employed.

6.3 Properties of the molecules

In contrast to the fully conjugated molecular chain in OPE3, a fundamental difference of PCP molecules is the presence of spatially separated aromatic rings linked by saturated methylene bridges in PCP. In this case, a current path mediated by π-π overlap between aromatic rings acts in parallel with current paths through the methylene bridges to create destructive QI features between the highest occupied molecular orbital (HOMO) and the HOMO-1, as shown in figure 6.4*b* and in the literature.[168] When combined with interruption of the conjugation in the PCP

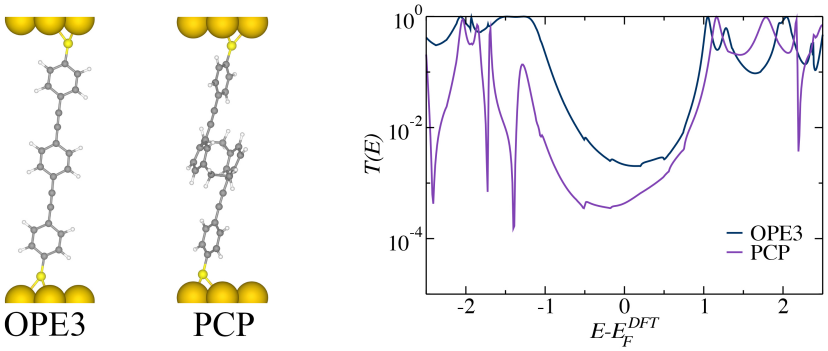

Figure 6.4: Charge transport in gold/molecule/gold junctions. (*a*) Schematic illustration of the PCP and OPE3 junctions. (*b*) Transmission functions $T(E)$ for PCP (purple) and OPE3 (blue).

molecule, this results in a lower transmission coefficient $T(E)$ for the PCP molecule compared with OPE3. In order to fully understand the origin of this difference, a comparison between the molecular orbitals of PCP and OPE3 is presented figure 6.5.[172]

Figure 6.5 shows that for both molecules the inter-orbital quantum interference between eg. the HOMO and LUMO is constructive, because their orbital products have opposite signs, as discussed in reference.[153] However the broken conjugation of the PCP, which can be regarded as a form of intra-orbital destructive QI between the left and right halves of the molecule, means that there is only a small electronic coupling between the left and right halves of the molecule. This results in the reduction of the conductance in PCP. It is worth mentioning that for OPE and PCP with gold-gold contact the calculated ratio of the conductance is $\frac{G_{OPE}}{G_{PCP}} = \frac{2.17\times10^{-3}}{4.34\times10^{-4}} = 5$, which is in agreement with the literature.[151,152]

6.4 Current and conductance

Figure 6.6*b* shows the calculated transmission coefficient through a gold-molecule-graphene junctions using PCP (purple) and OPE (orange) molecules. The ratio of the transmission coefficients for PCP and OPE at $E - E_F^{Gold}$ is $\frac{T_{OPE}(E_F^{Gold})}{T_{PCP}(E_F^{Gold})} \approx 135$,

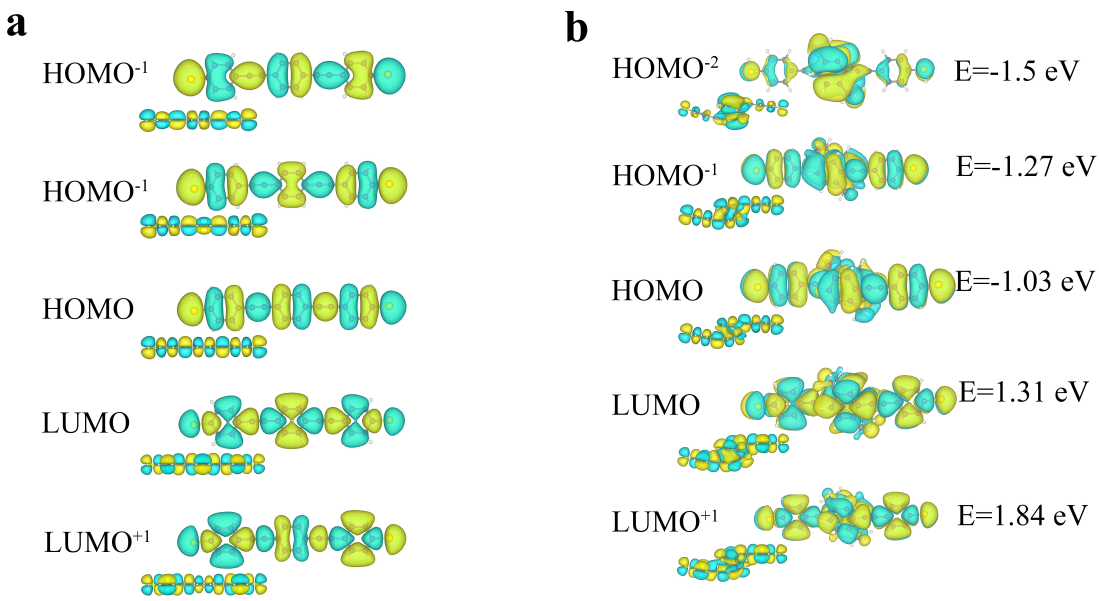

Figure 6.5: PCP and OPE3 molecular orbitals, (a) The Molecular orbitals for OPE3 (b) Molecular orbitals for PCP.

showing the same trend as the gold-molecule-gold calculation discussed in the previous section.

The experimental current density (J_D) vs. bias voltage V_D and the differential conductance (dJ/dV) vs. V_D are shown in figures 6.6c and 6.6d. The current density (J_D) for the PCP junction is considerably lower than that of the OPE3 junction, especially near zero bias, which is consistent with the transmission coefficient characteristics of the respective molecules discussed above. The minima in the dJ/dV curves are associated with the Dirac point of the graphene and their positions relative to the zero V_D indicates whether the graphene is p-doped or n-doped. In figure 6.6d, the Dirac point for OPE3 and PCP samples occurs at $-0.3V$ and $0V$ respectively. Indicating that the graphene is n-doped in the OPE3 sample and negligibly doped in PCP sample. For this reason, in what follows, when comparing our calculated $T(E)$ with experiments the band structure of the graphene is adjusted to place the Dirac point of the OPE3 system at $-0.3eV$ and for PCP system at $0eV$ resulting the dip in the transmission coefficients in figure 6.6b.

From the experimental results of figure 6.6d, the value of dJ/dV at zero bias for

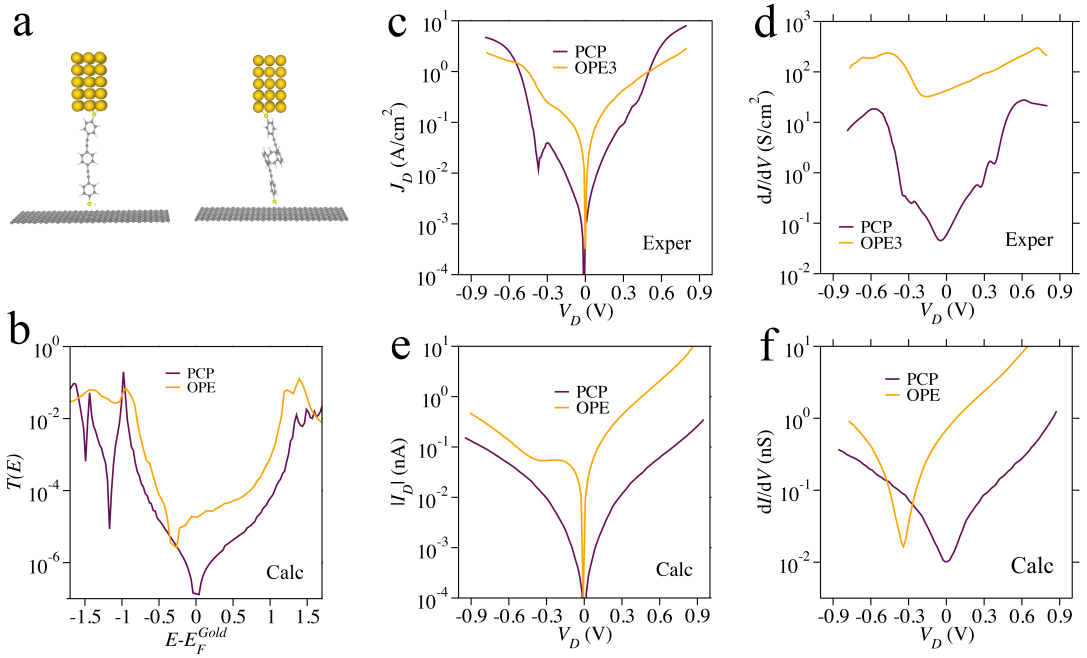

Figure 6.6: Charge transport in molecular junctions. (a) Schematic illustration of the PCP and OPE3 junctions. (b) Transmission functions $T(E)$ for PCP (purple) and OPE3 (orange). (c) Plots of experimental current density (J_D) versus bias voltage (V_D) for PCP and OPE3. (d) Differential conductance (dJ/dV) to V_D plots for experimental PCP and OPE3. (e) Theoretical current (I_D) to V_D plots for PCP and OPE3. (f) Theoretical differential conductance (dI/dV) to V_D plots for PCP and OPE3.

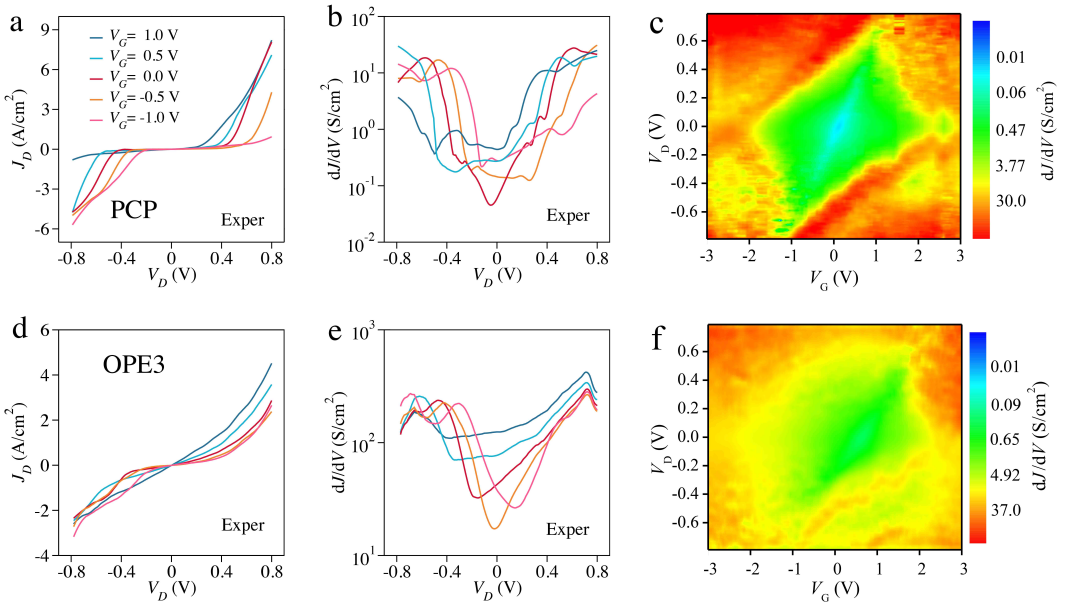

Figure 6.7: Experimental gating charge transport in molecular transistors. (a, d) Experimental J_D versus V_D characteristics for PCP and OPE with V_G changing from -1 to $1V$ with step of $0.5V$ (b, e) Experimental dJ/dV versus V_D characteristics for PCP and OPE (colour code for gate voltages are consistent with panel a)(c,f) Two-dimensional visualization of dJ/dV plotted versus V_G and V_D for PCP.

OPE3 is 71 times larger than that of PCP. This ratio is comparable with the value of 65 obtained from the calculated results of figure 6.6f. The conductance ratio of the gold-molecule-gold junction, is just about one tenth of junctions with gold-molecule-graphene contacts. This indicates that the conductance for molecule junctions with graphene electrode is more sensitive to the structure of molecules and their relative energy alignment.

Figures 6.7a and 6.7d show typical gate dependent $J_D - V_D$ characteristics measured at 200 K for PCP and OPE3 with gate voltage (V_G) changing from -1 to $1V$ with step of $0.5V$. With V_G changing from -1 to $1V$, J_D greatly increases with V_G for negative V_D, while J_D greatly decreases with V_G for positive V_D. On the other hand, the gate dependent J_D amplitude for OPE3 is evidently much smaller than that for PCP. This demonstrates the better gate control over the vertical PCP molecular transistors, compared with OPE3.

The conductance minima for both molecules move in a positive (negative) direction

along the V_D axis when the gate voltage is increased (decreased) (Figs. 6.7e). This feature is independent of the type of molecule and is a reflection of the gate-voltage dependence of the Dirac point of graphene. Figure 6.7c shows a two-dimensional visualization of dJ/dV plotted versus V_G and V_D for PCP. The oblique diamond-shaped low conductance region (green) indicates off-resonant transport, while the red-orange high conductance region outside the diamond is due to the conductive frontier molecular orbitals entering the bias window. Furthermore, a blue minimum conductance region appears at the centre of the diamond, which corresponds to the Dirac point of the graphene. For the OPE3 transistor (Fig. 6.7f), a similar oblique diamond-shaped low conductance region can also be observed. However, the relative conductance changing between centre low and outside high conductance regions for OPE3 is considerably smaller than that for PCP, which reflects the better gating tunability for PCP. This is in agreement with the calculated $T(E)$ for PCP and OPE3 (Fig. 6.6b), as the difference between off-resonant and resonant transport is more pronounced for PCP in comparison with OPE3. Furthermore, the V_G/V_D gradient for the edges of diamonds at the second and fourth quadrants is 0.2095 for OPE3, which is smaller than that of PCP with a value of 0.2493. This further demonstrates that the gate controllability for PCP is better than that for OPE3.

In our theoretical model, the gate voltage can move the energy levels of the graphene as well as the molecular energy levels (Eq. 6.1, 6.2 and 6.3). Therefore, the position of HOMO and LUMO relative to the Fermi energy of the gold varies with V_G as shown in figure 6.8. Similar to the bias voltage lever arm (α), we consider a gate voltage lever arm (β in equation 6.1).

The V_D and V_G dependent transmission coefficient $T(E, V_D, V_G)$ was calculated using quantum transport code GOLLUM,[101] and the current obtained from equation 6.4. The theoretical gate dependent $I_D - V_D$ characteristics for PCP (Fig. 6.9b) reveal that when V_G changes from -0.6 to $0.6V$, I_D greatly increases with V_G for negative V_D, while I_D decreases with V_G for positive V_D. A similar theoretical gate

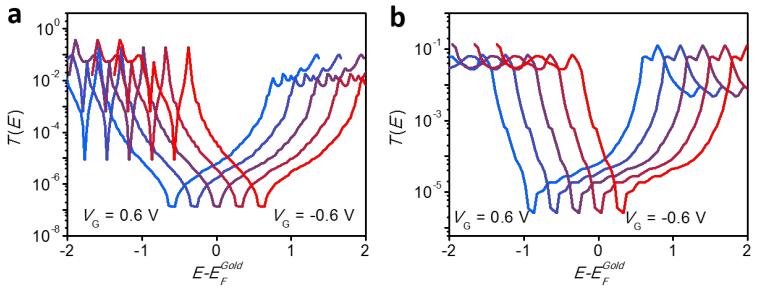

Figure 6.8: Gate dependent transmission for molecular transistors. Transmission functions $T(E)$ for PCP (a) and OPE3 (b) with V_G changing from -0.6 to $0.6V$ at step of $0.3V$.

dependent $I_D - V_D$ characteristic is also obtained for OPE3 (Fig. 6.9e), though the gate dependent change in I_D is smaller than that for PCP. Furthermore, from the gate dependent $dI/dV - V_D$ characteristics for PCP (Fig. 6.9c), it can be observed that the $dI/dV - V_D$ curve shifts in a positive direction with V_G changing from -0.6 to $0.6V$, especially for the lowest conductance points. For OPE3, a similar gate dependent $dI/dV - V_D$ curve is obtained, but with a relatively smaller amplitude (Fig. 6.9f), in qualitative agreement with the experimental results (Fig. 6.7).

In the experimental dJ/dV of OPE3 sample, we can see that the Dirac point of graphene moves up by $0.4V$ when gate voltage is increased by $1V$ (Fig. 6.7e). For a similar change in gate voltage, the Dirac point moves $0.5V$ in the PCP sample. Therefore, to compare our calculations with experiment, we choose $\beta = 0.4$. This assumption allows us to model the sensitivity of these devices to the change in V_G and V_D and yields agreement with our experiments. For example, a $1.2V$ change in the gate voltage of PCP device, moves the Dirac point of the graphene by $0.48V$ along the V_D axis (light blue and pink curves in figure 6.9c). Similar behaviour also occurs in OPE3 junctions (Fig. 6.9d); namely the orbital energies only vary with V_G, whereas the Dirac point and transmission minima are sensitive to both V_D and V_G.

Transfer characteristics, which monitor the current modulation by varying V_G at a fixed V_D, are widely used for evaluating the performance of transistors.[173] Experi-

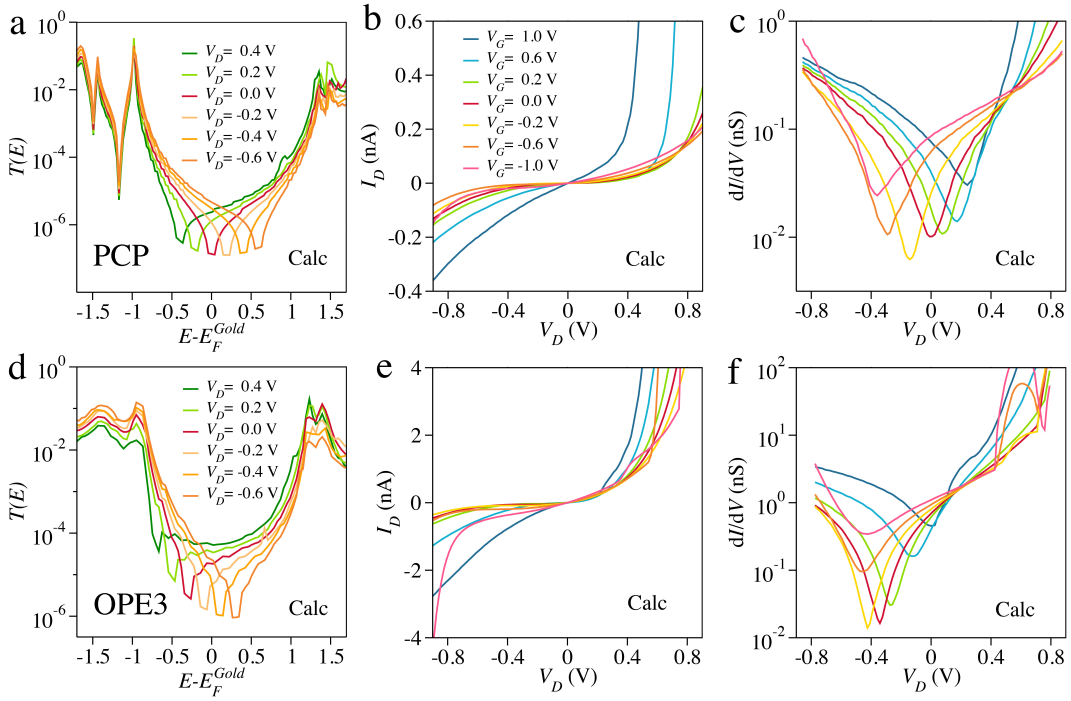

Figure 6.9: Theoretical gating charge transport in molecular transistors. (a, d) Transmission coefficient $T(E)$ versus for PCP and OPE3 junctions for $-0.4 < V_D < 0.4$ with steps of $0.2V$. (b, e) Gate dependent theoretical $I_D - V_D$ characteristics for PCP and OPE3. (c, f) Gate dependent theoretical $dI/dV - V_D$ for PCP and OPE3. V_G is varied from $-0.6, -0.3, 0.0, 0.3$ to $0.6V$ in b,e,c,f.

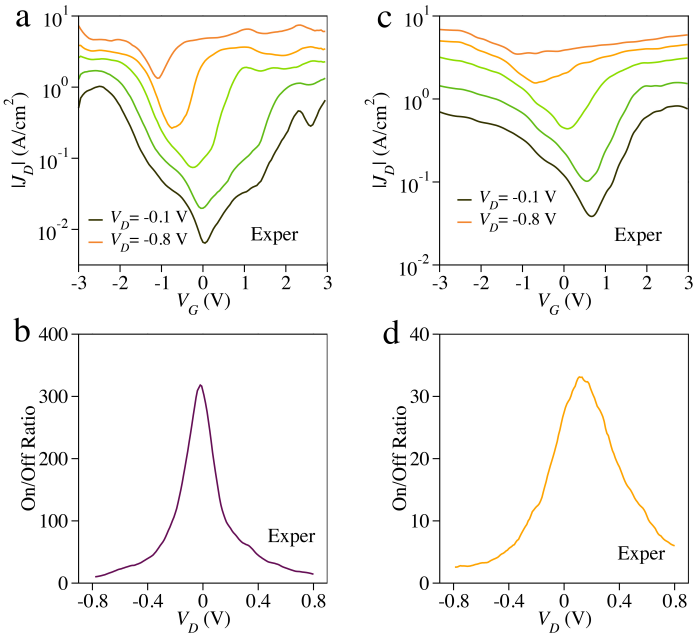

Figure 6.10: Experimental transfer characteristics for the vertical molecular transistors with (a) PCP and (c) OPE3. (b, d) On-off ratio for PCP and OPE devices.

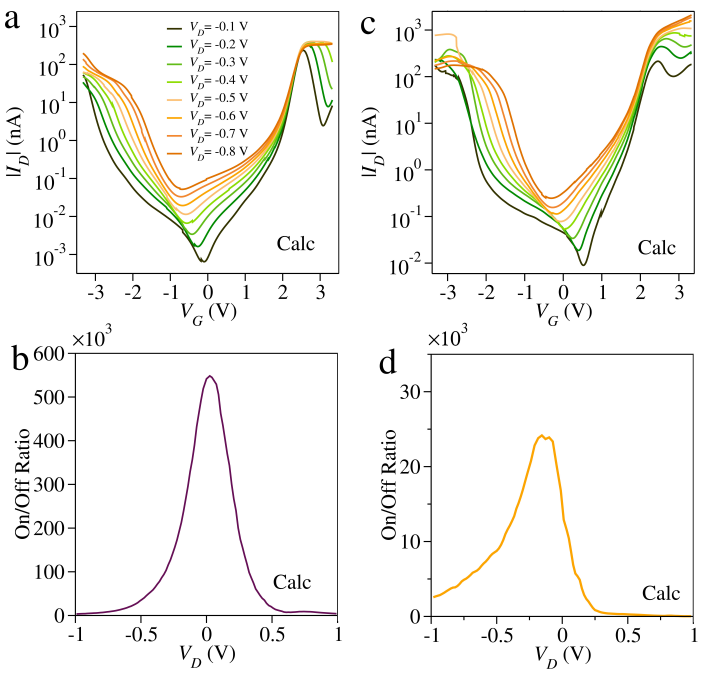

Figure 6.11: Theoretical transfer characteristics for the vertical molecular transistors with (a) PCP and (c) OPE3. (b, d) On-off ratio for PCP and OPE devices. V_D is varied from $-0.1, -0.2, -0.4, -0.6to - 0.8V$ in a and c.

mental transfer characteristics $(J_D - V_G)$ for PCP at $VD = -0.1, -0.2, -0.4, -0.6$ and $-0.8V$ are shown in figure 6.10a. It can be observed that the lowest current point at $V_D = -0.1V$ is near $V_G = 0V$. Increasing V_D from -0.1 to $-0.8V$, the lowest current point moves to more negative V_D. Such shifting of the lowest current point is due to variation on the Dirac point of the graphene electrode: with more negative V_D, increased negative V_G is needed to move the central transmission dip of the junction to the middle of the bias window. Furthermore, the on-off ratio, which corresponds to the ratio between the highest and lowest currents in a $J_D - V_G$ curve, decreases with increasing V_D. A highest on-off ratio of ~ 320 is achieved for PCP near $V_D = 0V$. (Fig 6.10b) The on-off ratio decreases with increasing V_D, which can be attributed to electron transmission occurring over a wider bias window, with the conductance less sensitive to gating-induced movement of molecular energy levels. Similar transfer characteristics (Fig. 6.10c) and a V_D dependent on-off ratio (Fig. 6.10d) also appears for OPE3, although with a peak on-off ratio value of ~ 4, which is only 10% of the PCP value. These behaviours cannot

be observed for the graphene device without SAMs layer, which is indicative of the unique field-effect behaviour for the vertical molecular transistors. The V_D dependent transfer characteristics for PCP and OPE3 were also investigated by theoretical simulations. From the theoretical transfer characteristics ($I_D - V_G$) for PCP (Fig. 6.11a) and OPE3 (Fig. 6.11c), as V_D changes from -0.1 to $-0.8V$, it can be observed that with increased negative V_D, on-off ratios decrease, and the lowest current points shift to the negative direction. In agreement with our measurements, the peak value of on-off ratio for PCP is about one order of magnitude higher than that of the OPE3 (Fig 6.11d).

6.5 Conclusion

In summary, we have demonstrated molecular transistors using vertical cross-plane graphene/SAM/gold heterostructures and ionic liquid gating. We show that charge transport across the vertical junction and transistor characteristics can be readily tailored by selecting molecules with or without destructive QI features (e.g. PCP vs. OPE3-based junctions). Importantly, we show that a graphene/PCP-SAM/gold junction can show a significance current modulation by an ionic liquid gate, with a maximum on-off ratio up to 330, which is about one order of magnitude higher than that for OPE3. This better gate behaviour for PCP is a direct consequence of the zero-bias conductance suppression induced by destructive QI. The designed vertical molecular transistors with large on-off ratio could form the basic electronic building blocks for future electronics and may offer a robust platform for exploring gate dependent quantum transport phenomena,[153,162,163] especially when the ionic liquid gate is further replaced by solid high-k gate.[173] Furthermore, such QI-driven vertical molecular transistors, with sensitive gating applied outside of top graphene electrode, can be further used for fabricating various functional devices, such chemical and biological sensors.[174,175] This work has stimulated another collaborative project with the experimental group in UCLA who performed

this study. This work studies the molecular magic-ratio of conductance in a self-assembled monolayer which is discussed in the next chapter.

Chapter 7

Self-assembled molecular-electronic films controlled by room-temperature quantum interference

If single-molecule, room-temperature, quantum interference (QI) effects could be translated into massively parallel arrays of molecules located between planar electrodes, then QI-controlled molecular transistors would become available as potential electronic building blocks for future integrated circuits and QI-based strategies for designing ultra-thin functional materials would become possible. Here, through a combined experimental and theoretical investigation, we demonstrate unequivocal signatures of room-temperature QI in vertical tunnelling transistors, formed from self-assembled monolayers (SAMs), with stable room-temperature switching operations. In contrast to artificial quantum dots, the electrical connectivity to the central cores of single molecules can be controlled to atomic accuracy through appropriate chemical synthesis. Consequently, it has been demonstrated that the electrical conductance of single molecules can be varied by orders of magnitude

in a deterministic manner, depending on their connectivity. Here, this signature of QI is translated into cross-plane graphene/SAM/gold molecular transistors formed from molecules with graphene-like anthanthrene cores. The conductances of vertical molecular junctions formed from anthanthrene-based molecules with two different connectivities differ by a factor of approximately 34, in agreement with theoretical predictions for their conductance ratio based on constructive QI effects within the core. By further controlling the molecule-electrode interface using different terminal groups, such QI effects can be enlarged, and the conductance ratio increased to 173. Field-effect control is achieved using an ionic liquid gate, whose strong vertical electric field penetrates through the graphene layer and tunes the energy levels of the SAMs. The resulting room-temperature on–off current ratio of the lowest-conductance SAMs can reach up to 306, about one order of magnitude higher than that of the highest-conductance SAMs. This demonstration of QI effects in gate-tunable SAMs represents a critical step towards functional ultra-thin-film devices for future molecular-scale electronics.

7.1 introduction

Single-molecule electronic junctions have been investigated intensively over the past decade, not only as stepping stones towards functional devices/circuits made from collections of molecules, but also because their room-temperature electrical conductance is controlled by quantum interference (QI).[155,176–184] Figure 7.1*a* illustrates an example of a room-temperature QI effect, in a graphene-like (anthanthrene) molecular core, when electrical current is injected and collected via the green arrows, or alternatively via the red arrows. If the core behaved like a classical resistor network, then the electrical conductance for these two connectivities would be approximately equal. In contrast, theory predicts and experiment confirms[172,185,186] that the room temperature, single-molecule, low-bias electrical conductance G_1 for the green $(7, 2')$ connectivity is approximately two orders of

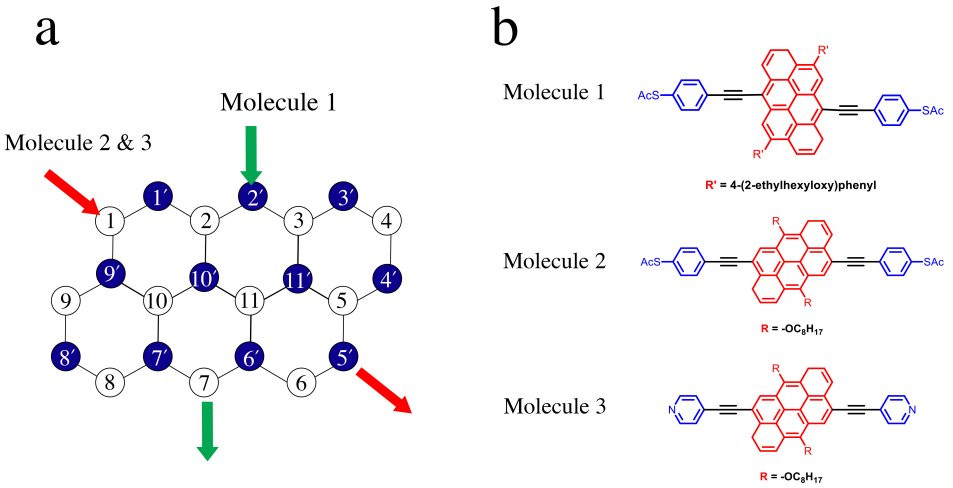

Figure 7.1: Structures of the studied molecules. (a) A sketch of an anthanthrene core with connectivities $7, 2'$ and $1, 5'$ (the numbering system is chosen for mathematical convenience and does not coincide with standard chemical notation). (b) Chemical realisations of molecules with anthanthrene cores. 1 corresponds to the $7, 2'$ connectivity, while 2 and 3 correspond to the $1, 5'$ connectivity. $R' = 4 - (2 - ethylhexyloxy)phenyl, R = -OC_8H_{17}$.

magnitude larger than the conductance G_2 of the red $(1, 5')$ connectivity. This is a clear signature of different degrees of constructive QI at room-temperature. Figure 7.2 is a demonstrattion of this principle for a tight-binding model of the core shown in figure 7.1a. The chemical realisation of the green connectivity is molecule 1 of figure 5.1a, in which the terminal groups attached to electrodes inject a current into the anthanthrene core via triple bonds. Similarly, molecules 2 and 3 are realisations of the red connectivity, with different terminal groups, which can further control interfacial coupling and energy level alignment between molecule and electrode.[187,188] Our aim is to create a SAM-based molecular tunnelling transistor from these molecules and to demonstrate that these single-molecule signatures of QI can be realised in self-assembled monolayer-based devices. We indeed find that the electrical conductance of the SAM formed from 1 is significantly higher than that of the SAM formed from 2 or 3. Furthermore, by applying an external gate, we are able to assess their different field-effect performances.

In contrast to molecular tunnelling transistors fabricated by placing a solid back gate[164] or electrochemical gate[165,189] to the side of molecular junctions, which can

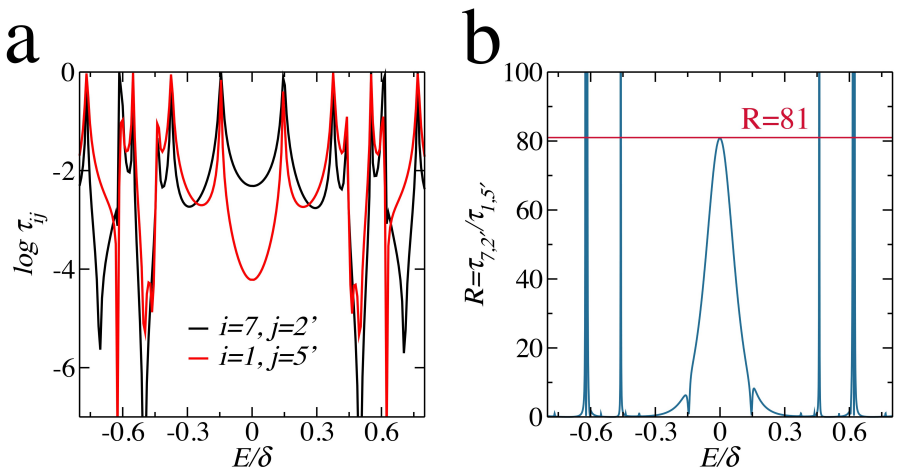

Figure 7.2: (a) Transmission coefficient for the connectivities in figure 7.1a for a tight-binding model. (b) The ratio of the transmission coefficients. The conductance ratio for the connectivities discussed in figure 7.1a is 81.[185]

typically only operate stably at cryogenic temperatures, here we utilise a vertical molecular tunnelling transistor with stable room-temperature operation, based on a gate modulated graphene/SAM/gold cross-plane vertical heterostructure.[166,167] The binding geometry of the molecules in the SAM are fixed[169] by the terminal anchor groups to the gold electrode and the inter molecular interactions in the SAM, which promotes stable charge transport through the molecular junctions. A strong gating electric field, generated from the electrical double layer (EDL) of ionic liquid,[170] is vertically applied to the graphene/SAM/gold junctions (Fig. 7.3a). Due to the partial electrostatic transparency of graphene,[171] the applied electric field penetrates through the graphene layer and tunes the energy levels of the SAM relative to the Fermi energy of gold (E_F^{Gold}), resulting in effective gate control and a significant conductance modulation in the molecular transistors.

7.2 Results

In the absence of electrically active side chains, the ratio $\frac{G_1}{G_2}$ of the low-bias, single-molecule conductances of 1 and 2 are predicted by a 'magic number' table,[185] which yields $\frac{G_1}{G_2} = 81$ (Fig. 7.2). This simple 'magic ratio theory' illustrates how connec-

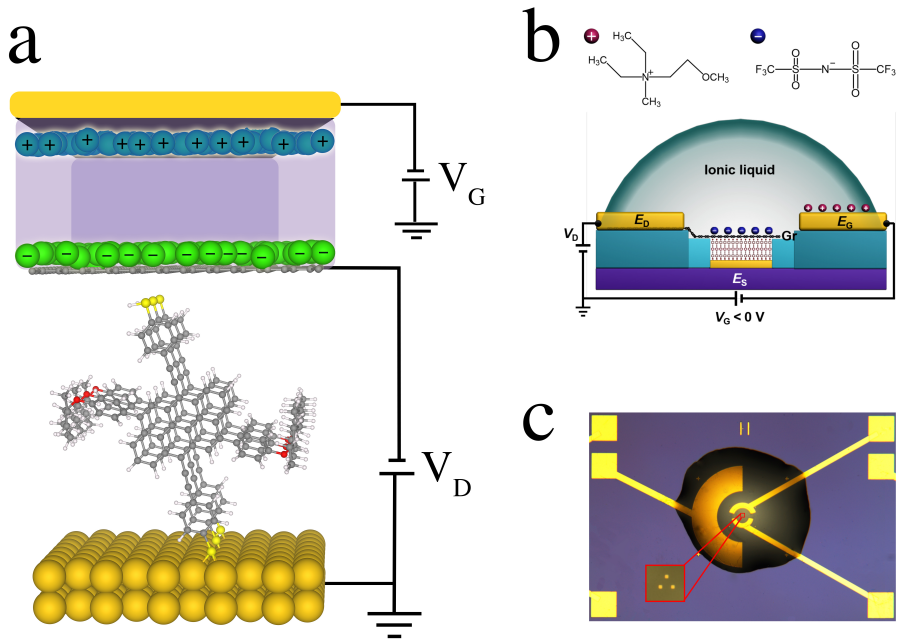

Figure 7.3: Schematic illustration of the vertical molecular tunnelling transistor. (*a*, *b*) Schematic illustration for the setup of the device with vertical ionic liquid gate through graphene layer to SAMs and molecular structures for DEME+ cation and TFSI- anion. (*c*) Optical photograph of the device with ionic liquid gate.

tivity alone contributes to conductance ratios, without including chemical effects or coulomb interactions. When the latter are included, recent studies indicate that the qualitative trend in the ratio is preserved (i.e., that $\frac{G_1}{G_2} \gg 1$), but the precise value should be calculated using ab initio methods. Our aim is to determine if this signature of QI is preserved or modified in a SAM, and how it depends on intermolecular interactions and the interplay between the molecular level and the density of states of graphene.

Figure 7.4*b* shows the computed transmission coefficient for electrons passing through all three junctions. Previous comparison between experiment and theory revealed that electron transport through anthanthrene based molecules takes place near the middle of the energy gap between the highest occupied molecular orbital (HOMO) and the lowest unoccupied molecular orbital (LUMO).[185] Therefore in the calculations presented below, the Fermi energy of the gold is located near the middle of the HOMO-LUMO gap and all energy axes are plotted with respect to the mid-gap energy $E_F^{mid-gap} = E_F^{Gold}$. The computed ratio of their

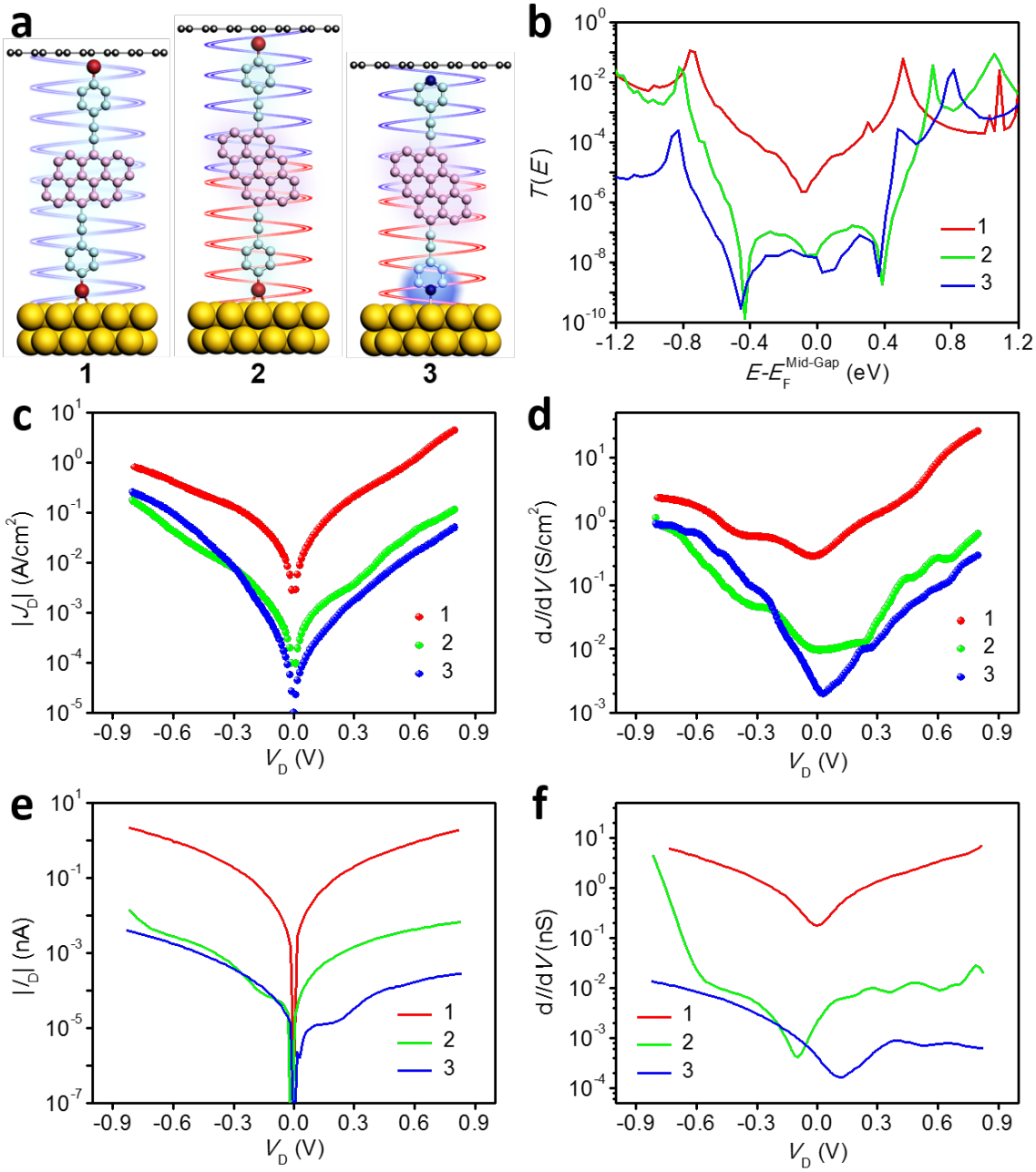

Figure 7.4: Charge transport in molecular junctions. (a) Schematic illustration of molecular junction 1, 2 and 3, where the side chains of molecules are hidden. (b) Transmission functions $T(E)$ for 1 (red), 2 (green) and 3 (blue). (c) Plots of experimental current density (J_D) vs. bias voltage (V_D) for 1, 2 and 3. (d) Experimental differential conductance (dJ/dV) vs. V_D. (e) Theoretical current (I_D) vs. V_D. (f) Theoretical differential conductance (dI/dV) vs. V_D.

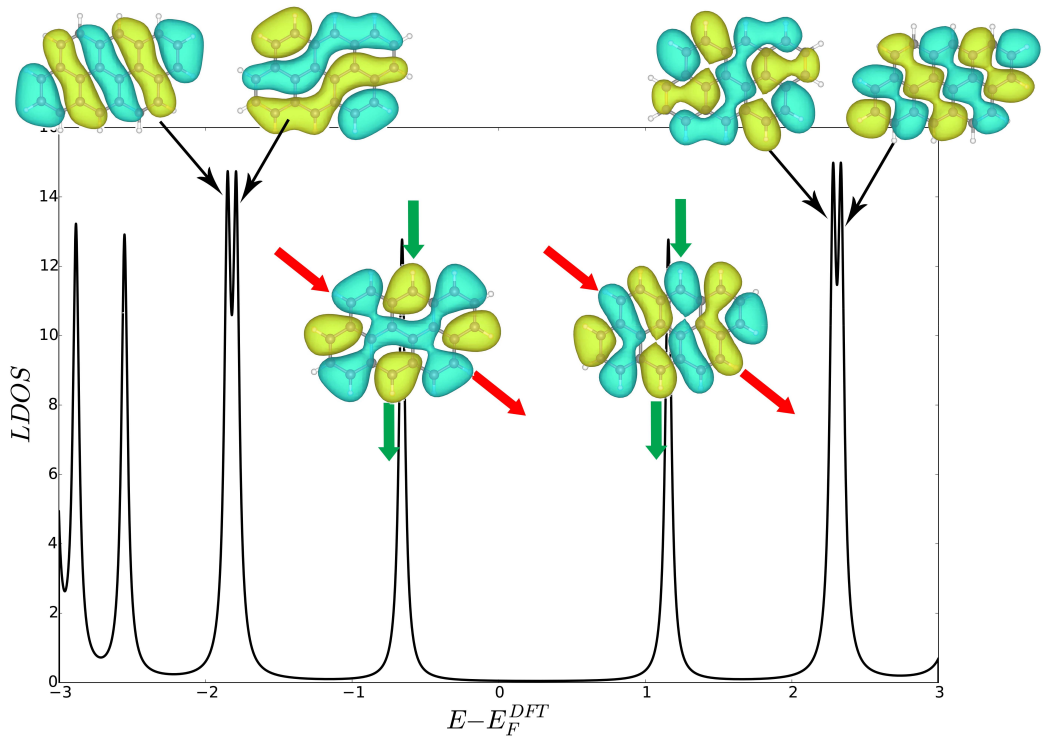

Figure 7.5: The local density of states for the anthanthrene core of the molecule 1, 2 and 3 of Figure 1. The wavefunction of the HOMO and the LUMO energy levels of the core suggests that neither of the connectivities suggested in Figure 1 lead to inter-orbital destructive quantum interference.[22]

transmission coefficients in graphene-molecule-gold junctions for molecule 2 and 1 at $E = E_F^{Gold}$ is 116. It should be emphasised that both molecules exhibit constructive QI near their gap centres and the conductance ratio arises from the different degrees of constructive QI associated with the different connectivities. Figure 7.5 illustrates that the constructive nature of the QI is also reflected in the molecular orbitals of molecule 2 and 1. When the terminal groups of molecules are changed from thiol to pyridine, the transmission coefficient in the junctions for molecule 3 at $E = E_F^{Gold}$ is reduced to 1/7 of that for molecule 2. This indicates that the QI effect acts in conjunction with the higher pyridine-gold interface resistance to determine charge transport in the junctions.

The experimental current density (J_D) vs. bias voltage (V_D) and the differential conductance (dJ/dV) vs. V_D are shown in Fig. 7.4*c*,*d*. As predicted by magic ratio theory, the current density (J_D) and for the $1, 5'$ junction formed from molecule 2 is considerably lower than that of the $7, 2'$ junction formed from molecule 1, especially

near zero bias, which is consistent with the transmission coefficient characteristics of the respective molecules discussed above and theoretical results (Fig. 7.4*e*). With pyridine terminal groups for the $1, 5'$ junction, the J_D for molecule 3 is further reduced as forecasted in transmission functions. The minima in the dJ/dV curves are associated with the Dirac point of the graphene and their position relative to the zero V_D indicates whether the graphene is p-doped or n-doped. In Fig. 7.4*d*, the Dirac point for molecule 1 and 2 samples occurs at -0.03 V and -0.05 V respectively, indicating that the graphene is slightly n-doped in the presence of the thiol-terminated SAMs. However, for sample 3 this minimum appears at 0.01V, suggesting p-doped graphene in the case of a pyridine anchor group. For this reason, in what follows, when comparing our calculated $T(E)$ with experiments, the band structure of the graphene is adjusted to place the Dirac point of each system at the experimental value.

For the experimental dJ/dV results (Fig. 7.4*d*), the value of dJ/dV at zero bias for molecule 1 is 29 times larger than that of molecule 2. This ratio is comparable with the value of 84 obtained from the theoretical results of Fig. 7.4*f*. It is also worth mentioning that for molecule 2 and 1 junctions with gold-molecule-gold contacts (Fig. 7.7), the conductance ratio at zero bias is $\frac{G_1}{G_2} = 203$, which indicates that the interfacial contacts are playing a role in determining the conductance ratio. After changing the terminal groups from thiol to pyridine to control the interfacial contacts, the zero-bias differential conductance for molecule 3 is 1/5 of that for molecule 2 which is comparable with the calculated value of 1/8.7 (Fig. 7.4). To probe the field effect performances of these molecular junctions, DEME-TFSI ionic liquid was used for gating, which has a large electrochemical window, a high ionic conductivity, and a low freezing temperature for ion migration. When a gate voltage (V_G) is applied to the gate electrode, a Helmholtz electrical double layer (EDL) self-organizing on the outside surface of graphene layer (Fig. 7.3*a*,*b*) generates a strong electric field up to 10 MV/cm to the molecular junction.[170] The gate performances of three transistors were measured at room temperature (298

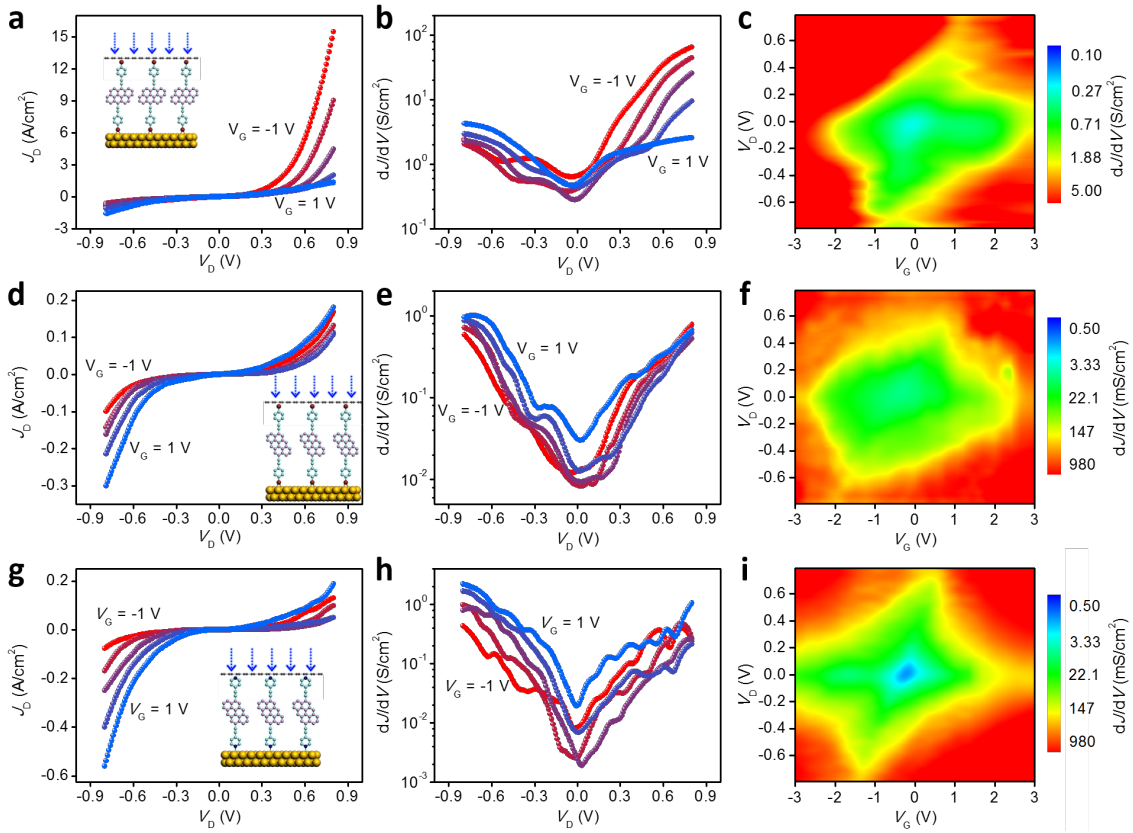

Figure 7.6: Gating charge transport in molecular transistors. (a, d, g) J_D vs. V_D characteristics for 1 (a), 2 (d), and 3 (g) with gate voltage (V_G) changing from -1 to $1V$ with step of $0.5V$. Insets show schematics of the 1, 2 and 3 transistors with applied vertical electric field. (b, e, h) dJ/dV vs. V_D characteristics for 1 (b), 2 (e), and 3 (h) with V_G changing from -1 to $1V$ with step of $0.5V$. (c, f, i) Two-dimensional visualization of dJ/dV vs. V_G and V_D for 1 (c), 2 (f), and 3 (i).

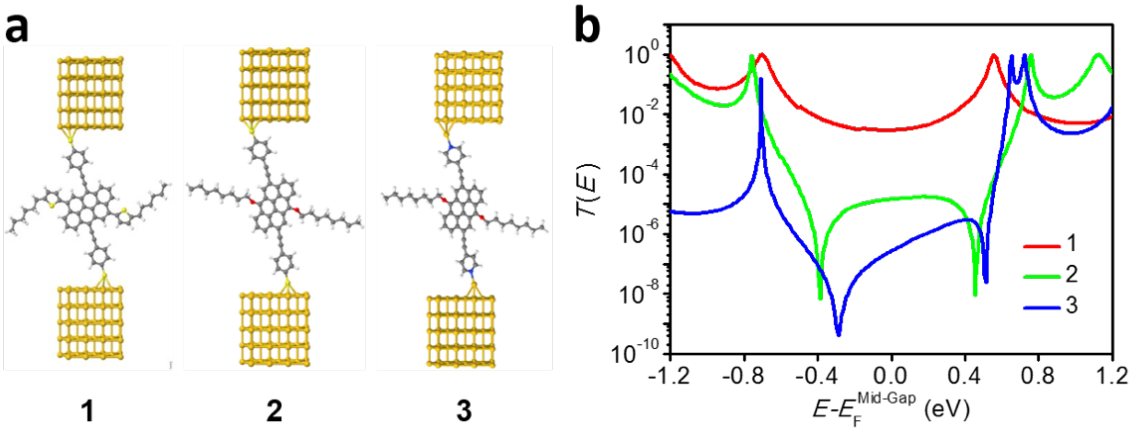

Figure 7.7: (a) The structure of gold/molecule/gold junction 1, 2 and 3 for simulation. (b) Transmission coefficient for gold/molecule/gold junctions for molecule 1(red), 2 (green) and 3 (blue). At $E - E_F^{mid-gap} = 0eV$, the ratio of $\frac{T_1}{T_2} = 203$, $\frac{T_2}{T_3} = 52$.

K). Figures 7.6*a*, *d* and *g* show typical gate dependent $J_D - V_D$ characteristics for molecules 1, 2 and 3, respectively. Changing V_G from -1 to $1V$, greatly increases J_D for negative V_D, while J_D greatly decreases with V_G for positive V_D, clearly demonstrating effective field-effect modulation of the molecular junctions. Typical gate dependent $dJ/dV - V_D$ characteristics for molecules 1, 2 and 3 are shown in figure 7.6*b*, *e* and *h*. When the gate voltage is increased from -1 to $1V$, $dJ/dV - V_D$ curves for all three junctions move in a positive direction along the V_D axis, which reflects the gate-voltage dependent movement of the molecular orbital energy levels. Figures 7.6*c*, *f* and *i* respectively show two-dimensional visualizations of dJ/dV plotted versus V_G and V_D for molecules 1, 2 and 3. The oblique diamond-shaped low conductance region (green and blue) can be observed for all three transistors, which indicate off-resonant transport through HOMO-LUMO gap. While the red-orange high conductance region outside the diamond is owing to the conductive frontier molecular orbitals coming into the bias window. The relative conductance changing between center low conductance and outside high conductance regions for molecule 1 is considerably smaller than that for molecule 2, which indicates the better gating tunability for molecule 1. This agrees with the calculated $T(E)$ for molecules 1 and 2 (Fig. 7.4*b*), as the difference between off-resonant and resonant transport is more pronounced for molecule 2 in comparison with molecule 1. For comparison between molecules 3 and 2, a blue lowest conductance region appears at the center of the diamond for molecule 3 (Fig. 7.6*f*), corresponding to the calculated lowest off-resonant transmission of 3 (Fig. 7.4*b*), which further improves the gating tunability of molecule 3.

The conductance minima for molecule 1 are sharp features for all values of the applied gate voltage. However, in the case of molecule 2 (Fig. 7.6*e*) the minimum at $V_G = 0V$ is a broader feature, which splits into two sharper minima when the gate voltage is increased to $0.5V$ and $1.0V$. This is in agreement with the calculated $T(E)$ for molecules 1 and 2 (Fig. 7.4*b*). While T_1 has no features between the HOMO and LUMO apart from the Dirac point, T_2 has two sharp

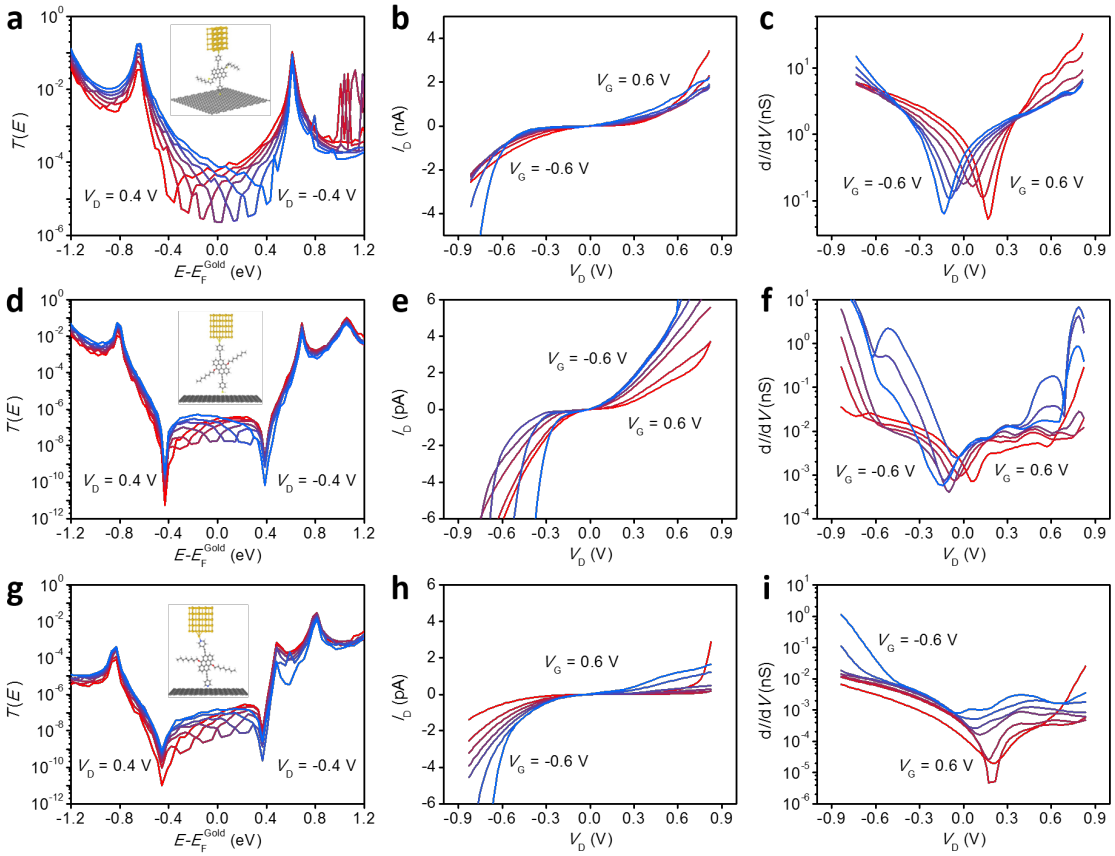

Figure 7.8: Working mechanism for vertical molecular transistors. Transmission coefficient $T(E)$ vs. $E - E_F^{mid-gap}$ for molecular junction 1 (a), 2 (d) and 3 (g) for $-0.4 < V_D < 0.4$ with steps of $0.13V$ (red for $V_D = 0.4V$). Insets show the structures of molecular junctions for simulation. Gate dependent theoretical $I_D - V_D$ characteristics for 1 (b), 2 (e) and 3 (h) for $-0.6 < V_G < 0.6$ with steps of $0.2V$ (red for $V_G = 0.6V$). Gate dependent theoretical $dI/dV - V_D$ characteristics for 1 (c), 2 (f) and 3 (i) for $-0.6 < V_G < 0.6$ with steps of $0.2V$ (red for $V_G = 0.6V$).

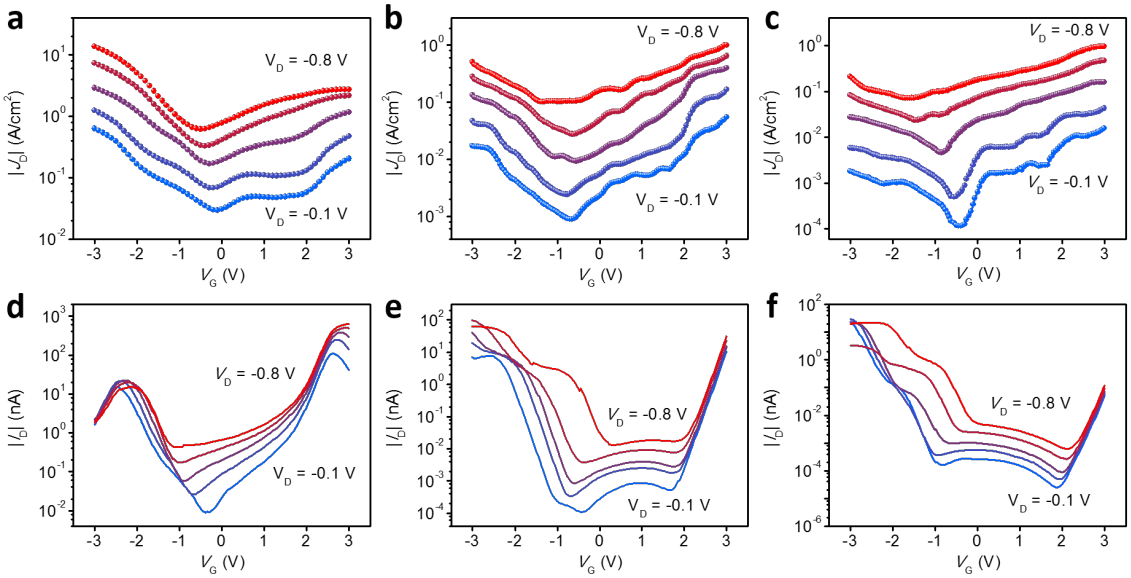

Figure 7.9: Transfer characteristics for the vertical molecular transistors. $(a-c)$ Experimental transfer characteristics for 1 (a), 2 (b) and 3 (c). $(d-f)$ Theoretical transfer characteristics for 1 (d), 2 (e) and 3 (f). V_D is varied from -0.1, -0.2, -0.4, -0.6 to -0.8 V in $(a-f)$.

anti-resonances. For $V_G = 0$ none of the anti-resonances are close enough to the Fermi energy to appear in the dI/dV curves. By increasing the gate voltage, and hence the relative position of the anti-resonances to the Fermi energy, one of the anti-resonances is close enough to the Fermi-energy to be captured in the dI/dV. The lever arms in the theoretical model, which give the best agreement between theory and experiment, are $\alpha = 0.4$, $\gamma = 0.25$ and $\beta = 0.25$.

Figures 7.8a, d and g show the V_D dependence of $T(E)$ versus for molecules 1, 2 and 3. It is assumed that the energies of the molecular levels relative to are independent of V_D and that positive (negative) bias voltage decreases (increases) the Dirac point relative to E_F^{Gold}. The current is computed using equation 6.4 in previous chapter by evaluating individual transmission coefficients $T(E, V_D, V_G)$ at every V_D value and computing the associated current. The dI/dV curves are then obtained by differentiating the current with respect to V_D.

The V_D and V_G dependent transmission coefficient $T(E, V_D, V_G)$ was calculated using the quantum transport code the Gollum[101] and the current obtained from equation 6.4. The theoretical gate-dependent $I_D - V_D$ characteristics for molecule

2 (Fig. 7.8*e*) reveal that when V_G changes from -0.6 to $0.6V$, I_D greatly increases with V_G for negative V_D, while I_D decreases with V_G for positive V_D. A similar theoretical gate dependent $I_D - V_D$ characteristic is also obtained for molecule 1 (Fig. 7.8*b*), though the gate dependent change in I_D is smaller than that for molecule 2. Furthermore, from the gate dependent $dI/dV - V_D$ characteristics for molecule 2 (Fig. 7.8*f*), it can be observed that the $dI/dV - V_D$ curve shifts in a positive direction with V_G changing from -0.6 to 0.6 V, especially for the lowest conductance points. For molecule 1, a similar gate dependent $dI/dV - V_D$ curve is obtained, but with relatively smaller amplitude (Fig. 7.8*c*), in qualitative agreement with the experimental results (Fig. 7.6). For molecule 3, gate dependent $I_D - V_D$ (Fig. 7.8*h*) and $dI/dV - V_D$ (Fig. 7.8*i*) curve with relatively larger amplitude can be observed, which are similar with molecule 2. Moreover, lowest conductance minima appear in gate dependent $dI/dV - V_D$ curves (Fig. 7.8*i*), which is consistent with experimental lowest conductance region (Fig. 7.6*i*). Transfer characteristics, monitoring the current modulation with varying V_G at a fixed V_D, are widely used for assessing the transistor performance.[190] The V_D dependent transfer characteristics for molecules 1, 2 and 3 were investigated by both experiment and theoretical simulations. Experimental transfer characteristics ($J_D - V_G$) for 1 at $V_D = -0.1, -0.2, -0.4, -0.6$ and $-0.8V$ are shown in Fig. 7.9*a*. It can be observed that the lowest current point at $V_D = -0.1V$ is near $V_G = 0V$; and with V_D changing from -0.1 to $-0.8V$, the lowest current point shifts to more negative V_D. As the Dirac point of the graphene electrode dominates the conductance minima for molecule 1 (Fig. 7.8*a*), such shifting of the lowest current point is due to the variation of the Dirac point of the graphene electrode. Specifically, with more negative V_D, an increased negative V_G is needed to move the central transmission dip of the junction to the middle of the bias window. This experimental phenomenon is also confirmed by theoretical transfer characteristics ($I_D - V_G$) for 1 (Fig. 7.9*d*), as V_D changes from -0.1 to $-0.8V$. The on-off ratio, which corresponds to the ratio between the highest and lowest currents in a $J_D - V_G$ curve, is up to 26 for

molecule 1 near $V_D = 0V$. In contrast, the highest on-off ratio for molecule 2 (Fig. 7.9*b*) is increased to 105 near $V_D = 0V$, which is about 4 times of molecule 1. Furthermore, two conductance valleys can be obviously observed from $J_D - V_G$ curves, especially at $V_D = -0.1V$, which is due to the QI-induced conductance minima for molecule 2. This is clear from the theoretical transfer characteristics ($I_D - V_G$) of molecule 2 (Fig. 7.9*e*), where two conductance valleys appear and become mixed together with V_D changing from -0.1 to $-0.8V$. Furthermore, the on-off ratio decreases with increasing $|V_D|$, which can be attributed to electron transmission occurring over a wider bias window, with the conductance being less sensitive to gating-induced movement of molecular energy levels. Similar transfer characteristics appear for molecule 3 (Fig. 7.9*c*), and the highest on-off ratio is further increased to 306 near $V_D = 0V$, which is about 2.9 times of molecule 2 and 12.0 times of 1. This is consistent with the theoretical transfer characteristics ($I_D - V_G$) for 3 (Fig. 7.9*c*), because two conductance valleys appear, and on-off ratios decrease as V_D changes from -0.1 to $-0.8V$.

7.3 Conclusion

In summary, we have demonstrated that unequivocal signatures of single-molecule room-temperature QI can be translated into self-assembled molecular films. Furthermore anthanthrene-based molecular transistors, formed from vertical cross-plane graphene/SAM/gold heterostructures and ionic liquid gating, are shown to exhibit stable room-temperature switching operations. With two different connectivities to the anthanthrene core, QI effects lead to a conductances ratio of approximately 34 for molecular junctions 1 and 2, which can be further enlarged to 173 for junction 3 by controlling the molecule-electrode interface with different terminal groups. Importantly, junction 3 can show a significance current modulation by an ionic liquid gate, with a maximum on–off ratio up to 306, which is about one order of magnitude higher than that for 1. This enhanced gate behaviour for

3 is a direct consequence of the zero-bias conductance suppression induced by QI, combined with a higher interfacial resistance. The designed QI-controlled molecular transistors with large on-off ratio are potential electronic building blocks for future integrated circuits and functional ultra-thin film materials.

Chapter 8

Conclusion

In this thesis we employed the well-known DFT to get insight into the electronic structure of various molecular devices. Furthermore, we used a combination of Landauer approach and equilibrium Green's function theory to study electron and phonon transport through molecular junctions. These methods are discussed in chapter 2 at length. Using the named methods, we introduced powerful molecular design techniques which can potentially improve the efficiency of thermoelectric devices.

In the third chapter we introduced a powerful design technique to suppress unwanted phonon transport through single molecule. This method suggests that designing the appropriate side branches can lead to suppression in the transmission of phonons the frequency of which happens to resonate with the normal frequency of the branches. This design method allows us to suppress phonon transport in the desirable range of frequencies. The use of this strategy in designing single molecules can have significant impact on the efficiency of self-assembled monolayers in conversion of heat to electricity. Adaptation of this design strategy in experiments can also lead to the recognition of phononic quantum interference in single molecules.

In chapter 4 we showed that chemical modification of thiophene chains by addition

of ethylenedioxy group to the thiophene rings can enhance electronic conductance, Seebeck coefficient and the figure of merit. We also showed that this addition suppresses phonon transport since the added group act as side groups introduced in chapter 3. This work can be expanded by investigating other dopant with the aim of enhancing the ZT further and make synthesis of these molecules simpler.

In chapter 5 we discussed modelling of self assembled monolayer (SAM) of molecules placed between gold and graphene electrodes. We showed that a simple analytical model can capture the generic features in the dI/dV characteristics of these devices arising from the HOMO/LUMO dominated transport and doping of the graphene electrodes. Furthermore, we performed more realistic calculations using DFT and arrived at a close agreement with the experiments done on the same devices. This work provides a great experimental and theoretical platform for future investigation of various molecules in Gr/SAM/Au devices. It is essential to expand this work and investigate room-temperature quantum interference in such devices in future. This could be done by comparing the conductance of devices containing molecules whose conductance differ only due to quantum interference features. This will allow us to use molecular design for controlling the properties of SAM devices. Furthermore, studying the presence of dopant which can potentially enhance the ZT of these devices is one of the next natural steps. Phonon transmission through these devices should be investigated fully in the future with the consideration of new molecular design strategies similar to chapter 1 of this work.

In chapter 6 we have discussed modelling of gates SAM devices. We utilize two molecules one with destructive QI features and one without on on single molecule level. We then demonstrate that the destructive QI survives in a SAM device at room temperature. We prove our results by comparing the dI/dV ratios for two molecules obtained by experiment and theory and presenting a good agreement.

In chapter 7 we compare the conductance of SAM devices made of molecules

with various degrees of constructive QI through changing the connectivity of the anchoring groups the graphene-like molecular core (also known as 'magic-ratio' rule). Comparing theory and experiment, we show that the ratio of conductance of SAM devices made of these molecules is similar to that of single molecular junctions.

Bibliography

[1] William B. Chang, Cheng-Kang Mai, Michele Kotiuga, Jeffrey B. Neaton, Guillermo C. Bazan, and Rachel A. Segalman. Controlling the thermoelectric properties of thiophene-derived single-molecule junctions. *Chemistry of Materials*, 26(24):7229–7235, 2014.

[2] Brian Capozzi, Emma J. Dell, Timothy C. Berkelbach, David R. Reichman, Latha Venkataraman, and Luis M. Campos. Length-dependent conductance of oligothiophenes. *Journal of the American Chemical Society*, 136(29):10486–10492, 2014.

[3] Yan Geng, Sara Sangtarash, Cancan Huang, Hatef Sadeghi, Yongchun Fu, Wenjing Hong, Thomas Wandlowski, Silvio Decurtins, Colin J. Lambert, and Shi-Xia Liu. Magic ratios for connectivity-driven electrical conductance of graphene-like molecules. *Journal of the American Chemical Society*, 137(13):4469–4476, 2015. PMID: 25781036.

[4] C. J. Lambert. Basic concepts of quantum interference and electron transport in single-molecule electronics. *Chem. Soc. Rev.*, 44:875–888, 2015.

[5] Alexandre R. Rocha, Víctor M. García-suárez, Steve W. Bailey, Colin J. Lambert, Jaime Ferrer, and Stefano Sanvito. Towards molecular spintronics. *Nature Materials*, 4:335, Mar 2005.

[6] Stefano Sanvito, Young-Kyun Kwon, David Tománek, and Colin J. Lambert. Fractional quantum conductance in carbon nanotubes. *Phys. Rev. Lett.*, 84:1974–1977, Feb 2000.

[7] Laith Algharagholy, Thomas Pope, Qusiy Al-Galiby, Hatef Sadeghi, Steve W. D. Bailey, and Colin J. Lambert. Sensing single molecules with carbon-boron-nitride nanotubes. *J. Mater. Chem. C*, 3:10273–10276, 2015.

[8] Arieh Aviram and Mark A. Ratner. Molecular rectifiers. *Chemical Physics Letters*, 29(2):277 – 283, 1974.

[9] G. Binnig and H. Rohrer. Scanning tunneling microscopy. *Helvetica Physica Acta*, 55:726–735, 1982.

[10] G. Binnig, C. F. Quate, and Ch. Gerber. Atomic force microscope. *Phys. Rev. Lett.*, 56:930–933, Mar 1986.

[11] R. Martel, T. Schmidt, H. R. Shea, T. Hertel, and Ph. Avouris. Single- and multi-wall carbon nanotube field-effect transistors. *Applied Physics Letters*, 73(17):2447–2449, 1998.

[12] H. E. Katz and Z. Bao. The physical chemistry of organic field-effect transistors. *The Journal of Physical Chemistry B*, 104(4):671–678, 2000.

[13] A. DeHon. Array-based architecture for fet-based, nanoscale electronics. *IEEE Transactions on Nanotechnology*, 2(1):23–32, Mar 2003.

[14] Ali Javey, Hyoungsub Kim, Markus Brink, Qian Wang, Ant Ural, Jing Guo, Paul McIntyre, Paul McEuen, Mark Lundstrom, and Hongjie Dai. High-k dielectrics for advanced carbon-nanotube transistors and logic gates. *Nature Materials*, 1:241, Nov 2002.

[15] Z. J. Donhauser, B. A. Mantooth, K. F. Kelly, L. A. Bumm, J. D. Monnell, J. J. Stapleton, D. W. Price, A. M. Rawlett, D. L. Allara, J. M. Tour, and

P. S. Weiss. Conductance switching in single molecules through conformational changes. *Science*, 292(5525):2303–2307, 2001.

[16] Charles P. Collier, Gunter Mattersteig, Eric W. Wong, Yi Luo, Kristen Beverly, José Sampaio, Françisco M. Raymo, J. Fraser Stoddart, and James R. Heath. A [2]catenane-based solid state electronically reconfigurable switch. *Science*, 289(5482):1172–1175, 2000.

[17] A. S. Martin, J. R. Sambles, and G. J. Ashwell. Molecular rectifier. *Phys. Rev. Lett.*, 70:218–221, Jan 1993.

[18] Aleksandar Staykov, Daijiro Nozaki, and Kazunari Yoshizawa. Theoretical study of donor-bridgeacceptor unimolecular electric rectifier. *The Journal of Physical Chemistry C*, 111(31):11699–11705, 2007.

[19] M. P. Samanta, W. Tian, S. Datta, J. I. Henderson, and C. P. Kubiak. Electronic conduction through organic molecules. *Phys. Rev. B*, 53:R7626–R7629, Mar 1996.

[20] Chao Wang, Yongjie Hu, Charles M. Lieber, and Shouheng Sun. Ultrathin au nanowires and their transport properties. *Journal of the American Chemical Society*, 130(28):8902–8903, 2008.

[21] Andrei Kolmakov and Martin Moskovits. Chemical sensing and catalysis by one-dimensional metal-oxide nanostructures. *Annual Review of Materials Research*, 34(1):151–180, 2004.

[22] G. Raschke, S. Brogl, A. S. Susha, A. L. Rogach, T. A. Klar, J. Feldmann, B. Fieres, N. Petkov, T. Bein, A. Nichtl, and K. Kürzinger. Gold nanoshells improve single nanoparticle molecular sensors. *Nano Letters*, 4(10):1853–1857, 2004.

[23] Thomas Rueckes, Kyoungha Kim, Ernesto Joselevich, Greg Y. Tseng, Chin-Li Cheung, and Charles M. Lieber. Carbon nanotube-based nonvolatile random access memory for molecular computing. *Science*, 289(5476):94–97, 2000.

[24] Rainer Waser and Masakazu Aono. Nanoionics-based resistive switching memories. *Nature Materials*, 6:833, Nov 2007.

[25] Denis Fichou. Structural order in conjugated oligothiophenes and its implications on opto-electronic devices. *J. Mater. Chem.*, 10:571–588, 2000.

[26] M. Bürkle, L. A. Zotti, J. K. Viljas, D. Vonlanthen, A. Mishchenko, T. Wandlowski, M. Mayor, G. Schön, and F. Pauly. *Ab initio* study of the thermopower of biphenyl-based single-molecule junctions. *Phys. Rev. B*, 86:115304, Sep 2012.

[27] O. Entin-Wohlman, Y. Imry, and A. Aharony. Three-terminal thermoelectric transport through a molecular junction. *Phys. Rev. B*, 82:115314, Sep 2010.

[28] Kanhayalal Baheti, Jonathan A. Malen, Peter Doak, Pramod Reddy, Sung-Yeon Jang, T. Don Tilley, Arun Majumdar, , and Rachel A. Segalman. Probing the chemistry of molecular heterojunctions using thermoelectricity. *Nano Letters*, 8(2):715–719, 2008.

[29] Shannon K. Yee, Jonathan A. Malen, Arun Majumdar, and Rachel A. Segalman. Thermoelectricity in fullerene–metal heterojunctions. *Nano Letters*, 11(10):4089–4094, 2011.

[30] See Kei Lee, Tatsuhiko Ohto, Ryo Yamada, and Hirokazu Tada. Thermopower of benzenedithiol and c60 molecular junctions with ni and au electrodes. *Nano Letters*, 14(9):5276–5280, 2014.

[31] Jonathan A. Malen, Peter Doak, Kanhayalal Baheti, T. Don Tilley, Rachel A. Segalman, and Arun Majumdar. Identifying the length dependence of orbital alignment and contact coupling in molecular heterojunctions. *Nano Letters*, 9(3):1164–1169, 2009.

[32] Janakiraman Balachandran, Pramod Reddy, Barry D. Dunietz, and Vikram Gavini. End-group-induced charge transfer in molecular junctions: Effect on electronic-structure and thermopower. *The Journal of Physical Chemistry Letters*, 3(15):1962–1967, 2012.

[33] Youngsang Kim, Wonho Jeong, Kyeongtae Kim, Woochul Lee, and Pramod Reddy. Electrostatic control of thermoelectricity in molecular junctions. *Nat Nano*, 9(11):881–885, Nov 2014.

[34] Víctor M García-Suárez, Colin J Lambert, David Zs Manrique, and Thomas Wandlowski. Redox control of thermopower and figure of merit in phase-coherent molecular wires. *Nanotechnology*, 25(20):205402, 2014.

[35] Aaron Tan, Janakiraman Balachandran, Seid Sadat, Vikram Gavini, Barry D. Dunietz, Sung-Yeon Jang, and Pramod Reddy. Effect of length and contact chemistry on the electronic structure and thermoelectric properties of molecular junctions. *Journal of the American Chemical Society*, 133(23):8838–8841, 2011.

[36] J. R. Widawsky, W. Chen, H. Vázquez, T. Kim, R. Breslow, M. S. Hybertsen, and L. Venkataraman. Length-dependent thermopower of highly conducting au–c bonded single molecule junctions. *Nano Letters*, 13(6):2889–2894, 2013.

[37] Laura Rincon-Garcia, Ali K. Ismael, Charalambos Evangeli, Iain Grace, Gabino Rubio-Bollinger, Kyriakos Porfyrakis, Nicolas Agrait, and Colin J. Lambert. Molecular design and control of fullerene-based bi-thermoelectric materials. *Nat Mater*, 15(3):289–293, Mar 2016.

[38] A. Shakouri and Suquan Li. Thermoelectric power factor for electrically conductive polymers. In *Thermoelectrics, 1999. Eighteenth International Conference on*, pages 402–406, Aug 1999.

[39] Pramod Reddy, Sung-Yeon Jang, Rachel A. Segalman, and Arun Majumdar. Thermoelectricity in molecular junctions. *Science*, 315(5818):1568–1571, 2007.

[40] Jonathan A. Malen, Shannon K. Yee, Arun Majumdar, and Rachel A. Segalman. Fundamentals of energy transport, energy conversion, and thermal properties in organic–inorganic heterojunctions. *Chemical Physics Letters*, 491(4–6):109 – 122, 2010.

[41] Jonathan A. Malen, Peter Doak, Kanhayalal Baheti, T. Don Tilley, Arun Majumdar, and Rachel A. Segalman. The nature of transport variations in molecular heterojunction electronics. *Nano Letters*, 9(10):3406–3412, 2009.

[42] Jonathan R. Widawsky, Pierre Darancet, Jeffrey B. Neaton, and Latha Venkataraman. Simultaneous determination of conductance and thermopower of single molecule junctions. *Nano Letters*, 12(1):354–358, 2012.

[43] Duck-Young Chung, Tim Hogan, Paul Brazis, Melissa Rocci-Lane, Carl Kannewurf, Marina Bastea, Ctirad Uher, and Mercouri G. Kanatzidis. Csbi4te6: A high-performance thermoelectric material for low-temperature applications. *Science*, 287(5455):1024–1027, 2000.

[44] Li-Dong Zhao, Vinayak P. Dravid, and Mercouri G. Kanatzidis. The panoscopic approach to high performance thermoelectrics. *Energy Environ. Sci.*, 7:251–268, 2014.

[45] Qian Zhang, Yimeng Sun, Wei Xu, and Daoben Zhu. Organic thermoelectric materials: Emerging green energy materials converting heat to electricity directly and efficiently. *Advanced Materials*, 26(40):6829–6851, 2014.

[46] C. M. Finch, V. M. García-Suárez, and C. J. Lambert. Giant thermopower and figure of merit in single-molecule devices. *Phys. Rev. B*, 79:033405, Jan 2009.

[47] Charalambos Evangeli, Katalin Gillemot, Edmund Leary, M. Teresa González, Gabino Rubio-Bollinger, Colin J. Lambert, and Nicolás Agraït. Engineering the thermopower of c60 molecular junctions. *Nano Letters*, 13(5):2141–2145, 2013.

[48] Ali K. Ismael, Iain Grace, and Colin J. Lambert. Increasing the thermopower of crown-ether-bridged anthraquinones. *Nanoscale*, 7:17338–17342, 2015.

[49] Qusiy H. Al-Galiby, Hatef Sadeghi, Laith A. Algharagholy, Iain Grace, and Colin Lambert. Tuning the thermoelectric properties of metallo-porphyrins. *Nanoscale*, 8:2428–2433, 2016.

[50] John Moreland and J. W. Ekin. Electron tunneling experiments using nb-sn "break" junctions. *Journal of Applied Physics*, 58(10):3888–3895, 1985.

[51] C.J. Muller, J.M. van Ruitenbeek, and L.J. de Jongh. Experimental observation of the transition from weak link to tunnel junction. *Physica C: Superconductivity*, 191(3):485 – 504, 1992.

[52] M. A. Reed, C. Zhou, C. J. Muller, T. P. Burgin, and J. M. Tour. Conductance of a molecular junction. *Science*, 278(5336):252–254, 1997.

[53] Bingqian Xu and Nongjian J. Tao. Measurement of single-molecule resistance by repeated formation of molecular junctions. *Science*, 301(5637):1221–1223, 2003.

[54] David J. Wold and C. Daniel Frisbie. Formation of metalmoleculemetal tunnel junctions: microcontacts to alkanethiol monolayers with a conducting afm tip. *Journal of the American Chemical Society*, 122(12):2970–2971, 2000.

[55] Michael Thoss and Ferdinand Evers. Perspective: Theory of quantum transport in molecular junctions. *The Journal of Chemical Physics*, 148(3):030901, 2018.

[56] Yongqiang Xue and Mark A. Ratner. Theoretical principles of single-molecule electronics: A chemical and mesoscopic view. *International Journal of Quantum Chemistry*, 102(5):911–924, 2005.

[57] M. C. Payne, M. P. Teter, D. C. Allan, T. A. Arias, and J. D. Joannopoulos. Iterative minimization techniques for ab initio total-energy calculations: molecular dynamics and conjugate gradients. *Rev. Mod. Phys.*, 64:1045–1097, Oct 1992.

[58] Pablo Ordejón, Emilio Artacho, and José M. Soler. Self-consistent order-n density-functional calculations for very large systems. *Phys. Rev. B*, 53:R10441–R10444, Apr 1996.

[59] S. Sanvito, C. J. Lambert, J. H. Jefferson, and A. M. Bratkovsky. General green's-function formalism for transport calculations with spd hamiltonians and giant magnetoresistance in co- and ni-based magnetic multilayers. *Phys. Rev. B*, 59:11936–11948, May 1999.

[60] Jeremy Taylor, Hong Guo, and Jian Wang. Ab initio modeling of quantum transport properties of molecular electronic devices. *Phys. Rev. B*, 63:245407, Jun 2001.

[61] Mads Brandbyge, José-Luis Mozos, Pablo Ordejón, Jeremy Taylor, and Kurt Stokbro. Density-functional method for nonequilibrium electron transport. *Phys. Rev. B*, 65:165401, Mar 2002.

[62] Mao Sumino, Kentaro Harada, Masaaki Ikeda, Saburo Tanaka, Koji Miyazaki, and Chihaya Adachi. Thermoelectric properties of n-type c60 thin films and their application in organic thermovoltaic devices. *Applied Physics Letters*, 99(9), 2011.

[63] Hylke B. Akkerman, Paul W. M. Blom, Dago M. de Leeuw, and Bert de Boer. Towards molecular electronics with large-area molecular junctions. *Nature*, 441(7089):69–72, May 2006.

[64] Tao Li, Jonas Rahlf Hauptmann, Zhongming Wei, Søren Petersen, Nicolas Bovet, Tom Vosch, Jesper Nygård, Wenping Hu, Yunqi Liu, Thomas Bjørnholm, Kasper Nørgaard, and Bo W. Laursen. Solution-processed ultrathin chemically derived graphene films as soft top contacts for solid-state molecular electronic junctions. *Advanced Materials*, 24(10):1333–1339, 2012.

[65] Gunuk Wang, Yonghun Kim, Minhyeok Choe, Tae-Wook Kim, and Takhee Lee. A new approach for molecular electronic junctions with a multilayer graphene electrode. *Advanced Materials*, 23(6):755–760, 2011.

[66] Alexander B. Neuhausen, Ali Hosseini, Joseph A. Sulpizio, Christopher E. D. Chidsey, and David Goldhaber-Gordon. Molecular junctions of self-assembled

monolayers with conducting polymer contacts. *ACS Nano*, 6(11):9920–9931, 2012.

[67] Shubhaditya Majumdar, Jonatan A. Sierra-Suarez, Scott N. Schiffres, Wee-Liat Ong, III C. Fred Higgs, Alan J. H. McGaughey, and Jonathan A. Malen. Vibrational mismatch of metal leads controls thermal conductance of self-assembled monolayer junctions. *Nano Letters*, 15(5):2985–2991, 2015.

[68] Robert Y. Wang, Rachel A. Segalman, and Arun Majumdar. Room temperature thermal conductance of alkanedithiol self-assembled monolayers. *Applied Physics Letters*, 89(17), 2006.

[69] Gediminas Kiršanskas, Qian Li, Karsten Flensberg, Gemma C. Solomon, and Martin Leijnse. Designing -stacked molecular structures to control heat transport through molecular junctions. *Applied Physics Letters*, 105(23), 2014.

[70] G. Jeffrey Snyder and Eric S. Toberer. Complex thermoelectric materials. *Nature Materials*, 7:105, Feb 2008.

[71] Rama Venkatasubramanian, Edward Siivola, Thomas Colpitts, and Brooks O'Quinn. Thin-film thermoelectric devices with high room-temperature figures of merit. *Nature*, 413(6856):597–602, Oct 2001.

[72] T. J. Seebeck. Ueber die magnetische polarisation der metalle und erze durch temperaturdifferenz. *Annalen der Physik*, 82(3):253–286.

[73] Ward Van Heddeghem, Sofie Lambert, Bart Lannoo, Didier Colle, Mario Pickavet, and Piet Demeester. Trends in worldwide {ICT} electricity consumption from 2007 to 2012. *Computer Communications*, 50:64 – 76, 2014.

[74] Hui Shi, Congcong Liu, Jingkun Xu, Haijun Song, Baoyang Lu, Fengxing Jiang, Weiqiang Zhou, Ge Zhang, and Qinglin Jiang. Facile fabrication of PEDOT:PSS/polythiophenes bilayered nanofilms on pure organic electrodes and their thermoelectric performance. *ACS Applied Materials & Interfaces*, 5(24):12811–12819, 2013.

[75] T. Meier, F. Menges, P. Nirmalraj, H. Hölscher, H. Riel, and B. Gotsmann. Length-dependent thermal transport along molecular chains. *Phys. Rev. Lett.*, 113:060801, Aug 2014.

[76] Hatef Sadeghi, Sara Sangtarash, and Colin J. Lambert. Oligoyne molecular junctions for efficient room temperature thermoelectric power generation. *Nano Letters*, 15(11):7467–7472, 2015.

[77] Haoxue Han, Yong Zhang, Nan Wang, Majid Kabiri Samani, Yuxiang Ni, Zainelabideen Y. Mijbil, Michael Edwards, Shiyun Xiong, Kimmo Saaskilahti, Murali Murugesan, Yifeng Fu, Lilei Ye, Hatef Sadeghi, Steven Bailey, Yuriy A. Kosevich, Colin J. Lambert, Johan Liu, and Sebastian Volz. Functionalization mediates heat transport in graphene nanoflakes. *Nat Commun*, 7, Apr 2016.

[78] G.-H. Kim, L. Shao, K. Zhang, and K. P. Pipe. Engineered doping of organic semiconductors for enhanced thermoelectric efficiency. *Nature Materials*, 12:719, May 2013.

[79] Olga Bubnova, Zia Ullah Khan, Abdellah Malti, Slawomir Braun, Mats Fahlman, Magnus Berggren, and Xavier Crispin. Optimization of the thermoelectric figure of?merit?in the conducting polymer poly(3,4-ethylenedioxythiophene). *Nature Materials*, 10:429, May 2011.

[80] Efthimios Kaxiras. *Atomic and Electronic Structure of Solids*. Cambridge University Press, 2003.

[81] S. Datta. *Quantum Transport: Atom to Transistor*. Cambridge University Press, 2005.

[82] R. M. Martin. *Electronic Structure: Basic Theory and Practical Methods*. Cambridge University Press, 2004.

[83] M. Born and R. Oppenheimer. Zur quantentheorie der molekeln. *Annalen der Physik*, 389(20):457–484, 1927.

[84] P. Hohenberg and W. Kohn. Inhomogeneous electron gas. *Phys. Rev.*, 136:B864–B871, Nov 1964.

[85] W. Kohn and L. J. Sham. Self-consistent equations including exchange and correlation effects. *Phys. Rev.*, 140:1133–1138, Nov 1965.

[86] W. Kohn. Nobel lecture: Electronic structure of matter¯wave functions and density functionals. *Rev. Mod. Phys.*, 71:1253–1266, Oct 1999.

[87] John P. Perdew and Yue Wang. Accurate and simple analytic representation of the electron-gas correlation energy. *Phys. Rev. B*, 45:13244–13249, Jun 1992.

[88] A. D. Becke. Density-functional exchange-energy approximation with correct asymptotic behavior. *Phys. Rev. A*, 38:3098–3100, Sep 1988.

[89] John P. Perdew, Kieron Burke, and Matthias Ernzerhof. Generalized gradient approximation made simple. *Phys. Rev. Lett.*, 77:3865–3868, Oct 1996.

[90] José M Soler, Emilio Artacho, Julian D Gale, Alberto García, Javier Junquera, Pablo Ordejón, and Daniel Sánchez-Portal. The siesta method for ab initio order- n materials simulation. *Journal of Physics: Condensed Matter*, 14(11):2745, 2002.

[91] N. Troullier and José Luís Martins. Efficient pseudopotentials for plane-wave calculations. *Phys. Rev. B*, 43:1993–2006, Jan 1991.

[92] L Fernández-Seivane, M A Oliveira, S Sanvito, and J Ferrer. On-site approximation for spin–orbit coupling in linear combination of atomic orbitals density functional methods. *Journal of Physics: Condensed Matter*, 18(34):7999, 2006.

[93] Dvira Segal, Abraham Nitzan, and Peter Hänggi. Thermal conductance through molecular wires. *The Journal of Chemical Physics*, 119(13):6840–6855, 2003.

[94] B. J. van Wees, H. van Houten, C. W. J. Beenakker, J. G. Williamson, L. P. Kouwenhoven, D. van der Marel, and C. T. Foxon. Quantized conductance of

point contacts in a two-dimensional electron gas. *Phys. Rev. Lett.*, 60:848–850, Feb 1988.

[95] Nicolás Agraıt, Alfredo Levy Yeyati, and Jan M. van Ruitenbeek. Quantum properties of atomic-sized conductors. *Physics Reports*, 377(2):81 – 279, 2003.

[96] Daniel S. Fisher and Patrick A. Lee. Relation between conductivity and transmission matrix. *Phys. Rev. B*, 23:6851–6854, Jun 1981.

[97] M. Büttiker, Y. Imry, R. Landauer, and S. Pinhas. Generalized many-channel conductance formula with application to small rings. *Phys. Rev. B*, 31:6207–6215, May 1985.

[98] M. Büttiker. Four-terminal phase-coherent conductance. *Phys. Rev. Lett.*, 57:1761–1764, Oct 1986.

[99] G. Rubio, N. Agraït, and S. Vieira. Atomic-sized metallic contacts: Mechanical properties and electronic transport. *Phys. Rev. Lett.*, 76:2302–2305, Mar 1996.

[100] Elke Scheer, Nicolás Agraït, Juan Carlos Cuevas, Alfredo Levy Yeyati, Bas Ludoph, Alvaro Martín-Rodero, Gabino Rubio Bollinger, Jan M. van Ruitenbeek, and Cristián Urbina. The signature of chemical valence in the electrical conduction through a single-atom contact. *Nature*, 394:154, Jul 1998.

[101] A. I. Yanson, G. Rubio Bollinger, H. E. van den Brom, N. Agraït, and J. M. van Ruitenbeek. Formation and manipulation of a metallic wire of single gold atoms. *Nature*, 395:783, Oct 1998.

[102] Mariana M. Odashima, Beatriz G. Prado, and E. Vernek. Pedagogical introduction to equilibrium Green's functions: condensed-matter examples with numerical implementations. *Revista Brasileira de Ensino de FÃsica*, 39, 00 2017.

[103] J. Ferrer, C. J. Lambert, V. M. García-Suárez, D. Z. Manrique, D. Visontai, L. Oroszlany, R. Rodríguez-Ferradás, I. Grace, S. W. D. Bailey, K. Gillemot,

H. Sadeghi, and L. A. Algharagholy. GOLLUM: a next-generation simulation tool for electron, thermal and spin transport. *New Journal of Physics*, 16(9):093029, September 2014.

[104] T. C. Harman, P. J. Taylor, M. P. Walsh, and B. E. LaForge. Quantum dot superlattice thermoelectric materials and devices. *Science*, 297(5590):2229–2232, 2002.

[105] Bed Poudel, Qing Hao, Yi Ma, Yucheng Lan, Austin Minnich, Bo Yu, Xiao Yan, Dezhi Wang, Andrew Muto, Daryoosh Vashaee, Xiaoyuan Chen, Junming Liu, Mildred S. Dresselhaus, Gang Chen, and Zhifeng Ren. High-thermoelectric performance of nanostructured bismuth antimony telluride bulk alloys. *Science*, 320(5876):634–638, 2008.

[106] Kazuhiro Yanagi, Shouhei Kanda, Yuki Oshima, Yoshimasa Kitamura, Hideki Kawai, Takahiro Yamamoto, Taishi Takenobu, Yusuke Nakai, and Yutaka Maniwa. Tuning of the thermoelectric properties of one-dimensional material networks by electric double layer techniques using ionic liquids. *Nano Letters*, 14(11):6437–6442, 2014.

[107] A. Kambili, G. Fagas, Vladimir I. Fal'ko, and C. J. Lambert. Phonon-mediated thermal conductance of mesoscopic wires with rough edges. *Phys. Rev. B*, 60:15593–15596, Dec 1999.

[108] G. Fagas, A. G. Kozorezov, C. J. Lambert, J. K. Wigmore, A. Peacock, A. Poelaert, and R. den Hartog. Lattice dynamics of a disordered solid-solid interface. *Phys. Rev. B*, 60:6459–6464, Sep 1999.

[109] Troels Markussen. Phonon interference effects in molecular junctions. *The Journal of Chemical Physics*, 139(24), 2013.

[110] Marius Bürkle, Thomas J. Hellmuth, Fabian Pauly, and Yoshihiro Asai. First-principles calculation of the thermoelectric figure of merit for

[2,2]paracyclophane-based single-molecule junctions. *Phys. Rev. B*, 91:165419, Apr 2015.

[111] Gediminas Kiršanskas, Qian Li, Karsten Flensberg, Gemma C. Solomon, and Martin Leijnse. Designing -stacked molecular structures to control heat transport through molecular junctions. *Applied Physics Letters*, 105(23), 2014.

[112] G. Thorgilsson, G. Viktorsson, and S.I. Erlingsson. Recursive greens function method for multi-terminal nanostructures. *Journal of Computational Physics*, 261:256 – 266, 2014.

[113] Marjan Famili, Iain Grace, Hatef Sadeghi, and Colin J. Lambert. Suppression of phonon transport in molecular christmas trees. *ChemPhysChem*, 18(10):1234–1241, 2017.

[114] Xunshan Liu, Sara Sangtarash, David Reber, Dan Zhang, Hatef Sadeghi, Jia Shi, Zong-Yuan Xiao, Wenjing Hong, Colin J. Lambert, and Shi-Xia Liu. Gating of quantum interference in molecular junctions by heteroatom substitution. *Angewandte Chemie International Edition*, 56(1):173–176, 2017.

[115] David Zsolt Manrique, Qusiy Al-Galiby, Wenjing Hong, and Colin J. Lambert. A new approach to materials discovery for electronic and thermoelectric properties of single-molecule junctions. *Nano Letters*, 16(2):1308–1316, 2016.

[116] Ryo Yamada, Hiroaki Kumazawa, Tomoharu Noutoshi, Shoji Tanaka, and Hirokazu Tada. Electrical conductance of oligothiophene molecular wires. *Nano Letters*, 8(4):1237–1240, 2008.

[117] Eung-Gun Kim and Jean-Luc Brédas. Electronic evolution of poly(3,4-ethylenedioxythiophene) (PEDOT): From the isolated chain to the pristine and heavily doped crystals. *Journal of the American Chemical Society*, 130(50):16880–16889, 2008.

[118] Shay Potash and Shlomo Rozen. New conjugated oligothiophenes containing the unique arrangement of internal adjacent [all]-s,s-oxygenated thiophene fragments. *Chemistry – A European Journal*, 19(17):5289–5296, 2013.

[119] P. Pingel, R. Schwarzl, and D. Neher. Effect of molecular p-doping on hole density and mobility in poly(3-hexylthiophene). *Applied Physics Letters*, 100(14):143303, 2012.

[120] Marcel Schubert, Eduard Preis, James C. Blakesley, Patrick Pingel, Ullrich Scherf, and Dieter Neher. Mobility relaxation and electron trapping in a donor/acceptor copolymer. *Phys. Rev. B*, 87:024203, Jan 2013.

[121] Guanghao Lu, James Blakesley, Scott Himmelberger, Patrick Pingel, Johannes Frisch, Ingo Lieberwirth, Ingo Salzmann, Martin Oehzelt, Riccardo Di Pietro, Alberto Salleo, Norbert Koch, and Dieter Neher. Moderate doping leads to high performance of semiconductor/insulator polymer blend transistors. *Nature Communications*, 4:1588, Mar 2013.

[122] Jean Roncali, Philippe Blanchard, and Pierre Frere. 3,4-ethylenedioxythiophene (EDOT) as a versatile building block for advanced functional [small pi]-conjugated systems. *J. Mater. Chem.*, 15:1589–1610, 2005.

[123] Rupali Gangopadhyay, Bidisa Das, and Mijanur Rahaman Molla. How does pedot combine with pss? insights from structural studies. *RSC Adv.*, 4:43912–43920, 2014.

[124] Olga Bubnova, Zia Ullah Khan, Hui Wang, Slawomir Braun, Drew R. Evans, Manrico Fabretto, Pejman Hojati-Talemi, Daniel Dagnelund, Jean-Baptiste Arlin, Yves H. Geerts, Simon Desbief, Dag W. Breiby, Jens W. Andreasen, Roberto Lazzaroni, Weimin M. Chen, Igor Zozoulenko, Mats Fahlman, Peter J. Murphy, Magnus Berggren, and Xavier Crispin. Semi-metallic polymers. *Nature Materials*, 13:190, Dec 2013.

[125] J. B. Neaton, Mark S. Hybertsen, and Steven G. Louie. Renormalization of molecular electronic levels at metal-molecule interfaces. *Phys. Rev. Lett.*, 97:216405, Nov 2006.

[126] Víctor M García-Suárez and Colin J Lambert. First-principles scheme for spectral adjustment in nanoscale transport. *New Journal of Physics*, 13(5):053026, 2011.

[127] Qingkai Yu, Jie Lian, Sujitra Siriponglert, Hao Li, Yong P. Chen, and Shin-Shem Pei. Graphene segregated on ni surfaces and transferred to insulators. *Applied Physics Letters*, 93(11):113103, 2008.

[128] Abraham Nitzan and Mark A. Ratner. Electron transport in molecular wire junctions. *Science*, 300(5624):1384–1389, 2003.

[129] Michael Galperin, Mark A. Ratner, Abraham Nitzan, and Alessandro Troisi. Nuclear coupling and polarization in molecular transport junctions: Beyond tunneling to function. *Science*, 319(5866):1056–1060, 2 2008.

[130] Andrea Vezzoli, Iain M. Grace, Carly Brooke, Richard J. Nichols, Colin J. Lambert, and Simon J. Higgins. Soft versus hard junction formation for -terthiophene molecular wires and their charge transfer complexes. *The Journal of Chemical Physics*, 146(9):092307, 2017.

[131] Yanpeng Liu, Li Yuan, Ming Yang, Yi Zheng, Linjun Li, Libo Gao, Nisachol Nerngchamnong, Chang Tai Nai, C. S. Suchand Sangeeth, Yuan Ping Feng, Christian A. Nijhuis, and Kian Ping Loh. Giant enhancement in vertical conductivity of stacked cvd graphene sheets by self-assembled molecular layers. *Nature Communications*, 5:5461, Nov 2014.

[132] Dong Xiang, Hyunhak Jeong, Takhee Lee, and Dirk Mayer. Mechanically controllable break junctions for molecular electronics. *Advanced Materials*, 25(35):4845–4867, 2016.

[133] David Zsolt Manrique, Qusiy Al-Galiby, Wenjing Hong, and Colin J. Lambert. A new approach to materials discovery for electronic and thermoelectric properties of single-molecule junctions. *Nano Letters*, 16(2):1308–1316, 2016.

[134] Hatef Sadeghi, Sara Sangtarash, and Colin J. Lambert. Oligoyne molecular junctions for efficient room temperature thermoelectric power generation. *Nano Letters*, 15(11):7467–7472, 2015.

[135] Colin Lambert, Hatef Sadeghi, and Qusiy Al Galiby. Quantum-interference-enhanced thermoelectricity in single molecules and molecular films. *Comptes Rendus Physique*, 17:1084–1095, 08 2016.

[136] Yeonsik Jang, Hyunhak Jeong, Dongku Kim, Wang-Taek Hwang, Jun-Woo Kim, Inho Jeong, Hyunwook Song, Jiyoung Yoon, Gyu-Chul Yi, Heejun Jeong, and Takhee Lee. Electrical characterization of benzenedithiolate molecular electronic devices with graphene electrodes on rigid and flexible substrates. *Nanotechnology*, 27(14):145301, 2016.

[137] Jing-Jing Chen, Jie Meng, Yang-Bo Zhou, Han-Chun Wu, Ya-Qing Bie, Zhi-Min Liao, and Da-Peng Yu. Layer-by-layer assembly of vertically conducting graphene devices. *Nature Communications*, 4:1921, May 2013.

[138] Hylke Akkerman and Bert de Boer. Topical review: Electrical conduction through single molecules and self-assembled monolayers. *Journal of Physics: Condensed Matter*, 20, 01 2008.

[139] Richard L. McCreery and Adam Johan Bergren. Progress with molecular electronic junctions: Meeting experimental challenges in design and fabrication. *Advanced Materials*, 21(43):4303–4322, 2009.

[140] C. S. Suchand Sangeeth, Abel T. Demissie, Li Yuan, Tao Wang, C. Daniel Frisbie, and Christian A. Nijhuis. Comparison of dc and ac transport in 1.5–7.5 nm oligophenylene imine molecular wires across two junction platforms: Eutectic

ga–in versus conducting probe atomic force microscope junctions. *Journal of the American Chemical Society*, 138(23):7305–7314, 2016.

[141] K. S. Novoselov, D. Jiang, F. Schedin, T. J. Booth, V. V. Khotkevich, S. V. Morozov, and A. K. Geim. Two-dimensional atomic crystals. *Proceedings of the National Academy of Sciences*, 102(30):10451–10453, 2005.

[142] Kirill I Bolotin, KJ Sikes, Zd Jiang, M Klima, G Fudenberg, J Hone, P Kim, and HL Stormer. Ultrahigh electron mobility in suspended graphene. *Solid State Communications*, 146(9):351–355, 2008.

[143] A. K. Geim and K. S. Novoselov. The rise of graphene. *Nature Materials*, 6:183, Mar 2007.

[144] Xinran Wang, Xiaolin Li, Li Zhang, Youngki Yoon, Peter K. Weber, Hailiang Wang, Jing Guo, and Hongjie Dai. N-doping of graphene through electrothermal reactions with ammonia. *Science*, 324(5928):768–771, 2009.

[145] Michael S. Inkpen, Mario Lemmer, Nathan Fitzpatrick, David C. Milan, Richard J. Nichols, Nicholas J. Long, and Tim Albrecht. New insights into single-molecule junctions using a robust, unsupervised approach to data collection and analysis. *Journal of the American Chemical Society*, 137(31):9971–9981, 2015.

[146] Jariyanee Prasongkit and Alexandre R. Rocha. Quantum interference effects in biphenyl dithiol for gas detection. *RSC Adv.*, 6:59299–59304, 2016.

[147] M. Bürkle, J. K. Viljas, D. Vonlanthen, A. Mishchenko, G. Schön, M. Mayor, T. Wandlowski, and F. Pauly. Conduction mechanisms in biphenyl dithiol single-molecule junctions. *Phys. Rev. B*, 85:075417, Feb 2012.

[148] Mario Lemmer, Michael S. Inkpen, Katja Kornysheva, Nicholas J. Long, and Tim Albrecht. Unsupervised vector-based classification of single-molecule charge transport data. *Nature Communications*, 7:12922, Oct 2016.

[149] G. V. Bianco, M. Losurdo, M. M. Giangregorio, P. Capezzuto, and G. Bruno. Exploring and rationalising effective n-doping of large area cvd-graphene by nh3. *Phys. Chem. Chem. Phys.*, 16:3632–3639, 2014.

[150] Giuseppe Valerio Bianco, Maria Losurdo, Alberto Sacchetti, Pio Capezzuto, and Giovanni Bruno. Demonstration of improved charge transfer in graphene/au nanorods plasmonic hybrids stabilized by benzyl thiol linkers. *Journal of Nanomaterials*, 2016, 2015.

[151] Ji Eun Lee, Gwanghyun Ahn, Jihye Shim, Young Sik Lee, and Sunmin Ryu. Optical separation of mechanical strain from charge doping in graphene. *Nature Communications*, 3:1024, Aug 2012.

[152] Sriharsha V. Aradhya and Latha Venkataraman. Single-molecule junctions beyond electronic transport. *Nature Nanotechnology*, 8:399, 06 2013.

[153] Dong Xiang, Xiaolong Wang, Chuancheng Jia, Takhee Lee, and Xuefeng Guo. Molecular-scale electronics: From concept to function. *Chemical Reviews*, 116(7):4318–4440, 2016.

[154] Stefan Thiele, Franck Balestro, Rafik Ballou, Svetlana Klyatskaya, Mario Ruben, and Wolfgang Wernsdorfer. Electrically driven nuclear spin resonance in single-molecule magnets. *Science*, 344(6188):1135–1138, 2014.

[155] Wei Du, Tao Wang, Hong-Son Chu, Lin Wu, Rongrong Liu, Song Sun, Wee Kee Phua, Lejia Wang, Nikodem Tomczak, and Christian A. Nijhuis. On-chip molecular electronic plasmon sources based on self-assembled monolayer tunnel junctions. *Nature Photonics*, 10:274–280, 03 2016.

[156] Constant M. Guédon, Hennie Valkenier, Troels Markussen, Kristian S. Thygesen, Jan C. Hummelen, and Sense Jan van der Molen. Observation of quantum interference in molecular charge transport. *Nature Nanotechnology*, 7:305–309, 03 2012.

[157] Timothy A. Su, Madhav Neupane, Michael L. Steigerwald, Latha Venkataraman, and Colin Nuckolls. Chemical principles of single-molecule electronics. *Nature Reviews Materials*, 1:16002, 02 2016.

[158] Chuancheng Jia, Agostino Migliore, Na Xin, Shaoyun Huang, Jinying Wang, Qi Yang, Shuopei Wang, Hongliang Chen, Duoming Wang, Boyong Feng, Zhirong Liu, Guangyu Zhang, Da-Hui Qu, He Tian, Mark A. Ratner, H. Q. Xu, Abraham Nitzan, and Xuefeng Guo. Covalently bonded single-molecule junctions with stable and reversible photoswitched conductivity. *Science*, 352(6292):1443–1445, 2016.

[159] Na Xin, Jinying Wang, Chuancheng Jia, Zitong Liu, Xisha Zhang, Chenmin Yu, Mingliang Li, Shuopei Wang, Yao Gong, Hantao Sun, Guanxin Zhang, Zhirong Liu, Guangyu Zhang, Jianhui Liao, Deqing Zhang, and Xuefeng Guo. Stereoelectronic effect-induced conductance switching in aromatic chain single-molecule junctions. *Nano Letters*, 17(2):856–861, 2017.

[160] Xiaodong Yin, Yaping Zang, Liangliang Zhu, Jonathan Z. Low, Zhen-Fei Liu, Jing Cui, Jeffrey B. Neaton, Latha Venkataraman, and Luis M. Campos. A reversible single-molecule switch based on activated antiaromaticity. *Science Advances*, 3(10), 2017.

[161] Brian Capozzi, Jianlong Xia, Olgun Adak, Emma J. Dell, Zhen-Fei Liu, Jeffrey C. Taylor, Jeffrey B. Neaton, Luis M. Campos, and Latha Venkataraman. Single-molecule diodes with high rectification ratios through environmental control. *Nature Nanotechnology*, 10:522–527, 05 2015.

[162] Xiaoping Chen, Max Roemer, Li Yuan, Wei Du, Damien Thompson, Enrique del Barco, and Christian A. Nijhuis. Molecular diodes with rectification ratios exceeding 105 driven by electrostatic interactions. *Nature Nanotechnology*, 12:797–803, 07 2017.

[163] Hyunwook Song, Youngsang Kim, Yun Hee Jang, Heejun Jeong, Mark A. Reed, and Takhee Lee. Observation of molecular orbital gating. *Nature*, 462:1039–1043, 12 2009.

[164] Mickael L. Perrin, Enrique Burzuri, and Herre S. J. van der Zant. Single-molecule transistors. *Chem. Soc. Rev.*, 44:902–919, 2015.

[165] Kasper Moth-Poulsen and Thomas Bjørnholm. Molecular electronics with single molecules in solid-state devices. *Nature Nanotechnology*, 4:551–556, 08 2009.

[166] Cancan Huang, Alexander V. Rudnev, Wenjing Hong, and Thomas Wandlowski. Break junction under electrochemical gating: testbed for single-molecule electronics. *Chem. Soc. Rev.*, 44:889–901, 2015.

[167] Yuan Liu, Nathan O. Weiss, Xidong Duan, Hung-Chieh Cheng, Yu Huang, and Xiangfeng Duan. Van der waals heterostructures and devices. *Nature Reviews Materials*, 1:16042, 07 2016.

[168] K. S. Novoselov, A. Mishchenko, A. Carvalho, and A. H. Castro Neto. 2d materials and van der waals heterostructures. *Science*, 353(6298), 2016.

[169] Marco Carlotti, Andrii Kovalchuk, Tobias Wächter, Xinkai Qiu, Michael Zharnikov, and Ryan C. Chiechi. Conformation-driven quantum interference effects mediated by through-space conjugation in self-assembled monolayers. *Nature Communications*, 7:13904, 12 2016.

[170] J. Christopher Love, Lara A. Estroff, Jennah K. Kriebel, Ralph G. Nuzzo, and George M. Whitesides. Self-assembled monolayers of thiolates on metals as a form of nanotechnology. *Chemical Reviews*, 105(4):1103–1170, 04 2005.

[171] K. Ueno, S. Nakamura, H. Shimotani, H. T. Yuan, N. Kimura, T. Nojima, H. Aoki, Y. Iwasa, and M. Kawasaki. Discovery of superconductivity in ktao3 by electrostatic carrier doping. *Nature Nanotechnology*, 6:408–4012, 05 2011.

[172] Tian Tian, Peter Rice, Elton J. G. Santos, and Chih-Jen Shih. Multiscale analysis for field-effect penetration through two-dimensional materials. *Nano Letters*, 16(8):5044–5052, 2016.

[173] Lambert Colin J. and Liu Shi-Xia. A magic ratio rule for beginners: A chemist's guide to quantum interference in molecules. *Chemistry A European Journal*, 24(17):4193–4201, 2017.

[174] Woo Jong Yu, Zheng Li, Hailong Zhou, Yu Chen, Yang Wang, Yu Huang, and Xiangfeng Duan. Vertically stacked multi-heterostructures of layered materials for logic transistors and complementary inverters. *Nature Materials*, 12:246–250, 12 2012.

[175] Jia Chuancheng, Wang Qing, Xin Na, Zhou Jian, Gong Yao, Li Lidong, Sun Qiang, and Guo Xuefeng. Logic control of interface induced charge trapping effect for ultrasensitive gas detection with all mirror image symmetry. *Advanced Materials Technologies*, 1(3):1600067, 2016.

[176] Yuxin Liu, Xiaochen Dong, and Peng Chen. Biological and chemical sensors based on graphene materials. *Chem. Soc. Rev.*, 41:2283–2307, 2012.

[177] T. A. Papadopoulos, I. M. Grace, and C. J. Lambert. Control of electron transport through fano resonances in molecular wires. *Phys. Rev. B*, 74:193306, Nov 2006.

[178] M. Magoga and C. Joachim. Conductance of molecular wires connected or bonded in parallel. *Phys. Rev. B*, 59:16011–16021, Jun 1999.

[179] Troels Markussen, Jakob SchiÃ¶tz, and Kristian S. Thygesen. Electrochemical control of quantum interference in anthraquinone-based molecular switches. *The Journal of Chemical Physics*, 132(22):224104, 2010.

[180] H. Vazquez, R. Skouta, S. Schneebeli, M. Kamenetska, R. Breslow, L. Venkataraman, and M. S. Hybertsen. Probing the conductance superposi-

tion law in single-molecule circuits with parallel paths. *Nature Nanotechnology*, 7:663, Sep 2012.

[181] Stefan Ballmann, Rainer Härtle, Pedro B. Coto, Mark Elbing, Marcel Mayor, Martin R. Bryce, Michael Thoss, and Heiko B. Weber. Experimental evidence for quantum interference and vibrationally induced decoherence in single-molecule junctions. *Phys. Rev. Lett.*, 109:056801, Jul 2012.

[182] Sriharsha V. Aradhya, Jeffrey S. Meisner, Markrete Krikorian, Seokhoon Ahn, Radha Parameswaran, Michael L. Steigerwald, Colin Nuckolls, and Latha Venkataraman. Dissecting contact mechanics from quantum interference in single-molecule junctions of stilbene derivatives. *Nano Letters*, 12(3):1643–1647, 2012. PMID: 22352939.

[183] Veerabhadrarao Kaliginedi, Pavel Moreno-GarcÃa, Hennie Valkenier, Wenjing Hong, Víctor M. García-Suárez, Petra Buiter, Jelmer L. H. Otten, Jan C. Hummelen, Colin J. Lambert, and Thomas Wandlowski. Correlations between molecular structure and single-junction conductance: A case study with oligo(phenylene-ethynylene)-type wires. *Journal of the American Chemical Society*, 134(11):5262–5275, 2012. PMID: 22352944.

[184] Carlos R. Arroyo, Simge Tarkuc, Riccardo Frisenda, Johannes S. Seldenthuis, Charlotte H. M. Woerde, Rienk Eelkema, Ferdinand C. Grozema, and Herre S. J. vanâderâ Zant. Signatures of quantum interference effects on charge transport through a single benzene ring. *Angewandte Chemie International Edition*, 52(11):3152–3155, 2013.

[185] San-Huang Ke, Weitao Yang, and Harold U. Baranger. Quantum-interference-controlled molecular electronics. *Nano Letters*, 8(10):3257–3261, 2008. PMID: 18803424.

[186] Sara Sangtarash, Cancan Huang, Hatef Sadeghi, Gleb Sorohhov, JÃŒrg Hauser, Thomas Wandlowski, Wenjing Hong, Silvio Decurtins, Shi-Xia Liu,

and Colin J. Lambert. Searching the hearts of graphene-like molecules for simplicity, sensitivity, and logic. *Journal of the American Chemical Society*, 137(35):11425–11431, 2015. PMID: 26288219.

[187] Chuancheng Jia and Xuefeng Guo. Molecule-electrode interfaces in molecular electronic devices. *Chem. Soc. Rev.*, 42:5642–5660, 2013.

[188] Wenjing Hong, David Zsolt Manrique, Pavel Moreno-GarcÃa, Murat Gulcur, Artem Mishchenko, Colin J. Lambert, Martin R. Bryce, and Thomas Wandlowski. Single molecular conductance of tolanes: Experimental and theoretical study on the junction evolution dependent on the anchoring group. *Journal of the American Chemical Society*, 134(4):2292–2304, 2012. PMID: 22175273.

[189] Zhihai Li, Hui Li, Songjie Chen, Toni Froehlich, Chenyi Yi, Christian SchÃ¶nenberger, Michel Calame, Silvio Decurtins, Shi-Xia Liu, and Eric Borguet. Regulating a benzodifuran single molecule redox switch via electrochemical gating and optimization of molecule/electrode coupling. *Journal of the American Chemical Society*, 136(25):8867–8870, 2014. PMID: 24933522.

[190] Woo Jong Yu, Zheng Li, Hailong Zhou, Yu Chen, Yang Wang, Yu Huang, and Xiangfeng Duan. Vertically stacked multi-heterostructures of layered materials for logic transistors and complementary inverters. *Nature Materials*, 12:246, Dec 2012. Article.

Appendices

Appendix A

General Scattering problem

In this section we would like to solve a general scattering problem to find the transmission and reflection amplitudes in the scattering matrix. Our scattering problem consists of a scattering region , connected to two semi infinite leads as demonstrated in figure A.1.

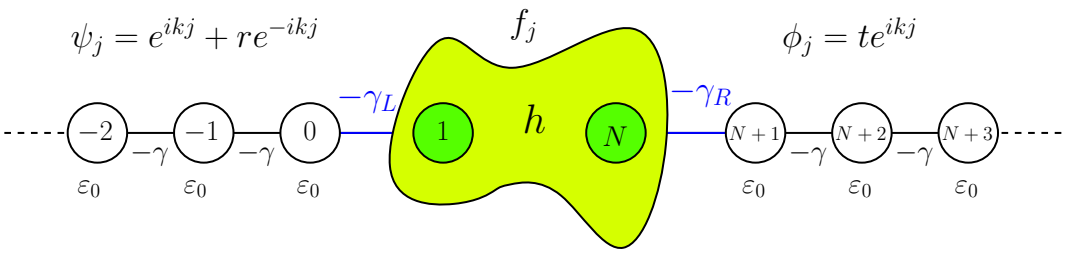

Figure A.1: General scattering problem: Green object is the scatterer, the Hamiltonian of which is represented by h. The wavefunction in scattering region is f_j in the left lead is ψ_j and in the right lead is ϕ_j. The on-site energies in the leads are ε_0 and the hopping integral elements are $-\gamma$. The coupling between left and right leads are represented as $-\gamma_L$ and $-\gamma_R$.

For the system represented in figure A.1, the discrete Shrödinger equation is

$$H\begin{pmatrix}\vdots\\ \psi_{-2}\\ \psi_{-1}\\ \psi_0\\ f_1\\ f_2\\ \vdots\\ f_N\\ \phi_{N+1}\\ \phi_{N+2}\\ \vdots\end{pmatrix} = E\begin{pmatrix}\vdots\\ \psi_{-2}\\ \psi_{-1}\\ \psi_0\\ f_1\\ f_2\\ \vdots\\ f_N\\ \phi_{N+1}\\ \phi_{N+2}\\ \vdots\end{pmatrix}. \tag{A.1}$$

The Shrödinger equation can be written using matrix elements for the four main conditions in this problem where $j < 0$ (Eq. A.2) , $j > N+1$ (Eq. A.6), inside the scattering region where $1 \leq j \geq N$ (Eq. A.4) and the boundary condition where $j = 0$, $j = N + 1$ (Eq. A.5, A.3) as below:

$$\varepsilon_0\psi_j - \gamma\psi_{j-1} - \gamma\psi_{j+1} = E_j\psi_j \qquad for \quad j < 0 \tag{A.2}$$

$$\varepsilon_0\psi_0 - \gamma\psi_{-1} - \gamma_L f_1 = E_j\psi_0 \qquad for \quad j = 0 \tag{A.3}$$

$$\sum_{j=1}^{N} h_{ij}f_j = Ef_i \Rightarrow \begin{cases} \sum h_{ij}f_j - \gamma_L\psi_0\delta_{11} - \gamma_R\phi_{N+1}\delta_{1N} = Ef_i \\ \sum h_{1j}f_j - \gamma_L\psi_0 = Ef_1 \\ \sum h_{Nj}f_j - \gamma_R\phi_{N+1} = Ef_N \end{cases} \qquad for \quad j = 1, N \tag{A.4}$$

$$\varepsilon_0\phi_{N+1} - \gamma_R f_N - \gamma\phi_{N+2} = E\phi_{N+1} \qquad for \quad j = N+1 \tag{A.5}$$

$$\varepsilon_0\phi_j - \gamma\phi_{j-1} - \gamma\phi_{j+1} = E\phi_j \qquad for \quad j > N+1 \tag{A.6}$$

From equation A.2 and A.3 we get

$$\gamma_L f_1 = \gamma \psi_1. \tag{A.7}$$

From equation A.5 and A.6 we get

$$\gamma_R f_N = \gamma \phi_N. \tag{A.8}$$

The following two vectors ($|f\rangle$ and $|x\rangle$) represent the wavefunction of the non-interacting scattering region and the constant perturbation from the two leads in the Shrödinger equation (Eq. A.9).

$$\text{scattering region: } |f\rangle = \begin{pmatrix} f_1 \\ f_2 \\ f_3 \\ \vdots \\ f_{N-1} \\ f_N \end{pmatrix} \qquad \text{perturbation: } |x\rangle = \begin{pmatrix} -\gamma_L \psi_0 \\ 0 \\ 0 \\ \vdots \\ 0 \\ -\gamma_R \phi_{N+1} \end{pmatrix}$$

$$h\,|f\rangle = E\,|f\rangle + |x\rangle\,, \tag{A.9}$$

which rearranges to the following

$$|f\rangle = (E - h)^{-1}\,|x\rangle\,. \tag{A.10}$$

We define the Green's function of the scattering region to be

$$g = (E - h)^{-1}. \tag{A.11}$$

Hence we conclude that the Green's function relates the wavefunction inside the scattering region to the perturbation from the leads by the means of following

equation

$$|f\rangle = g\,|x\rangle\,. \tag{A.12}$$

$$\begin{pmatrix} f_1 \\ f_2 \\ f_3 \\ \vdots \\ f_{N-1} \\ f_N \end{pmatrix} = \begin{pmatrix} g_{11} & g_{12} & g_{13} & \cdots & g_{1N} \\ g_{21} & g_{22} & g_{23} & \cdots & g_{2N} \\ \vdots & & & & \vdots \\ \vdots & & & & \vdots \\ g_{N1} & g_{N2} & g_{N3} & \cdots & g_{NN} \end{pmatrix} \begin{pmatrix} -\gamma_L\psi_0 \\ 0 \\ 0 \\ \vdots \\ 0 \\ -\gamma_R\phi_{N+1} \end{pmatrix} \tag{A.13}$$

Writing the equation above using matrix elements and considering equations A.8 and A.7, we have can conclude that

$$f_1 = \gamma_L\psi_0 g_{11} - \gamma_R\phi_{N+1}g_{1N} = \frac{\gamma}{\gamma_L}\psi_1 \tag{A.14}$$

and

$$f_N = \gamma_L\psi_0 g_{N1} - \gamma_R\phi_{N+1}g_{NN} = \frac{\gamma}{\gamma_R}\phi_N. \tag{A.15}$$

Using the boundary conditions we know that

$$\begin{aligned} &\psi_0 = 1 + 1 \\ &\psi_1 = e^{ik} + re^{-ik} = e^{ik} - e^{-ik} + e^{-ik} + re^{-ik} = 2i\sin k + \psi_0 e^{-ik} \\ &\phi_{N+1} = te^{ik(N+1)} \\ &\phi_N = te^{ikN} = \phi_{N+1}e^{-ik} \end{aligned} \tag{A.16}$$

Therefore we can write the boundary conditions as follows.

$$\psi_0 = \frac{\gamma_L}{\gamma}e^{ik}f_1 - 2i\sin k e^{ik} \tag{A.17}$$

$$\phi_{N+1} = \frac{\gamma_R}{\gamma}e^{ik}f_N \tag{A.18}$$

Defining the self-energies, Σ_L and Σ_R as following

$$\Sigma_{L/R} = \frac{-\gamma_{L/R}^2}{\gamma} e^{ik} = \sigma_{L/R} - i\Gamma_{L/R}, \tag{A.19}$$

where the real part is $\sigma_{L/R} = \frac{\gamma_{L/R}^2}{\gamma} \cos k$ and the imaginary part is $\Gamma_{L/R} = \frac{\gamma_{L/R}^2}{\gamma} \sin k$. Using the definition of the self-energies we can summarise equation A.17 and A.18 in to a matrix form.

$$\begin{pmatrix} -\gamma_L \psi_0 \\ -\gamma_R \phi_{N+1} \end{pmatrix} = \begin{pmatrix} -\Sigma_L f_1 \\ -\Sigma_R f_N \end{pmatrix} + \begin{pmatrix} 2\gamma_L i e^{ik} \sin k \\ 0 \end{pmatrix} \tag{A.20}$$

$$\begin{pmatrix} -\gamma_L \psi_0 \\ -\gamma_R \phi_{N+1} \end{pmatrix} = \underbrace{\begin{pmatrix} \Sigma_L & 0 \\ 0 & \Sigma_R \end{pmatrix}}_{\widehat{\Sigma}} \begin{pmatrix} f_1 \\ f_N \end{pmatrix} + \begin{pmatrix} 2i\gamma_L e^{ik} \sin k \\ 0 \end{pmatrix} \tag{A.21}$$

In the Dirac notations reads

$$|\widehat{x}\rangle = \widehat{\Sigma} \left|\widehat{f}\right\rangle + |s\rangle \,. \tag{A.22}$$

Where $|s\rangle = \binom{s_L}{0}$, is the vector determining the position of the source (left or right lead). From equation A.12 we know that $\left|\widehat{f}\right\rangle = \widehat{g}\,|\widehat{x}\rangle$. Therefore,

$$|\widehat{x}\rangle = (I - \widehat{\Sigma}\widehat{g})^{-1}\,|s\rangle \,. \tag{A.23}$$

To solve the equation A.23 we start from the most inner block, $\widehat{\Sigma}\widehat{g}$.

$$\widehat{\Sigma}\widehat{g} = \begin{pmatrix} \Sigma_L & 0 \\ 0 & \Sigma_R \end{pmatrix} \begin{pmatrix} g_{11} & g_{1N} \\ g_{N1} & g_{NN} \end{pmatrix} = \begin{pmatrix} \Sigma_L g_{11} & \Sigma_L g_{1N} \\ \Sigma_R g_{N1} & \Sigma_R g_{NN} \end{pmatrix} \tag{A.24}$$

Therefore $I - \widehat{\Sigma}\widehat{g}$ is given by

$$\begin{pmatrix} 1 & 0 \\ 0 & 1 \end{pmatrix} - \Sigma\widehat{g}\,|s\rangle = \begin{pmatrix} 1-\Sigma_L g_{11} & -\Sigma_L g_{1N} \\ -\Sigma_R g_{N1} & 1-\Sigma_R g_{NN} \end{pmatrix}. \tag{A.25}$$

Hence we can construct $|\widehat{x}\rangle$.

$$\begin{aligned} |\widehat{x}\rangle &= \begin{pmatrix} 1-\Sigma_L g_{11} & -\Sigma_L g_{1N} \\ -\Sigma_R g_{N1} & 1-\Sigma_R g_{NN} \end{pmatrix}^{-1} \begin{pmatrix} S_L \\ 0 \end{pmatrix} \\ &= \frac{1}{det} \begin{pmatrix} 1-\Sigma_R g_{NN} & \Sigma_L g_{1N} \\ \Sigma_R g_{N1} & 1-\Sigma_L g_{11} \end{pmatrix} \begin{pmatrix} S_L \\ 0 \end{pmatrix} \end{aligned} \tag{A.26}$$

To demonstrate the relation between the wavefunctions and the Green's function we substitute the $|x\rangle$ vector in equation above

$$\begin{pmatrix} -\gamma_L \psi_0 \\ -\gamma_R \phi_{N+1} \end{pmatrix} = \frac{S_L}{det} \begin{pmatrix} 1-\Sigma_R g_{NN} \\ \Sigma_R g_{N1} \end{pmatrix}. \tag{A.27}$$

The transmission amplitude ($\phi_{N+1} = te^{ikN+1}$) is then given by

$$-\gamma_R t e^{ik(N+1)} = \frac{\Sigma_R g_{N1} S_L}{det}. \tag{A.28}$$

$$t = 2i \sin k \frac{\gamma_R \gamma_L}{\gamma} e^{ik} e^{-ikN} \frac{g_{N1}}{det}. \tag{A.29}$$

Therefore the transmission coefficient (T) is

$$T = |t|^2 = 4 \left(\frac{\gamma_R^2 \sin k}{\gamma} \right) \left(\frac{\gamma_L^2 \sin k}{\gamma} \right) \left| \frac{g_{N1}}{det} \right|^2. \tag{A.30}$$

Consequently we can write T in terms of Γ_L and Γ_R

$$T = 4\Gamma_L \Gamma_R \left| \frac{g_{N1}}{det} \right|^2, \tag{A.31}$$

where the determinant (det) is given by

$$\begin{aligned} det &= (1 - \Sigma_R g_{NN}) \cdot (1 - \Sigma_L g_{11}) - \Sigma_L \Sigma_R g_{1N} g_{N1} \\ &= 1 - \Sigma_R g_{NN} - \Sigma_L g_{11} + \Sigma_L \Sigma_R (g_{NN} g_{11} - g_{1N} g_{N1}). \end{aligned} \tag{A.32}$$

To finally be able to get a numerical answer we need to extract the g_{11}, g_{1N}, g_{N1} and g_{NN}. To do so, we use the completeness condition for the wavefunction to write the following

$$g = \sum_{n=1}^{N} \frac{|v_n >< v_n|}{E - \lambda_n}. \tag{A.33}$$

Using the equation above the ij^{th} element of the Green's function (g_{ij}) can be extracted as bellow

$$< i|g|j >= \frac{v(i)v(j)}{E - \lambda_n}. \tag{A.34}$$

From equation A.34, we understand that $g_{1N} = g_{N1}$. This results in simplification of equation A.32 to,

$$det = 1 - \Sigma_R g_{NN} - \Sigma_L g_{11}. \tag{A.35}$$

We can substitute the det and the Green's function elements found above, in the transmission coefficient.

$$\begin{aligned} T &= 4\Gamma_R \Gamma_L \left[\frac{(v(i)v(j))^2}{(E - \lambda)^2} \right] \times \frac{1}{\left| 1 - \Sigma_R \frac{v(N)^2}{E - \lambda} - \Sigma_L \frac{v(1)^2}{E - \lambda} \right|^2} \\ &= \frac{4\Gamma_R v(1)^2 \Gamma_L v(N)^2}{\left| (E - \lambda) - \Sigma_R v(N)^2 - \Sigma_L v(1)^2 \right|^2} \\ &= \frac{4\widehat{\Gamma}_R \widehat{\Gamma}_L}{\left| E - \lambda - \widehat{\sigma}_R - \widehat{\sigma}_L + i \left(\widehat{\Gamma}_R + \widehat{\Gamma}_L \right) \right|^2}. \end{aligned} \tag{A.36}$$

We define,

$$\widehat{\lambda} = \lambda - \widehat{\sigma}_R - \widehat{\sigma}_L. \tag{A.37}$$

Hence we can write the transmission coefficient in the form of the well known

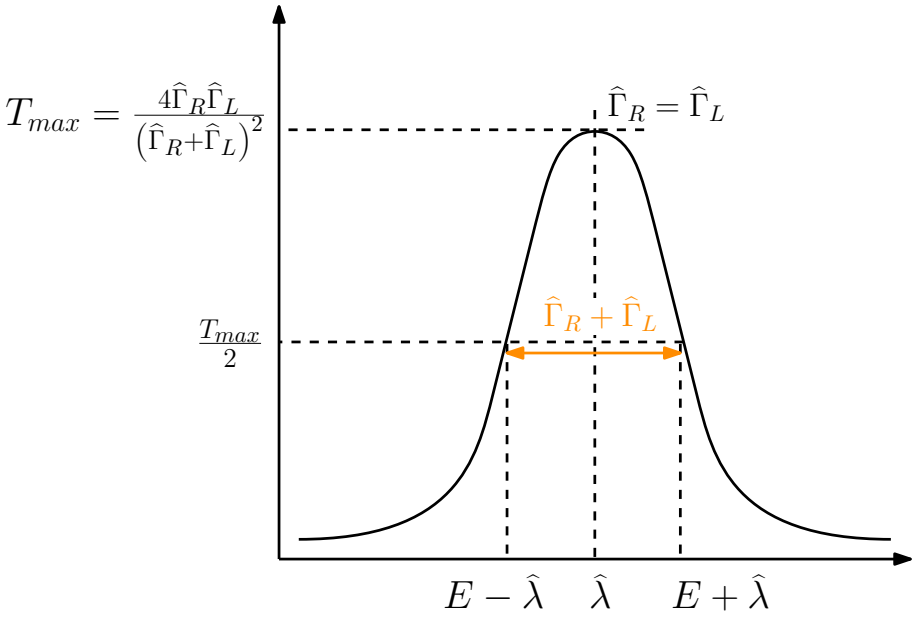

Figure A.2: A Breit-Wigner resonance: the demonstration of level broadening due to the imaginary part of the self-energy (Γ) and the shift in the resonances due to the real part of the self energy(σ).

Breit-Wigner formula

$$T = \frac{4\widehat{\Gamma}_R\widehat{\Gamma}_L}{(E-\widehat{\lambda})^2 + \left(\widehat{\Gamma}_R + \widehat{\Gamma}_L\right)^2}. \tag{A.38}$$

We can see from this equation that the real part of the self-energies ($\widehat{\sigma}_R+\widehat{\sigma}_L$) add to the eigenvalues of the isolated object and shift the resonances in the transmission coefficient as expected. The maximum of the transmission coefficient occurs when $\widehat{\Gamma}_R = \widehat{\Gamma}_L$. Moreover, $\widehat{\Gamma}_R + \widehat{\Gamma}_L$ defines the width of the resonances. This is also known as level broadening associated with the imaginary part of the self-energies. (Fig. A.2)

Appendix B

Green's Function of a perfect one dimensional lattice

Consider a perfect one dimensional chain where the on-site energies are given by ε_0 and the hopping integral elements are given by γ as shown in figure B.1. Using the definition of Green's function, we can write

$$[(E - H)\, g]_{jl} = \delta_{jl} = \begin{pmatrix} 1 & & \\ & \ddots & \\ & & 1 \end{pmatrix}_{jl}. \tag{B.1}$$

Where H is the Hamiltonian of the doubly infinite chain. We can write the equation above in the following form

$$\sum_i E_{ji} g_{il} - \sum_i H_{ji} g_{il} = \delta_{jl}. \tag{B.2}$$

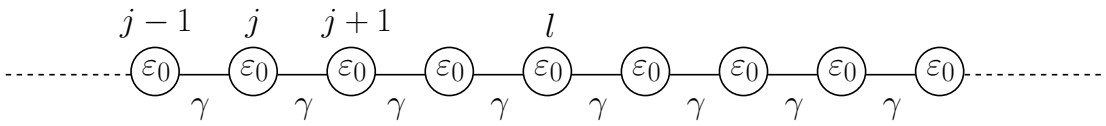

Figure B.1: A perfect doubly infinite 1D chain with on-site energies of ε_0 and hopping elements of γ.

Since all the off diagonal elements in E matrix are zero, the only non-zero term in the left side of the equation is for $n = i = j$. Therefore we can rewrite the equation above as

$$E_{nn}g_{nl} - \delta_{jl} = \sum_i H_{ji}g_{il}. \tag{B.3}$$

For the chain described in figure B.1, equation above reads

$$\varepsilon_0 g_{jl} - \gamma g_{j+1,l} - \gamma g_{j-1,l} = E g_{jl} - \delta_{jl}. \tag{B.4}$$

In order to solve the equation above we make a guess for the Green's function

$$g_{jl} = \underbrace{Ae^{ikj}}_{j\geq l} + \underbrace{Be^{-ikj}}_{j\leq 1}. \tag{B.5}$$

Therefore when $j = l$ the Green's function from left has to equal the Green's

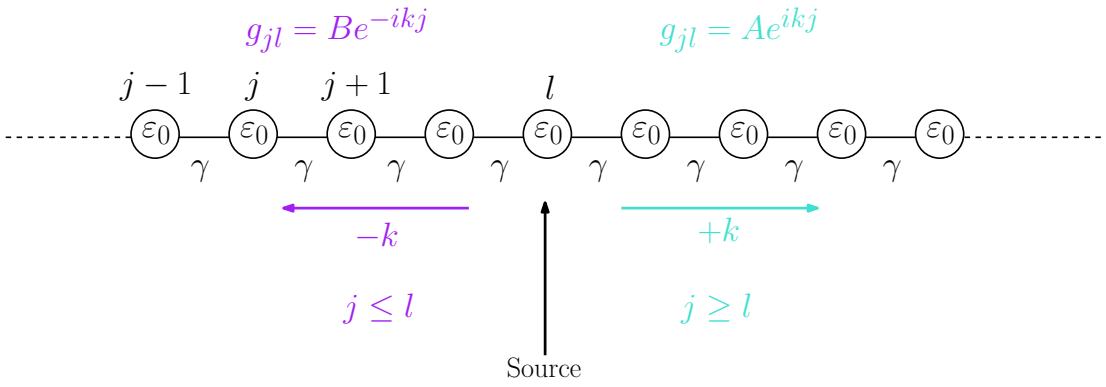

Figure B.2: The Retarded Green's function of an infinite one dimensional lattice. The excitation at $j = l$ causes the wave to propagate to the left and right with amplitudes A and B

function from right

$$g_{l,l} = Be^{-ikl} = Ae^{ikl} = C \Rightarrow A = Ce^{-ikl}, B = Ce^{ikl}. \tag{B.6}$$

Solving equation B.4 for when $j = l$, we get

$$\underbrace{(\varepsilon_0 - E)}_{2\gamma\cos(k)} g_{l,l} - \gamma \underbrace{g_{l+1,l}}_{j\geq l} - \gamma \underbrace{g_{l-1,l}}_{j\leq l} = -1. \tag{B.7}$$

for the off diagonal Green's functions $g_{l+1,l}$ and $g_{l-1,l}$ we have:

$$\begin{cases} g_{j,l} = Ce^{-ik(j-l)} \xrightarrow{j=l-1} g_{l-1,l} = Ce^{ik} \\ g_{j,l} = Ce^{-ik(j-l)} \xrightarrow{j=l+1} g_{l+1,l} = Ce^{ik} \end{cases} \tag{B.8}$$

Substituting in equation B.7 we get,

$$2C\gamma\cos(k) - C\gamma e^{ik} - C\gamma e^{ik} = -1 \tag{B.9}$$

Given that $\cos(k) = \frac{1}{2}(e^{ik} + e^{-ik})$ we can rewrite the equation above as,

$$C\gamma(-2i\sin(k)) = -1 \tag{B.10}$$

Therefore C reads

$$C = \frac{1}{2i\gamma\sin k} \xrightarrow{v=\frac{2\gamma\sin k}{\hbar}} C = \frac{1}{i\hbar v}, \tag{B.11}$$

where v is the group velocity. Now we can combine the two Green's functions for the $j \leq l$ and $j \geq l$.

$$\left.\begin{array}{l} j \leq l \Rightarrow g_{j,l} = \frac{e^{-ik_L(j-l)}}{i\hbar v} \\ j \geq l \Rightarrow g_{j,l} = \frac{e^{ik_L(j-l)}}{i\hbar v} \end{array}\right\} \Rightarrow g^R_{jl} = \frac{e^{ik_L|j-l|}}{i\hbar v} \tag{B.12}$$

g^R is called the retarded Green's function where the boundary conditions corresponds to outgoing waves propagating from the point of excitation (source). Advanced Green's function (g^A) is another possible answer for equation B.4 which satisfies the boundary condition where the incoming waves disappear at the point of excitation (sink). (Fig. B.3)

$$g^A_{jl} = \frac{e^{-ik|j-l|}}{-i\hbar v} \tag{B.13}$$

Having found the Green's function of a doubly infinite chain, we would like to apply this knowledge to a scattering problem. More precisely we would like to find

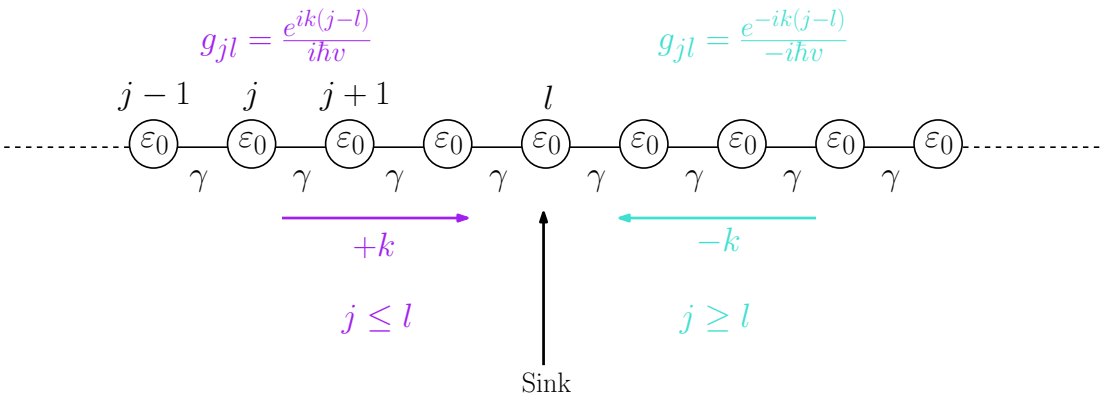

Figure B.3: Advanced Green's function corresponds to the boundary condition where two incoming waves disappear at the point of excitation

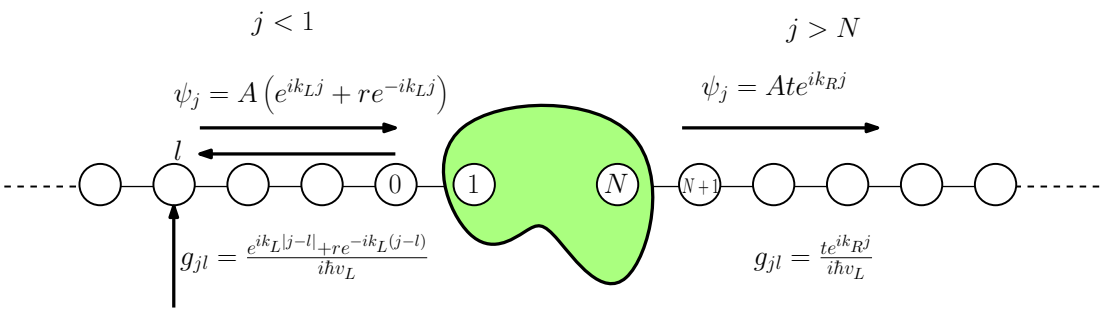

Figure B.4: A scattering problem where the scatterer has N sites and is connected to two leads.

a relation between the scattering amplitude and the Green's function. Consider a system with a scatterer consist of N sites where two leads are connected to site 1 and N. The wavefunction of each side of the scattering region is shown in figure B.4 where A is the overall amplitude of choice and $k_{L/R}$ are the wave numbers of left and right lead. Considering that the source is located on site l on the left hand side, the Green's function is also demonstrated in figure B.4. Note that there is an additional term in the Green's function of the left lead which stands for the reflection from the scattering region. Solving for the boundary conditions where $j = 0$ and $j = N+1$ yields Fisher-Lee equations for the transmission and reflection amplitudes

$$t = i\hbar\sqrt{v_R v_L} g_{N+1,0} e^{-ik_R(N+1)} \tag{B.14}$$

and

$$r = \left(\frac{g_{00}}{A_0} - 1\right) = i\hbar v_L g_{00} - 1, \tag{B.15}$$

where g_{00} and $g_{N+1,0}$ are the surface Green's functions of the left and right lead respectively.

Appendix C

Dyson's equation

As shown in appendix B, the Fisher-Lee equations are given as follows.

$$\begin{aligned} t &= G_{10} i\hbar v \\ r &= G_{00} i\hbar v - 1 \end{aligned} \tag{C.1}$$

To obtain the transmission and reflection amplitudes it is desirable to find G_{10} and G_{00}. Consider the problem where we have a doubly infinite chain and we add a scatterer to it. (Fig. C.1) The full Hamiltonian of such system can be written as

$$H = H_O + H_S. \tag{C.2}$$

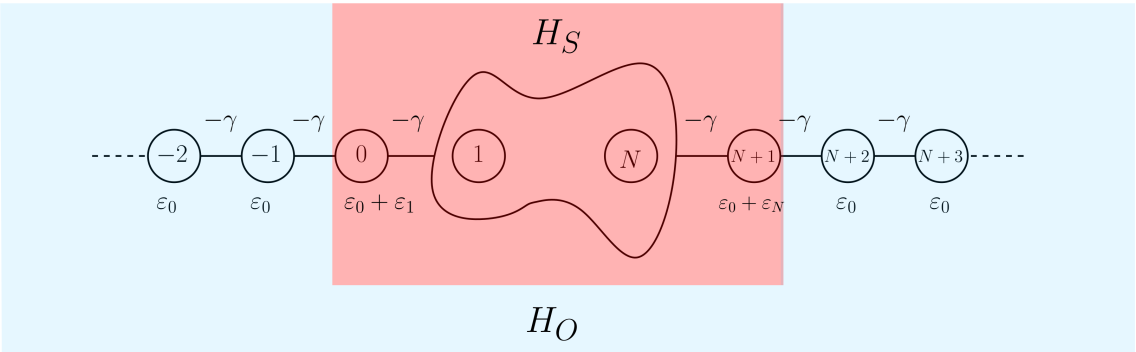

Figure C.1: The scatterer can be defined as a perturbation (H_S) to the doubly infinite chain (H_O).

Where H_O is the Hamiltonian of the doubly infinite chain and H_S is the Hamiltonian of the scatterer (O stands for outside and S stands for scatterer). (Eq. C.3) Although H_S has the same infinite dimensions as H_O, in practice, however, only a small block of it is non-zero ($\bar{h}$ in Eq. C.3).

$$H = \begin{pmatrix} \ddots & \ddots & & & & \\ \ddots & \varepsilon_0 & -\gamma & & & \\ & -\gamma & \varepsilon_0 & -\gamma & & \\ & & -\gamma & \varepsilon_0 & -\gamma & \\ & & & -\gamma & \varepsilon_0 & \ddots \\ & & & & \ddots & \ddots \end{pmatrix} + \begin{matrix} \\ \\ \\ 0 \\ \\ N+1 \\ \\ \end{matrix} \begin{pmatrix} & & 0 & & N+1 & \\ & & & & & \\ & & & & & \\ & \varepsilon_1 & & \bar{h} & & \\ & & & & & \\ & & & & \varepsilon_{N+1} & \\ & & & & & \end{pmatrix} \tag{C.3}$$

We introduce the Green's function of the whole system G according to the definition as

$$(E - H)G = 1. \tag{C.4}$$

We define $\bar{G}$ to be the block of Green's function associated with the scatterer.

$$G = \begin{pmatrix} & & & \\ & G_{00} & & \\ & & \bar{G} & \\ & & & G_{N+1} \\ & & & \end{pmatrix} \tag{C.5}$$

Substituting from equation C.2 for H, in equation C.4 and rearranging we get

$$(E - H_O)G = H_S G + 1. \tag{C.6}$$

Considering $(E - H_O)g = 1$, where g the Green's function of the doubly infinite chain, we can multiply the equation above with g

$$G = gH_S G + g. \tag{C.7}$$

Equation above in matrix elements notation reads

$$\begin{aligned} G_{ij} &= g_{ij} + (gH_S G)_{ij} \\ &= g_{ij} + \sum_{-\infty}^{+\infty} g_{il} H_S^{lk} G_{kj}. \end{aligned} \tag{C.8}$$

Although the sum in equation C.8 is from $-\infty$ to $+\infty$ the only non zero terms are from 0 to $N + 1$ as demonstrated in equation C.3.

$$G_{ij} = g_{ij} + \sum_{0}^{N+1} g_{il} H_S^{lk} G_{kj} \tag{C.9}$$

Therefore, we can reduce the problem to a finite problem where we replace g by $\bar{g}$, G by $\bar{G}$ and H_S by $\bar{h}$.

$$\bar{G} = \bar{g} + \bar{g}\bar{h}\bar{G} \tag{C.10}$$

Since these matrices are finite, the inversion of them is possible,

$$\bar{G} = \bar{g}(1 - \bar{g}\bar{h})^{-1}. \tag{C.11}$$

Therefore we can write

$$\bar{G} = (\bar{g}^{-1}(1 - \bar{g}\bar{h}))^{-1}. \tag{C.12}$$

Hence we find the so called 'Dyson's equation' to be,

$$\bar{G} = (\bar{g}^{-1} - \bar{h})^{-1}. \tag{C.13}$$

Note that finding $\bar{G}$ involves two matrix inversions which is always the case when working with Green's functions. The definitions used in this section are general

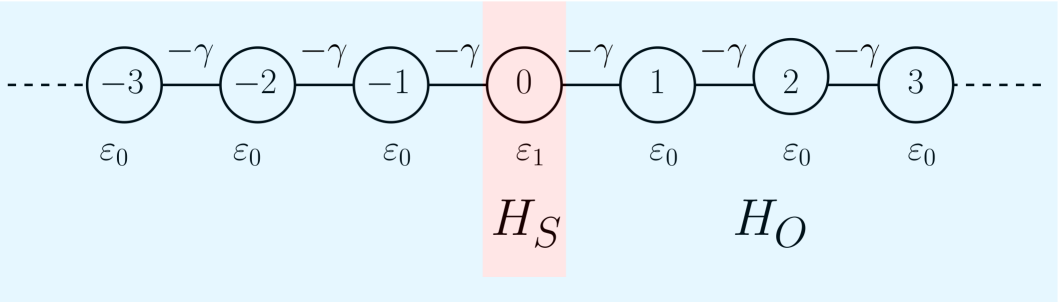

Figure C.2: Infinite chain with a single impurity.

an do not depend on the type of interactions being used therefore the properties of the Green's function can be used with any system. In the following two section, we discuss two examples where the perturbation is a single and a 2×2 impurity.

C.1 Example-Single impurity

Consider the example where the perturbation to the doubly infinite chain is just a single site impurity.(Fig. C.2) Let's remind ourselves of the the Green's function of a doubly infinite chain,

$$\bar{g}_{jl} = \frac{e^{ik|j-l|}}{i\hbar v}. \tag{C.14}$$

Therefore for $\bar{g}$ we have,

$$\bar{g} = \bar{g}_{00} = \frac{1}{i\hbar v}. \tag{C.15}$$

Since in this case, $\bar{h} = \varepsilon_1$ for $\bar{G}$ we have,

$$\bar{G} = \bar{G}_{00} = (i\hbar v - \varepsilon_1)^{-1}. \tag{C.16}$$

Therefore we can re-write the Fisher-Lee equation as,

$$t = i\hbar v G_{00} = \frac{i\hbar v}{i\hbar v - \varepsilon_1}. \tag{C.17}$$

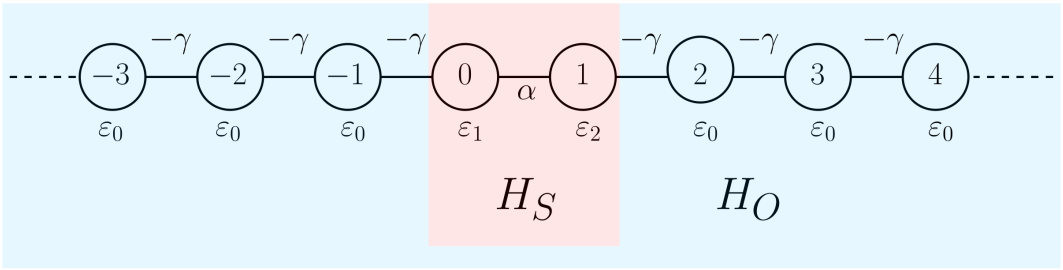

Figure C.3: Infinite chain with a 2 × 2 impurity.

Therefore the transmission coefficient is given by,

$$T = |t|^2 = \frac{1}{1 + (\frac{\varepsilon_1}{2\gamma \sin(k)})^2}. \tag{C.18}$$

C.2 Example - 2×2 impurity

In the second example we would like to consider the example where the perturbation is a two site impurity.(Fig. C.3) Therefore the non-zero part of the perturbation matrix to the doubly finite chain, $\bar{h}$, is a 2×2 matrix,

$$\bar{h} = \begin{pmatrix} \varepsilon_1 - \varepsilon_0 & -\alpha + \gamma \\ -\alpha + \gamma & \varepsilon_2 - \varepsilon_0 \end{pmatrix}. \tag{C.19}$$

remember h_1 matrix should be the non zero part of the H_1 matrix. H_1 matrix should satisfy the equation $H = H_0 + H_1$, where H is the total Hamiltonian of our problem and H_0 is the Hamiltonian of a one dimensional chain. Moreover , $\bar{g}$ reads,

$$\bar{g} = \begin{pmatrix} g_{00} & g_{01} \\ g_{10} & g_{11} \end{pmatrix}. \tag{C.20}$$

Where the Green's function of the doubly infinite chain is ,

$$g_{jl} = \frac{e^{ik|j-l|}}{i\hbar v} \tag{C.21}$$

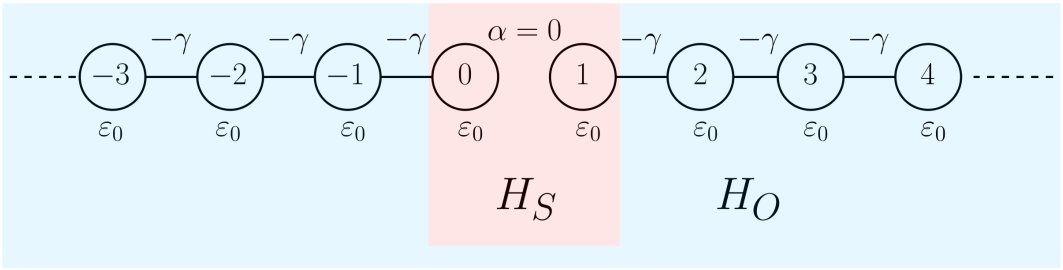

Figure C.4: The special case where $\varepsilon_1 = \varepsilon_2 = \varepsilon_0$ and $\alpha = 0$, which yields to two semi-infinite leads.

Therefore,

$$\bar{g}^{-1} = \frac{i\hbar v}{det} \begin{pmatrix} 1 & e^{-ik} \\ e^{-ik} & 1 \end{pmatrix} \tag{C.22}$$

Where $det = 1 - e^{-2ik}$. To obtain the transmission and reflection amplitudes we yet need to find $\bar{G}$,

$$\bar{G} = (\bar{g}^{-1} - \bar{h})^{-1} \tag{C.23}$$

Substituting $\bar{g}$ from equation C.22 we have

$$\bar{G} = \left(\frac{i\hbar v}{det} \begin{pmatrix} 1 & e^{-ik} \\ e^{-ik} & 1 \end{pmatrix} - \begin{pmatrix} \varepsilon_1 - \varepsilon_0 & -\alpha + \gamma \\ -\alpha + \gamma & \varepsilon_2 - \varepsilon_0 \end{pmatrix} \right)^{-1} \tag{C.24}$$

$$\bar{G} = \frac{det}{i\hbar v} . \frac{1}{DET} \cdot \begin{pmatrix} 1 - \frac{\bar{h}_{11}.det}{i\hbar v} & e^{ik} + \frac{\bar{h}_{12}.det}{i\hbar v} \\ e^{ik} + \frac{\bar{h}_{12}.det}{i\hbar v} & 1 - \frac{\bar{h}_{11}.det}{i\hbar v} \end{pmatrix}, \tag{C.25}$$

where the two determinants are as followed:

$$det = 1 - e^{-2ik} \tag{C.26}$$

$$DET = (1 - \frac{\bar{h}_{11}.det}{i\hbar v})^2 - (e^{ik} + \frac{\bar{h}_{12}.det}{i\hbar v})^2 \tag{C.27}$$

Having found $\bar{G}$, we can now consider the special case where $\varepsilon_1 = \varepsilon_2 = \varepsilon_0$ and $\alpha = 0$.(Fig. C.4) This arrangement results in two semi-infinite lead which equivalent to having a doubly infinite chain and introducing a perturbation by cutting the

chain in the middle.

$$\bar{h} = \begin{pmatrix} 0 & \gamma \\ \gamma & 0 \end{pmatrix} \tag{C.28}$$

Therefore we can write the determinant in equation C.27 as

$$\begin{aligned} DET &= 1 - (e^{ik} + \frac{\gamma.det}{i\hbar v})^2 \\ &= 1 - (e^{ik} + \frac{det}{2i\sin(k)})^2. \end{aligned} \tag{C.29}$$

Now if we evaluate $\bar{G}_{00}$ or $\bar{G}_{11}$, we will find the surface Green's function at the end of a semi-infinite chain.

$$\bar{G}_{00} = \bar{G}_{11} = \frac{det}{i\hbar v} \cdot \frac{1}{DET} = \frac{1 - e^{2ik}}{i2\gamma \sin k} = \frac{-e^{ik}}{\gamma} \tag{C.30}$$

$\bar{G}_{00}$ and $\bar{G}_{11}$ are also known as the surface Green's function.

Appendix D

ZT

The thermoelectric effect also known as Seebeck effect refers to voltage generation in a conductor or a semiconductor subjected to temperature gradient. The efficiency of a thermoelectric device in converting heat to electricity is given by the dimensionless variable, figure of merit (ZT).

$$ZT = \frac{GS^2sT}{\kappa_{ph} + \kappa_e} \tag{D.1}$$

ZT of a material can be tuned depending on the following variables:

- Seebeck coefficient , $S = \frac{-\Delta V}{\Delta T}$: Voltage generated per degree of temperature difference over a material.
- Thermal conductivity , $\kappa = \frac{Q}{\Delta T}$: Heat carried per degree of temperature difference over a material by electrons and phonons ($\kappa = \kappa_e + \kappa_{ph}$).
- Electrical conductivity , $G = \frac{I}{\Delta V}$.
- Peltier coefficients, $\Pi = \frac{Q}{I}$.

In the equation for ZT, the term GS^2 is called power factor. The importance of power factor is that higher power factor is associated with more energy generation

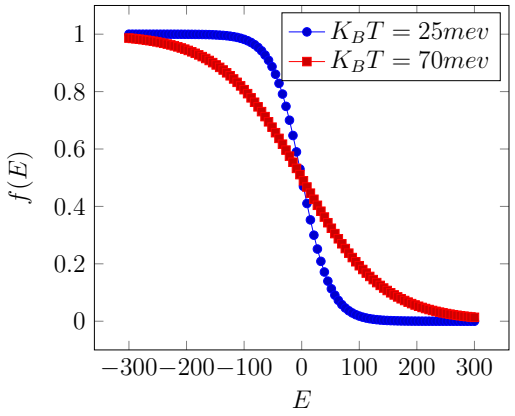

Figure D.1: Fermi distribution of charges in a hot (red) and cold (blue) lead.

in a material (not necessarily more efficient). Combining the equations for S, κ and G, we can construct a 2 by 2 matrix to relate ΔV and Q to I and ΔT. (Eq. D.2)

$$\begin{pmatrix} \Delta V \\ Q \end{pmatrix} = \begin{pmatrix} 1/G & S \\ \Pi & \kappa \end{pmatrix} \begin{pmatrix} I \\ \Delta T \end{pmatrix} \tag{D.2}$$

Herein we present a numerical method to calculate the coefficients presented in the 2 by 2 matrix in equation D.2 for a nano-structure between two hot and cold reservoirs.

Figure D.1 demonstrates the Fermi distribution of charges in a hot (red) and cold (blue) lead. The distribution of charge carriers in the lead with raised temperature is greater at higher energies. This means that in the hot lead, the high energy electrons are transmitted with a higher probability.

The two reservoirs send electrons into the scattering region and the probability of the occupancy of a particular channel is given by the Fermi function. If we pick on a particular channel in the left lead, the number of electrons carried by this channel to the right lead is given by,

$$\delta n = \frac{2}{\hbar} T(E)[f_1(E) - f_2(E)] \tag{D.3}$$

The number 2 in the nominator is for the channel being able to carry both spin

up and spin down electrons. Therefore current is given by,

$$I = \frac{2e}{\hbar} \int dET(E) \left[f_1(E) - f_2(E) \right] \tag{D.4}$$

Heat flux is,

$$\dot{Q} = \frac{2}{h} \int dET(E)(E - E_f) \left[f_1(E) - f_2(E) \right] \tag{D.5}$$

Assuming the difference between f_1 and f_2 is small, we can do a Taylor expansion of $f_1(E)$ with respect to temperature,

$$f_1(E) = f_2(E) + \frac{\partial f_1}{\partial T}(T_1 - T_2) + \frac{\partial f_1}{\partial E_{f_1}}(E_{f_1} - E_{f_2}) \tag{D.6}$$

To differentiate the Fermi function for the first lead, we substitute the exponent by x,

$$f_1(E) = \frac{1}{e^{\frac{E - E_{f_1}}{K_B T}} + 1} = \frac{1}{e^x + 1} \tag{D.7}$$

Therefore f_1 differentiated with respect to T_1 and differentiated with respect to E_{f_1} is ,

$$\frac{\partial f_1}{\partial T_1} = \left(\frac{-\partial f_1}{\partial x} \right) \left(\frac{E - E_{f_1}}{K_B T_1^2} \right) \qquad , \qquad \frac{\partial f_1}{\partial E_f} = \left(\frac{-\partial f_1}{\partial x} \right) \left(\frac{1}{K_B T} \right) \tag{D.8}$$

Substituting this into equation D.4

$$\frac{I}{e} = \frac{2}{h} \int dET(E) \left(\frac{-\partial f_1}{\partial x} \right) \left[\frac{E - E_{f_1}}{K_B T_1^2} (T_1 - T_2) + \frac{E_{f_1} - E_{f_2}}{K_B T} \right] \tag{D.9}$$

Therefore $\dot{Q}$ reads,

$$\dot{Q} = \frac{2}{h} \int T(E) \frac{\partial f}{\partial x} (E - E_f) \left[e\Delta V + \frac{E - E_f}{T} \Delta T \right] dE \tag{D.10}$$

Therefore we can write a matrix which relates I and Q to ΔV and ΔT, where all

the matrix elements are functions of transmission coefficient,

$$\begin{pmatrix} I \\ Q \end{pmatrix} = \frac{2}{h} \begin{pmatrix} L_0 & -\frac{L_1}{T} \\ -L_1 & \frac{L_2}{T}\kappa \end{pmatrix} \begin{pmatrix} \Delta V \\ \Delta T \end{pmatrix} \tag{D.11}$$

Where for $x = E - E_f$, L_n is given by the integral bellow,

$$L_n = \int_{-4K_BT}^{4K_BT} T(E) \frac{-\partial f}{\partial x} (x^n)\, dx \tag{D.12}$$

Comparing this equation with equation D.2 we can write the Seebeck coefficient as,

$$S = -\frac{-\Delta V}{\Delta T} = \frac{-1}{eT} \frac{L_1}{L_0} \tag{D.13}$$

The electrical conductance (G) can be written using Landauer formula,

$$G = \frac{2e^2}{h} L_0 \tag{D.14}$$

The electronic thermal conductance (κ_e) is given by,

$$\kappa_e = \frac{2}{hT} \left(L_2 - \frac{L_1^2}{L_0} \right) \tag{D.15}$$

Combining the above three equation we can write ZT as,

$$ZT = \frac{\left(\frac{L_1^2}{L_0}\right)}{\frac{L_2}{L_0} - \left(\frac{-L_1^2}{L_0}\right)} \tag{D.16}$$

This method will allow us to numerically calculate the figure of merit from the transmission coefficient which is ideal for the purpose of this work.

Appendix E

Python code for solving the analytical model provided in chapter 3

```
#   Analytical toy-model for studying Graphene/SAM/Au devices
#
#   Authors of this code :  M. Famili, I. Grace, C. J. Lambert
#
#   Please site the refering article in all your publications arising
#   from your use of this code
#
import numpy as np
import matplotlib.pyplot as plt
import scipy as sp
from scipy import integrate
def fi_loc(array,value):
        idx = (np.abs(array-value)).argmin()
        return idx


ED0=-0.2
Gam0=0.1
Gam1=0.5
em=1
z=1

pref=7.74E-5
alph=1
gD=1
gG=0
bD=0
bG=0
dE=0.001
dV=0.05

VD=np.arange(-1,1.1,dV)
VG=np.arange(-1,1,2)
E=np.arange(-2,2,dE)
EDir=np.zeros((len(VD),len(VG)))
epsi=np.zeros((len(VD),len(VG)))
Gam2=np.zeros(len(E))
T=np.zeros((len(E),len(VD),len(VG)))
int_cur=np.zeros((len(VD),len(VG)))
dif_cur=np.zeros((len(VD),len(VG)))
Eplot=np.zeros((len(E),len(VG)))
for v_d in range(len(VD)):
        for v_g in range(len(VG)):
                EDir[v_d,v_g]=ED0-gD*VD[v_d]-gG*VG[v_g]
                epsi[v_d,v_g]=em-bD*VD[v_d]-bG*VG[v_g]

for v_g in range(len(VG)):
        print(v_g)
        for v_d in range(len(VD)):
                for e in range(len(E)):
                        Gam2[e]=Gam0+alph*abs(E[e]-EDir[v_d,v_g])**z
                        T[e,v_d,v_g]=4*Gam1*Gam2[e]/((E[e]-epsi[v_d,v_g])**2+(Gam1+Gam2[e]))**2
                Tint=T[min(fi_loc(E,-VD[v_d]),fi_loc(E,0)):max(fi_loc(E,-VD[v_d]),fi_loc(E,0)),v_d,v_g]
                int_cur[v_d,v_g]=(sp.integrate.trapz(T[min(fi_loc(E,-VD[v_d]),fi_loc(E,0)):max(fi_loc(E,-
VD[v_d]),fi_loc(E,0)),v_d,v_g],dx=dE)*VD[v_d]/abs(VD[v_d]))*pref
                dif_cur[:,v_g]=np.gradient(int_cur[:,v_g],dV)
                Eplot[:,v_g]=E
Tplot=T[:,::10,:]
VDplot=VD[::10]

plt.figure(1)
plt.subplot(212)
for v_g in range(len(VG)):
        for v_d in range(len(VDplot)):
                        plt.plot(Eplot,Tplot[:,v_d,:],label='$V_D=$'+str(round(-VDplot[v_d],2)),linewidth=1)
plt.ylabel('$T(E)$')
plt.xlabel('$E$')
plt.legend()


plt.subplot(221)
plt.ticklabel_format(style='sci', axis='y', scilimits=(0,0))
plt.ylabel('$I$')
plt.xlabel('$V_D(V)$')
for v_g in range(len(VG)):
    plt.plot(VD,int_cur[:,v_g],label='$V_G=$'+str(round(-VG[v_g],2)),linewidth=1)
plt.legend()


plt.subplot(222)
plt.ticklabel_format(style='sci', axis='y', scilimits=(0,0))
for v_g in range(len(VG)):
        plt.plot(VD,dif_cur[:,v_g], label='$V_G=$'+str(round(-VG[v_g],2)),linewidth=1)
plt.legend()
plt.ylabel('$dI/dV$')
plt.xlabel('$V_D(V)$')
plt.draw()
plt.show()
```